Journal of
Materials Chemistry C

REVIEW

View Article Online
View Journal | View Issue

Cite this: J. Mater. Chem. C, 2018, 6, 11903

The researcher's guide to solid-state dye-sensitized solar cells

Iacopo Benesperi, Hannes Michaels and Marina Freitag *

In order to sustainably support its ever-increasing energy demand, the human society will have to harvest renewable energy wherever and whenever possible. When converting light to electricity, silicon solar cells are the technology of choice to harvest direct sunlight due to their high performance and continuously dropping price. For diffused light and indoor applications, however, silicon is not the material of choice. To power the next gizmo in your smart home, dye-sensitized solar cells (DSCs) are a viable alternative. Made from inexpensive, earth-abundant, and non-toxic materials, DSCs perform best at low light intensity. So far, issues such as leakage of the liquid electrolyte and its corrosive nature have limited the commercialization of this technology. To overcome these limitations, solid-state DSCs (ssDSCs) – in which the liquid electrolyte is replaced by a solid material – have been developed. For many years their efficiencies have been poor, preventing them from being widely employed. In the past six years, however, research efforts have led them to rival with their liquid counterparts. Here, we will review recent advancements in the field of ssDSCs. Every device component will be acknowledged, from metal oxides and new dyes to novel hole transporters, dopants, counter-electrodes and device architectures. After reviewing materials, long-term stability of devices will be addressed, finally giving an insight into the future that awaits this exciting technology.

Received 17th July 2018,
Accepted 21st September 2018

DOI: 10.1039/c8tc03542c

rsc.li/materials-c

1. Introduction

Our modern society is not the first to face an energy crisis.[1] Already the ancient Greeks have faced a shortage of charcoal made from trees, after they stripped their land from the forests, resulting in wide-area erosion. Socrates described that the crisis was diverted by smart city planning, so that every household was able to take advantage of the sun.[2] Certainly, the technologies for harnessing sunlight have evolved and photovoltaics have become a major focus in today's politics and research.[3–7]

Solar cells can generate electrical power using the photovoltaic effect, which was first presented by the French physicist A. E. Becquerel in 1839[8] and much later implemented in a

Department of Chemistry – Ångström Laboratory, Uppsala University, 751 20 Uppsala, Sweden. E-mail: marina.freitag@kemi.uu.se

Iacopo Benesperi

Dr Iacopo Benesperi received his MSc in Materials Science from the Department of Chemistry, Turin University, Italy, under the supervision of Prof. Barolo. Thanks to his work on hole conducting materials for perovskite solar cells, he obtained his PhD in Chemistry from the School of Chemistry, Monash University, under the supervision of late Prof. Spiccia, Dr Simonov, Prof. Bach and Prof. Cheng. He is currently a research fellow at Uppsala University in Dr Marina Freitag's group, working on charge transport materials for thin-film solar cells.

Hannes Michaels

Hannes Michaels obtained his MSc degree in Nanoscience in 2017 from the University of Hamburg, Germany, after contributions to the research groups of Prof. Dr Hans-P. Oepen and Prof. Dr Wilfried Wurth in cooperation with Uppsala University, Sweden. Currently, he is a doctoral student at the Department of Chemistry in Uppsala exploring charge transport materials based on transition metal complexes for photovoltaic applications in the laboratory of Dr Marina Freitag and Prof. Dr Gerrit Boschloo.

successful device by Bell Labs.[9,10] The most known type of solar cells are semiconductor devices made from silicon. In these solar cells, charges are generated and separated in a p–n junction of the semiconductor. With silicon being the dominant material used in photovoltaic solar power technology, there are also a handful of competitive thin-film technologies, which are easier to realize, but rely on more expensive and toxic raw materials. Research has branched out to alternative materials for use in solar cells in laboratories around the world.

In 1966 Gerischer introduced a very different concept to the p–n junction, the approach of a photochemical cell (PEC), with a dye sensitizer bound to a metal oxide semiconductor (ZnO) and a liquid electrolyte between the anode and cathode.[11,12] Only in 1991 did O'Regan and Grätzel show that the implementation of a mesoporous network of metal oxides resulted in efficient PCEs, and the concept of dye sensitized solar cells was made known.[13] Unlike other solar cell technologies, here the dyes are responsible for light absorption, charge separation and injection of charge carriers into the semiconductor, which only plays the role of the electron transport layer. The redox electrolyte is responsible for regeneration of the oxidized dye and charge transport between the electrodes.[14–16] Until now, efficiencies of more than 14% have been realized under full sun illumination.[17–19] The DSCs promise to be made of cost efficient materials by sustainable production techniques.[20–22]

Currently the cost efficiency is becoming less relevant due to the tremendous drop in prices of silicon based systems.[17,23] Further issues regarding the use of corrosive, toxic, flammable and volatile liquid electrolytes are still being investigated and settled.[24–29] The more difficult task of sealing liquid junctions in DSCs in comparison to silicon panels, for which production has long been industrialized, is one of the major limitations for module fabrication.[30,31] Solid state dye-sensitized solar cells overcome this limitation with the replacement of the liquid electrolyte by solid charge transport materials.[24,32–35]

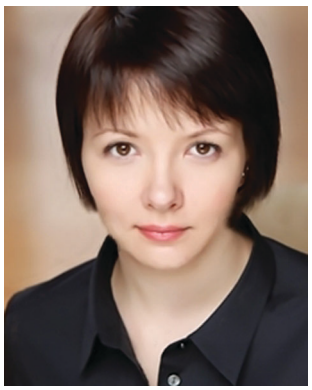

Marina Freitag

Dr Marina Freitag is presently an Assistant Professor at the Department of Chemistry, Uppsala University, continuing her work in coordination chemistry and solar cells. Previously, she held a postdoc position at EPFL (Prof. Anders Hagfeldt's). She received her PhD degree with Prof. Galoppini from Rutgers University, USA, and her BSc, in Chemistry from Freie Universität Berlin, Germany. She is the inventor of the so-called Zombie-cell and she contributed to recent breakthroughs in dye-sensitized solar cells for low-power applications.

It was only in 1988 that Tennakone reported for the first time a solid-state dye-sensitized heterojunction between TiO_2 and CuSCN.[36–39] However, dye-sensitized photocurrents were still low due to the nonporous structure of the junction. Since then, alternative approaches have been undertaken to form solid-state dye-sensitized junctions, employing either wide bandgap semiconductors or organic semiconductors. The general idea remained: in solid-state dye sensitized solar cells, the liquid redox electrolyte is replaced by a solid-state hole transporting material or a polymer electrolyte.[24,40–42]

Until recently, a reduction in the performance of ssDSCs in comparison to their liquid counterparts was observed and was the consequence of poor pore filling,[43–48] electron recombination at the semiconductor interface[49–53] and the lower conductivity[54,55] of the commonly used hole transport and polymer electrolyte materials.[24,33]

The objective of this review is to give a broad overview of the use of the various types of charge transporting materials and the recent progress made in the field of ssDSCs. The review also highlights the performance of several ssDSCs utilizing new organic and small molecule hole transport materials.

2. Operation principles and structure

2.1. Device structure

The traditional ssDSCs (Fig. 1a) consist of two main electrodes, the photoelectrode or working electrode and the counter electrode (CE). The working electrode (WE) consists of nanoporous metal oxide deposited onto a fluorine doped tin oxide (FTO) coated glass substrate. Usually a blocking layer is deposited on top of the FTO layer to avoid direct contact with the hole transporting material (HTM). The commonly used blocking layer is a compact layer of sintered TiO_2 and is usually optimized with respect to the HTL.[15,56] The most commonly used semiconductor metal oxide is mesoporous anatase TiO_2 with a particle size

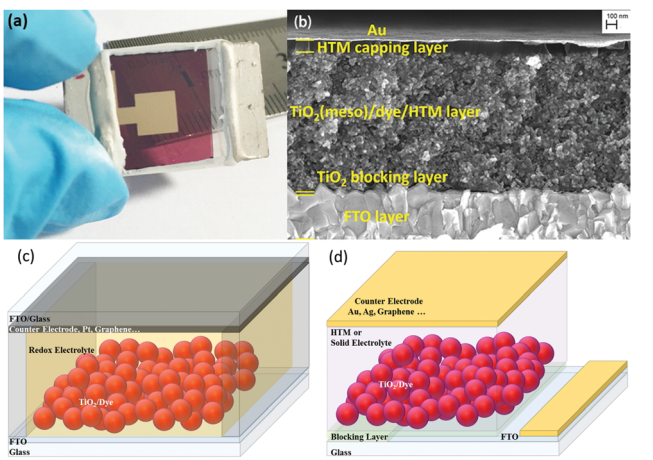

Fig. 1 (a) A fully assembled ssDSC with a Au counter electrode. (b) Cross-sectional electron microscopy image of a ssDSC. Adapted with permission from ref. 78. Copyright 2016 American Chemical Society. (c) Schematic sketch of solar cell architectures for the assembly of liquid-junction DSCs and (d) ssDSCs.

of around 20–30 nm. The high surface area of nanostructured TiO_2 is a prerequisite to absorb a large amount of sensitizer on the extended surface area, as seen in the exemplary cross-section SEM picture in Fig. 1b. One of the most crucial parts of any DSC is the light absorbing sensitizer. There are a large variety of light absorbers for DSCs, which can be categorized into metal-organic complexes and organic dyes.[16,57–66]

A schematic representation to distinguish between DSCs and ssDSCs is given in Fig. 1c and d. The large difference in device structure in comparison to the liquid junction is certainly the use of a solid redox electrolyte or HTM, but also redundancy of a spacer and further sealing between the electrodes. In the case of liquid-electrolyte DSCs (Fig. 1c), the charge transport between the working and counter electrodes is mediated by a redox electrolyte. In a solid-state DSC (Fig. 1d), a solid hole transporting material infiltrates the porous metal oxide (Fig. 1b). In ssDSCs, the mobility of the holes in the HTM is usually higher than the electron mobility in mesoporous TiO_2. Nevertheless, it is very important to balance the thickness of the overlying HTM layer. If it is too thick, an increased series resistance arises in the solar cell. If the layer is too thin, however, pinholes could appear resulting in contact of the metal contact with the mesoporous TiO_2 film and shunting of the device.[67–71]

The counter electrode usually consists of metal (Au, Ag) or carbon-based materials deposited by drop casting or evaporation on top of the charge transporting layer.[72–77]

2.2. Working principles

The conversion of light for power generation follows similar principles to those in photosynthesis. In Fig. 2, the basic working steps are shown.[79]

The dye sensitizer is bound *via* a functional group to a wide-band gap n-type semiconductor, most commonly TiO_2 or ZnO.[80,81] The sensitizer's electron in the ground state – *i.e.* in the highest occupied molecular orbital (HOMO) – reaches the excited state – *i.e.* the lowest unoccupied molecular orbital (LUMO) – upon light absorption. In the following step, the excited-state dye injects an electron into the conduction band of the metal oxide semiconductor. This is the moment of charge separation; the electrons are in the conduction band of the semiconductor and the holes are positioned in the oxidized dye. The semiconductor is responsible for fast electron transport to the FTO (fluorine doped tin oxide) electrode by diffusion.[71] The redox electrolyte or in the case of ssDSCs a solid hole transport material facilitates the regeneration of the oxidized dye and manages the charge transport to the counter electrode. Redox electrolytes are ionic conductors in which charges are transported *via* diffusion (concentration controlled) and/or by migration (electric field controlled).[26,82–84] In solid charge transport materials, the transport is electronic conduction from a solid donor species and the holes are transported to the counter electrode.[85–87]

The kinetics of charge transfers upon photoexcitation (1) in a liquid-junction DSC and a ssDSC are shown in Fig. 2. The ultrafast electron injection (2) from the excited state dye into the TiO_2 conduction band (3) is the fastest process in a dye sensitized solar cell and occurs on a timescale of femto- to picoseconds (Fig. 3).[88–92]

In ssDSCs, the dye is regenerated (4) from its oxidized state within a few hundred picoseconds, orders of magnitude faster than in the liquid junction cells, where dye regeneration occurs on the microsecond timescale. This fast regeneration process in solid-state DSCs is attributed to direct hole transfer (*via* an energy gradient) into the HOMO level of a solid-state hole transporter from the oxidized state of the dye molecule, whereas the redox reaction in a liquid-state system is diffusion limited. These extremely rapid regeneration dynamics lead to a rapid hole injection from the oxidized dye into the HTM essentially on the same time scale as the electron injection.[46,93,94] The redox mediator or HTM is finally regenerated by charge transfer at the counter electrode (5). Recombinative charge transfers (drawn as red arrows) from the dye (a) and TiO_2 (b) to the redox electrolyte/HTM or from TiO_2 to the ground state of the dye impede the solar cell performance (see Section 2.4 on Limitations of ssDSCs).

Bach *et al.* reported 50%-hole injection within 900 ps from the oxidized **N3** dye to **spiro-OMeTAD**.[85,95–97] In fact, dye reduction (or hole injection to the HTM) may occur before electron injection into TiO_2. Cappel and coworkers found that in a perylene-sensitized TiO_2/**ID176**/**spiro-OMeTAD** system electron injection and dye regeneration were complete after 1 ps, based on the observation of the Stark effect, a spectral shift of the dye spectrum caused by the electric field between the electron in TiO_2 and the hole in the HTM.[98,99] Remarkably, much slower (millisecond) regeneration kinetics were reported for **PEDOT** as a polymeric HTM.[40,100] Haque *et al.* found that a driving force of about 0.2 eV is needed for efficient (>85%) dye regeneration by the HTM.[92,101] Freitag *et al.* and Grätzel and coworkers showed slower (μs) regeneration kinetics for copper coordination complexes as HTMs with a driving force of about 0.1 eV for sufficient dye regeneration.[86,87,102–104]

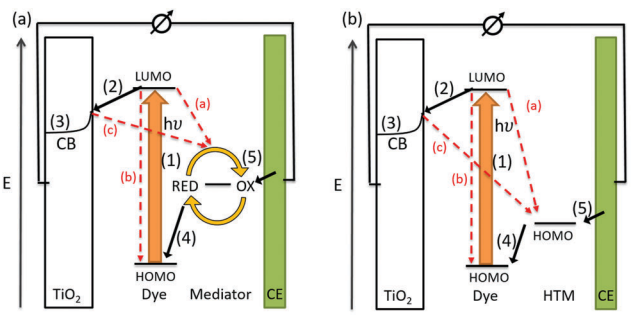

Fig. 2 Schematic drawing of charge transport mechanisms in (a) a liquid-junction DSC and (b) a ssDSC.

Fig. 3 Timescales of charge transfer kinetics in ssDSCs.

2.3. Characterization

A set of techniques to assess the performance of ssDSCs and their components have been developed. Thereby, the power conversion of the solar cell can be evaluated and charge transfer as well as transport processes can be monitored. Furthermore, the performance of single components of a ssDSC can be assessed. The ensuing full-device characterization techniques,

- *I–V* characteristics
- Incident-photon-to-current conversion efficiency (IPCE)
- Electron lifetime are illustrated in the first part of this section. Consequently, component-related techniques
- Photoinduced absorption spectroscopy (PIA)
- Transient absorption spectroscopy (TAS) are introduced.

2.3.1. *I–V* characteristics. The performance of ssDSCs is mostly investigated with a current–voltage (*I–V*) scan under standard 'one sun' AM 1.5G illumination (100 mW cm^{-2}).[105] The efficiency

$$\eta = \frac{P_{max}}{P_{in}} = \frac{J_{max} V_{max}}{P_{in}} = \frac{J_{SC} V_{OC} FF}{P_{in}} \quad (1)$$

of the solar cell can be determined as a ratio of the maximum power output P_{max} to the incoming light power P_{in}. This maximum power point (MPP) of the solar cell is reached when the product of J and V reaches its maximum (Fig. 4).

However, as V_{max} and J_{max} are not easily visible in the *I–V* scan, they are not commonly chosen to compare solar cell performances.

At the so-called open-circuit voltage V_{OC}, the voltage output of the solar cell matches the applied potential and the current density vanishes (see Fig. 4). The photovoltage (V_{OC}) is determined by the potential difference between the Fermi levels of electrons in the TiO_2 film and in the hole transporting material. Similarly, the photocurrent density (J_{SC}) is determined based on the incident light harvest efficiency (LHE), charge injection and collection efficiencies. The short-circuit current I_{SC} is recorded at zero potential and commonly normalized by the solar cell area to give a more comparable short-circuit current density J_{SC}. A so-called fill factor (FF) is subsequently introduced to account for ideality of the *I–V* curve. This fill factor represents the ratio of the actual maximum obtainable power (P_{max}, blue rectangle in Fig. 4) to the product of the open circuit voltage and short circuit current (V_{OC}:J_{SC}, green rectangle).

2.3.2. Incident-photon-to-current conversion efficiency (IPCE). The spectral response of ssDSCs can be resolved with incident-photon-to-current conversion efficiency (IPCE) techniques.[106] Therefore, monochromatic light is used to probe the wavelength-specific power conversion of a solar cell. The incident-photon-to-current conversion efficiency

$$IPCE(\lambda) = LHE(\lambda)\varphi_{inj}(\lambda)\varphi_{reg}(\lambda)\varphi_{cc}(\lambda) \quad (2)$$

can be formulated as a product of the efficiencies of the required processes for photon-to-electron conversion (ϕ_{inj}, ϕ_{reg} and ϕ_{cc} represent efficiencies for electron injection, dye regeneration and charge collection at the electrode, respectively). An exemplary IPCE spectrum of ssDSCs and their liquid counterpart is presented in Fig. 5.

Due to faster hole extraction from the dye molecules and faster conduction in the solid HTM compared to the diffusion-based liquid electrolyte, an increase in power photon-to-current conversion efficiency is observed over the entire absorption range of the **LEG4** dye.

The IPCE should, in turn, be integrated with the spectral flux distribution of sunlight Φ_{sun} to match the short circuit current density

$$J_{SC} = e\int IPCE(\lambda)\phi_{sun}(\lambda)d\lambda, \quad (3)$$

where e is the elementary charge. It should be noted at this point that common DC-IPCE spectra are often reported at lower light intensities. In the case of liquid electrolyte-based DSCs, mass transport in the redox electrolyte does not impede the photon-to-current conversion at low incident photon rates. The IPCE under full illumination is, however, likely affected by mass transport deficiencies and might thus crucially differ.[108] In ssDSCs, on the other hand, a quasi-linear relation between light intensity and photocurrent is expected.[109]

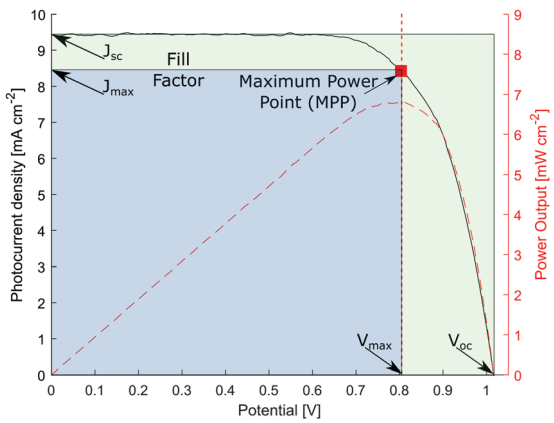

Fig. 4 Characteristic *I–V* scan of a ssDSC.

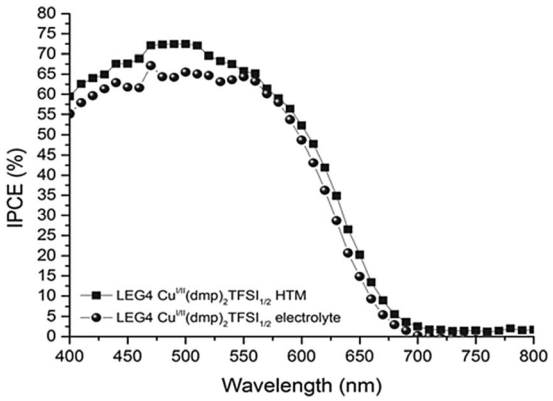

Fig. 5 Incident-photon-to-current conversion efficiency spectra of DSCs sensitized with the organic **LEG4** dye and using copper phenanthroline as a liquid-electrolyte (circles) and a solid-state HTM (squares). Reproduced from ref. 107 with permission from the Royal Society of Chemistry.

2.3.3. Electron lifetime. The lifetime of hot electrons after injection into the TiO_2 layer in ssDSCs is an important parameter to examine the effect of charge back-transfer to the HTM. Commonly, pulsed or square-wave modulated light is used, while the cell is kept under open-circuit conditions, to temporarily accumulate electrons in the TiO_2 layer.[110] When the light is switched off, the electrons recombine with the oxidized sites in the HTM and the V_{OC} is traced to obtain the electron lifetime τ_e as

$$\tau_e = -\frac{k_B T}{e}\left(\frac{dV_{OC}}{dt}\right)^{-1} \quad (4)$$

with Boltzmann's constant k_B, temperature T and elementary charge e.[15] Electron lifetime measurements are commonly presented *versus* the solar cell's V_{OC} or the Fermi level of TiO_2, as shown in Fig. 6.

At high irradiation intensities (and hence high V_{OC}), a high carrier density in the TiO_2 layer increases the rate of recombination with oxidized dye molecules or the HTM. Thus, the lifetime of electrons is comparably low with respect to lower V_{OC}.

2.3.4. Dye regeneration. Besides tracking the kinetics involving hot electrons in the TiO_2 layer, the regeneration of the (after electron injection) oxidized dye molecules plays a crucial role in the performance of a ssDSC. Photoinduced absorption spectroscopy (PIA) enables evaluation of the performance of dye regeneration by the HTM.[111] Commonly, a modulated LED is used to excite the majority of dye molecules (*i.e.* 'pump' the system). The absorption spectrum of the oxidized dye species is probed by a white light source (Fig. 7a).

An exemplary photoinduced absorption spectrum is shown in Fig. 8.

The observed spectral change in absorption upon excitation usually closely matches the absorption spectrum of the oxidized dye species (blue in Fig. 8). In contact with an HTM, however, the dye molecules are regenerated on a nanosecond timescale. The oxidized dye molecules are 'quenched' and their absorption is no longer visible in the photoinduced absorption spectrum. As illustrated in Fig. 3 in Section 2.2, the dye regeneration is accelerated in ssDSCs compared to their liquid-electrolyte counterparts. Therefore, the average lifetime of the oxidized dye species is reduced and the characteristic absorption features of the dye vanish (Fig. 8). Photoinduced absorption spectroscopy can furthermore be used to investigate pore filling of the hole transport material (Section 3.2) in a ssDSC, as dye molecules which are not in contact with the HTM will remain oxidized on a microsecond timescale.

Characteristic absorption bands in the oxidized dye spectrum can then be chosen to directly determine the time constants of electron transfer with transient absorption spectroscopy (TAS).[112] A schematic experimental setup is drawn in Fig. 7b. In this technique, a sensitized semiconductor oxide is excited with a nanosecond laser pulse and the decay of the oxidized dye absorption is monitored to compare regenerative charge transfer and recombinative processes.[86,113] An exemplary spectrum is presented in Fig. 9.

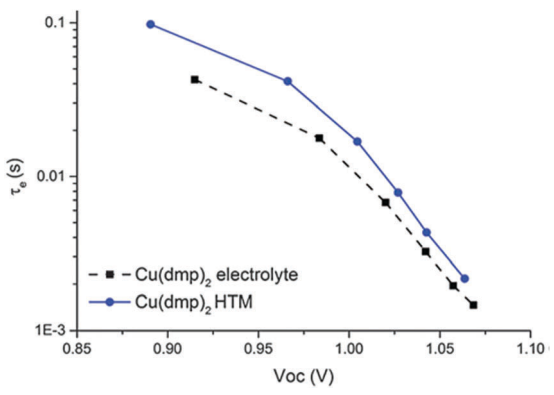

Fig. 6 Electron lifetime in **LEG4**-sensitized solar cells with copper phenanthroline as a liquid electrolyte (circles) and a solid-state HTM (squares). Reproduced from ref. 107 with permission from the Royal Society of Chemistry.

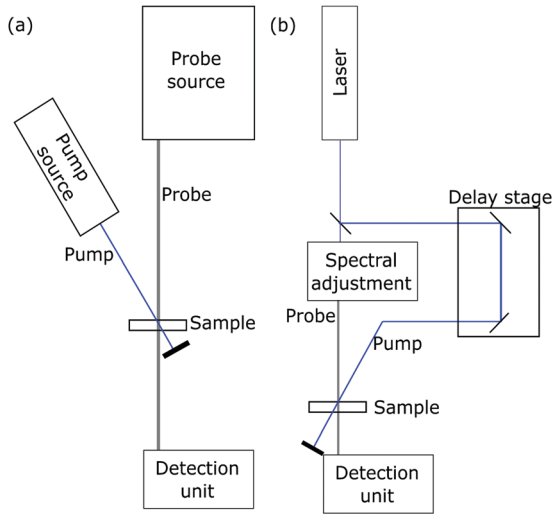

Fig. 7 Schematic setup for (a) photoinduced absorption and (b) transient absorption measurements.

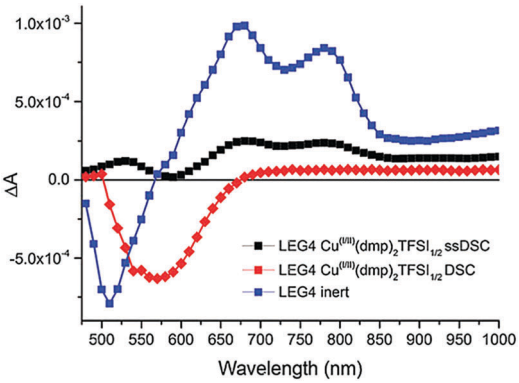

Fig. 8 Photoinduced absorption spectra of **LEG4**-sensitized TiO_2 photoanodes (blue) as well as in contact with copper phenanthroline complexes in liquid junction (red) and solid-state (black) DSCs. Reproduced from ref. 107 with permission from the Royal Society of Chemistry.

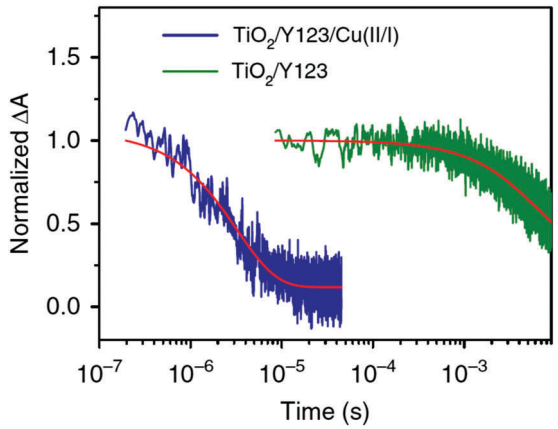

Fig. 9 Transient absorption spectra of **Y123**-sensitized photoanodes inert (green) and in contact with the solid $\mathbf{Cu^{II/I}(tmby)_2}$ hole transport material. Reproduced from ref. 87 with permission from the Nature publishing group.

Thus, it can be determined that the oxidized **Y123**-species is regenerated by the $\mathbf{Cu^{II/I}(tmby)_2}$ HTM on a nano- to micro-second timescale, while the oxidized dye species prevails up to milliseconds when electrons in the TiO_2 layer recombine with the oxidized dye.

2.4. Limitations of ssDSCs

Despite continuous research and progress, the highest performing ssDSC is at 11.7%,[103] lagging behind emerging hybrid organic inorganic perovskite-based solar cells or conventional silicon-based solar cells. The optimal band gap for a sensitizer dye follows the Shockley–Queisser limit, which determines the theoretical optimum band gap of a single absorbing material to be 1.1 electron volt (eV).[114–116] This theoretical limit predicts a maximum conversion efficiency just above 30% with a band gap of 1.4 eV (at AM 1.5 solar spectrum) for a perfect absorber in an ideal solar cell. The limitations in performance of DSCs are largely determined by imperfect energy-level alignment between the individual components, as well as the underlying kinetics of the charge separation and charge-transfer processes.[15,32,115]

It is well known that the main limitations in solid-state DSCs are with respect to (a) photocurrent, (b) potential and (c) fill factor.

(a) The photocurrent largely depends on the photoanode or the working electrode. Improving the light management will likely lead to higher photocurrent. This includes implementation of wide spectral range and high absorbing dyes as well as optimization of the semiconductor morphology with scattering layers, photonic crystals and plasmonics.[32,117,118] Currently, the photocurrent is further limited by relatively thin semiconductor layers, where the thickness is optimized to about 2 μm to enable sufficient pore-filling and low series resistance by the HTM. This thickness is not enough to absorb and convert enough incident light to yield efficiencies above 10%. The pore-filling effect has recently been investigated, confirming that a better performing solar cell device can be obtained by increasing the amount of **spiro-OMeTAD** inside the pores.[46,70,119]

(b) The limitations in potential can be overcome by lowering the driving force for dye regeneration to increase V_{OC}. The ideal theoretical open-circuit potential (V_{OC}) of ssDSC is where no back flow of current exists, which in real DSCs is limited by recombination reactions, specifically between the excited dye and the HTM. The same higher rate of electron recombination also limits the device efficiency for ssDSCs based on **spiro-OMeTAD**. Synthetic modifications of dyes and HTMs can reduce the recombination and improve V_{OC}.[86,87,107]

(c) The fill factor is limited by recombination processes between metal oxide and HTMs, resulting in dark currents as well as series resistance. Both influences are likely to be diminished by improving the morphology of the photoanode (blocking layers) as well as the choice and morphology of the counter electrode to ensure better contact with the HTM.[120]

3. Material development

3.1. Photoanode

3.1.1. Blocking layer. The TiO_2 compact layer (also called TiO_2 blocking layer or TiO_2 dense layer) is the first layer on the conducting working electrode substrate. It is used to block direct contact between the FTO and the HTM. HTMs, like **spiro-OMeTAD**, exhibit an ohmic-contact resistance at junctions with a metal like FTO glass. The FTO–HTM contact can also lead to increased charge recombination in a bulk device to lower the open-circuit voltage. To address these limitations, a pin-hole-free thin TiO_2 layer is deposited on the FTO before applying the nanoporous TiO_2 layer.[90] Several deposition methods for the TiO_2 compact layer have been investigated, including reactive sputtering, spray pyrolysis, metal–organic chemical vapor deposition, dip-coating, spin-coating and atomic layer deposition.[40,120,121] Fig. 10 shows the electron microscopy images of FTO substrates without (a) and with TiO_2 blocking layers of increasing thickness (b–d).

A commonly used titanium precursor is a diluted titanium bis-(acetoacetonato)-di-(isopropanoxylate) ethanol solution.

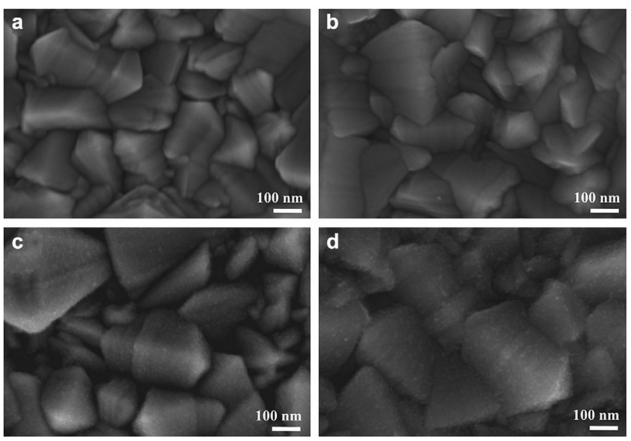

Fig. 10 Scanning electron microscopy images of (a) bare FTO as well as with blocking layers of (b) 13 nm (c) 25 nm and (d) 50 nm titanium dioxide. Reprinted from ref. 122 with permission from Elsevier.

Peng and coworkers optimized the blocking layer to about 150 nm by repetition of spray cycles. Further, the thickness of the compact layer and its surface properties can have a strong impact on the performance of the ssDSC due to the lower roughness of 10 nm in comparison to the 13 nm of the FTO substrates as a result of the smaller TiO_2 particles deposited.[40,120,121]

3.1.2. Nanostructured metal oxide electrodes. Metal oxides, wide band gap semiconductor materials, act as electron acceptors and electronic conduction paths to facilitate diffusion of photo-excited electrons, based on the conductive electronic structure of the valence band (VB) and conduction band (CB). Nanostructured metal oxides are important semiconducting materials for renewable energy applications, including artificial photosynthesis, DSCs, and photocatalysis. Accurate adjustment of the optical and electronic properties of the photoanode can be significant for the performance of the operating devices.

O'Regan and Grätzel pioneered the introduction of nanostructured titanium dioxide (TiO_2) that led to DSCs in 1991, presenting a very large surface area well suited for sensitization by molecular dyes. The nanostructured electrode is crucial, as its morphology drives many physical processes that control the overall device performance: the light-harvesting properties are directly dependent on the amount of surface area available for dyes, and furthermore on the number of free charge carriers, especially electrons. The collected photocurrent is limited by the ability of photogenerated charges to flow through the nanostructured electrode.

Although several alternative metal oxide compounds have been regularly assessed, TiO_2 still demonstrates the best device efficiencies, either in liquid or in solid-state device structures. In TiO_2, the titanium is in oxidation state IV (d^0). The oxide exists in several polymorphs of which two are more relevant: anatase (tetragonal) and rutile (tetragonal). The crystal structures of anatase and rutile are shown in Fig. 11.

For anatase, the band gap is 3.2 eV, slightly larger than that of rutile with 3.0 eV. This transition in the UV region results in an absorption at 390–400 nm. Rutile is the most stable bulk form of TiO_2, but anatase is reported to have better photoactivity and is more stable in nanoparticle form. The n-type TiO_2 photoelectrode nanoparticles offer some unique properties, making them an appropriate semiconductor for DSCs. They have a low intrinsic film conductivity, the small size of the nano-crystalline particles does not support a built-in electric field, and the electrolyte diffuses through the mesoporous network between the electrodes.

The high refractive index of TiO_2 (n = 2.5 anatase) results in efficient diffused scattering of the light inside the porous photoelectrode, which significantly enhances light absorption. Most importantly, mesoporous TiO_2 films have a high internal surface area to support the monolayer of a dye sensitizer, and their conduction band edge lies slightly below the LUMO position of many dye sensitizers.[124] This enables efficient electron injection in the conduction band of semiconductors to transport the electrons through the TiO_2 film by simple diffusion towards the FTO. The capability of the TiO_2 anatase phase to absorb the solar

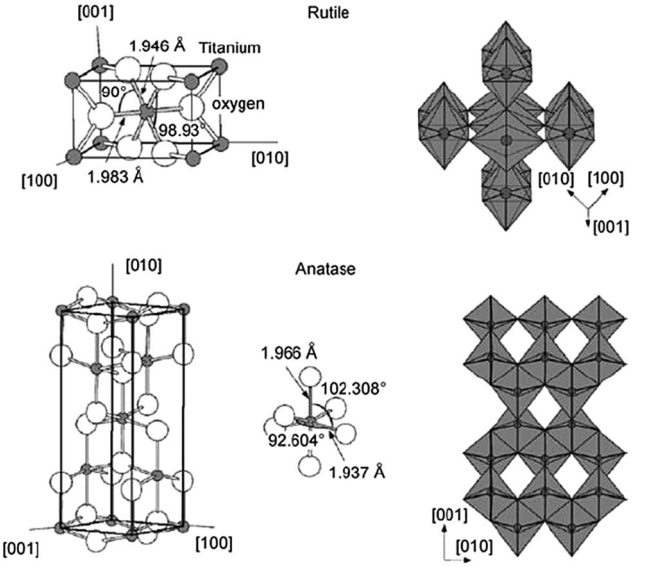

Fig. 11 Crystal structures of rutile (top) and anatase (bottom) phases of titanium dioxide. Reprinted from ref. 123 with permission from Elsevier.

spectrum in the range of ultraviolet or near-ultraviolet radiation can only capture about 4% of solar light. At the same time, the high dielectric constant of TiO_2 (ε = 80 for anatase) provides good electrostatic shielding of the injected electrons from recombination with the oxidized dye.[125]

After the deposition of mesoporous titanium dioxide, a scattering layer of larger particles is commonly deposited to reflect transmitted photons back into the active solar cell volume, as shown in Fig. 12.[126,127]

Many configurations were explored to optimize the morphology and therefore electron transport of mesoporous TiO_2 (Table 1). For example, the nanostructured electrodes were further modified with TiO_2 nanotubes/rods to enhance electron transport through well-aligned pathways (see Fig. 13). Nonetheless, the efficiency obtained by these methods does not compete with nanoporous TiO_2 in ssDSC, because of lower dye loading originating from a loss of semi-conductor/electrolyte surface area. Steiner and Snaith templated TiO_2 into cylinders using block co-polymers. This allowed them to make oriented one-dimensional (1D) columnar structures as well as three-dimensional (3D) bicontinuous gyroid structures. The resulted ssDSCs with a 400 nm thick film sensitized with **D149** (see Fig. 18) showed a PCE of 1.7%,[129] which was later optimized to 3.2% by Docampo *et al.* (see Table 3) employing the indoline **D102** dye (see Fig. 18).[130]

Crossland *et al.* developed mesoporous single crystals of anatase TiO_2, which displayed one order of magnitude higher electron mobility at the same charge density compared to conventional mesoporous TiO_2 layers. Using mesoporous single crystal films processed at low temperatures, the corresponding ssDSCs attained efficiencies of over 3.1%.[131]

Additional modification of the mesoporous TiO_2 film by an ultrathin layer of Al_2O_3 was carried out for ssDSCs initially with inorganic hole transport materials (CuI, CUSCN) and later also with **spiro-OMeTAD**. Apparently, the introduction of the ALD

Table 1 Photovoltaic performance of ssDSCs employing various photoanode materials

Anode	Dye	HTM[a]	CE[b]	V_{OC}[c] (mV)	J_{SC}[d] (mA cm^{-2})	FF[e]	PCE[f] (%)	Ref.
Copolymer templates	**D149**	**Spiro-OMeTAD**	Ag	870	3.7	0.54	1.7	129
Copolymer templates	**D102**	**Spiro-OMeTAD**	Ag	820	7.5	0.53	3.2	130
Single crystal TiO_2	**D102**	**Spiro-OMeTAD**	Ag	760	6.5	0.63	3.1	131
Columnar ZnO	Ru-phospho	CuSCN	C[g]	550	4.5	0.57	1.5	132
ZnO/MgO wires	Ru-NCS-bpy	**Spiro-OMeTAD**	Ag	350	2.3	0.42	0.3	133
ZnO nanowires	**Z907**	**Spiro-OMeTAD**	Au	780	12.2	0.58	5.7	134
SnO_2/Al_2O_3	**N3**	CuI	Au	350	1.7	0.32	0.3	135
SnO_2/MgO	**D102**	**Spiro-OMeTAD**	Ag	470	n.r.[h]	n.r.	1.26	136

[a] Hole transporting material. [b] Counter-electrode. [c] Open circuit voltage. [d] Short circuit current. [e] Fill factor. [f] Power conversion efficiency. [g] Graphite. [h] n.r. = not reported.

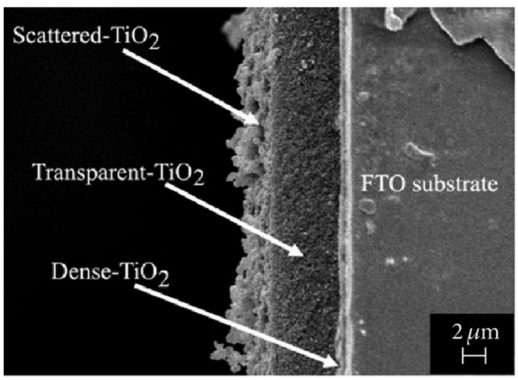

Fig. 12 Cross-sectional electron microscopy image of a DSC photoanode. Reprinted from ref. 128 with permission from Hindawi.

layer of Al_2O_3 improved voltages by slowing down the electron recombination from the TiO_2 and HTM, sacrificing the photocurrent density.[137]

Optimization of the functional properties relies not only on the modulation of the shape and structure of the photoanode, but also on the application of different materials and/or composite systems, which allow a fine tuning of the electronic band structure. Nevertheless, only a few studies explored alternative materials to TiO_2, but the search for increasing the power conversion efficiency (PCE) of ssDSC by incorporating n-type metal oxide semiconductors, such as ZnO, SnO_2, Nb_2O_5, and $SrTiO_3$, continues.[138–140]

Considering its electronic configuration and excellent physical properties, including the high electron mobility ($\sim$100 cm^2 V^{-1} s^{-1}) and conductivity, ZnO is considered more suitable for application in ssDSCs, if the stability issue could be addressed.[132,141–143]

In 2000 O'Regan *et al.* developed a method for electrodeposition of a columnar ZnO structure, which was dye-sensitized followed by electrodeposition of p-type CuSCN to create a complete inner-surface electrical contact, resulting in ssDSC performance of 1.5%.[132] Plank *et al.* reported on ssDSCs based on ZnO nanowires grown using hydrothermal methods,

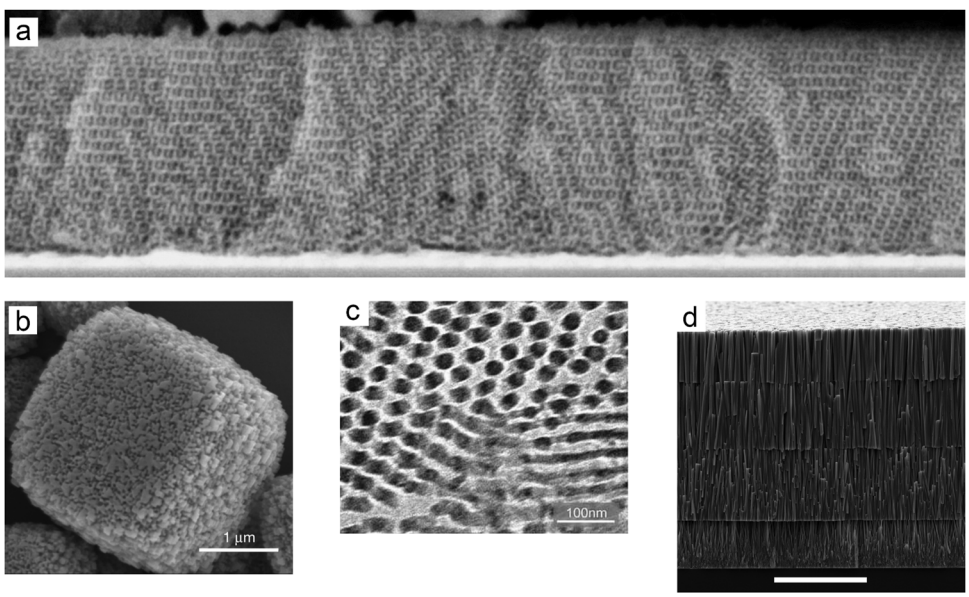

Fig. 13 Different structures of the mesoporous layer. (a) SEM image of TiO_2 gyroid networks. Reprinted from ref. 129 with permission from the American Chemical Society. (b) SEM image of TiO_2 mesoporous single crystals. Reprinted from ref. 131 with permission from Springer Nature. (c) TEM image of cylindrical porous TiO_2. Reprinted from ref. 130 with permission from Wiley. (d) SEM image of the ZnO nanowire array. Reprinted from ref. 134 with permission from the American Chemical Society.

resulting in ssDSC devices with 0.3% efficiency when an ultrathin MgO or ZrO_2 shell was applied.[133] Gao and coworkers developed multilayer TiO_2-coated ZnO nanowires, grown in a sequence fashion to reach 50 μm length, using a newly developed multistep HTM filling process. In conjunction with the **Z907** dye, the resulting ssDSC attained 5.7% efficiency.[134]

A heterojunction of n-SnO_2/Al_2O_3/Ru-dye/p-CuI, where the dye is coated on a thin film of Al_2O_3 first deposited on SnO_2, was introduced by Tennakone *et al.* The ssDSCs delivered a short-circuit current density of 1.7 mA cm^{-2} and an open-circuit voltage of 350 mV.[135] Docampo *et al.* used **spiro-OMeTAD** as the HTM on a SnO_2-based ssDSC resulting in a performance of 1.26%. The addition of a mesoporous Al_2O_3 layer on top of the SnO_2 mesoporous film led to suppression of recombination of the separated carriers.[136]

Another way to increase solar cell efficiency through modification of the mesoporous layer is to "dope" TiO_2 with materials that interact with light, such as metal nanoparticles and photonic crystals. In the case of metal nanoparticles, such materials are deposited on the mesoporous TiO_2 surface and they enhance dye sensitizer absorption by acting as subwavelength antennas. Through the generation of surface plasmons, these metal nanoparticles contribute to light absorption, reflection and scattering, contributing to the generation of more electrons.[144] In ssDSCs, Brown *et al.* obtained an increase in average efficiency from 1.2% to 2.2% after depositing Au nanoparticles with a SiO_2 shell on the mesoporous titania layer.[145] Such devices employed **Z907** as the dye and **spiro-OMeTAD** as the HTM. Arof and coworkers employed Ag nanoparticles in a device with the **N3** dye and a polymer electrolyte to obtain an increase in efficiency from 0.78% to 1.13%.[146] Photonic crystals are periodic nanostructures that can interact with light and affect its propagation. In dye-sensitized solar cells they are deposited on top of the TiO_2 mesoporous layer to reflect and diffract light at specific wavelengths, increasing dye performance.[147,148] In solid-state devices, photonic crystals were employed by Chung *et al.* with an increase in solar cell efficiency from 9.3% to 10.2%[33] and by Lee *et al.*, with an efficiency increase from 6.9% to 7.8%.[149]

3.1.3. Sensitizers. The sensitizer is an essential component to absorb light in the DSC, converting the incident light into photocurrent. Its properties have considerable effect on the light harvesting efficiency and the overall power conversion efficiency. The role of the sensitizer is not only in light harvesting but also in charge injection. As for any single junction photovoltaic cell, the ideal sensitizer is an absorber that converts standard global AM 1.5 sunlight into electricity and absorbs all light below a threshold wavelength of about 920 nm. In addition, the sensitizer must also carry anchoring groups such as carboxylate or silyl to firmly adsorb onto the semiconductor oxide surface.[150,151] The dye molecules are adsorbed onto the mesoporous TiO_2 film by simply immersing in a dye solution. In order to maximize the injection of excited electrons from the dye into the conduction band of TiO_2, the dye molecules should be strongly bonded and uniformly coat the surface of the nanoparticle.[78,152–154]

For liquid junction dye-sensitized solar cells, high power conversion efficiencies are mostly obtained using ruthenium complexes as sensitizers, but recently a new record was set using co-sensitization of zinc porphyrin with an organic dye. Good progress is also made with pure, metal-free, organic sensitizers. While large numbers of sensitizers are being reported every year, only a few of them are routinely screened in the ssDSC configuration, leaving the overall ssDSC efficiency lagging behind that of its liquid electrolyte counterpart. The dye design plays an even greater role in the ssDSC. Not only does the dye require optimized HOMO/LUMO energy levels, but it also needs to provide high oscillator strength to be able to capture sufficient light even at thin electrode thicknesses.[57] Dye molecules also need to supply sufficient surface protection on the TiO_2 electrode to reduce interfacial recombination, have a significant dipole moment to permit for an upward shift in the TiO_2 conduction band as well as to facilitate the wetting process of the hole transporting material within the mesoporous structure. Small molecules adsorbed on the TiO_2 surface along with the dye can also affect the conduction band edge through their dipole moment.

The sensitizers can be divided into inorganic-based dyes and organic dyes according to the chemical structure. Ruthenium and osmium complex sensitizers are the representative inorganic dyes and their properties have been investigated and improved systematically.[16,57,59–63] There are also many studies on purely organic dyes with good photovoltaic performance. Organic dyes are easy to synthesize, their properties can be easily tuned and they have lower cost compared with ruthenium sensitizers.[118,153,155] The film thickness is a critical point in our ssDSC device, therefore a high extinction coefficient dye can enhance the photocurrent and lead to higher overall efficiency with a small amount of dye. So far, organic dyes have made it possible to reach the highest power conversion efficiencies of over 11% for ssDSCs.[87,103] In general, dye molecule design makes it possible not only to selectively change the absorption range of the dye, but also to modify the energy levels.

3.1.3.1. Metal coordination complexes. The first dyes used in DSCs were ruthenium-based dyes and therefore metal coordination complexes. These ruthenium complexes have received particular interest as photosensitizers for having advantageous characteristics such as wide absorption bands, high external quantum efficiencies, favorable energy levels and relatively long excited state lifetimes. Among several Ru complexes, Ru complexes with carboxylated bi- or poly-pyridine ligands such as **N3**, **N719**, **CYC-B11**, **Z907** and **Z910** were extensively studied (Fig. 14).[156]

Ru-based dyes are capable of yielding conversion efficiencies greater than 10%, in liquid junction DSCs. However, the Ru-dyes have low extinction yields, which is a limitation, because the ssDSCs require thinner mesoporous layers of a semiconductor for better pore filling.

In one of the first reports of efficient ssDSCs, Bach *et al.* used the Ru-dye **N3** in combination with the organic HTM **spiro-OMeTAD** and a PCE of 0.74% (Table 2) was obtained at an intensity of 9.4 mW cm^{-2}.[85] Later, the partially deprotonated

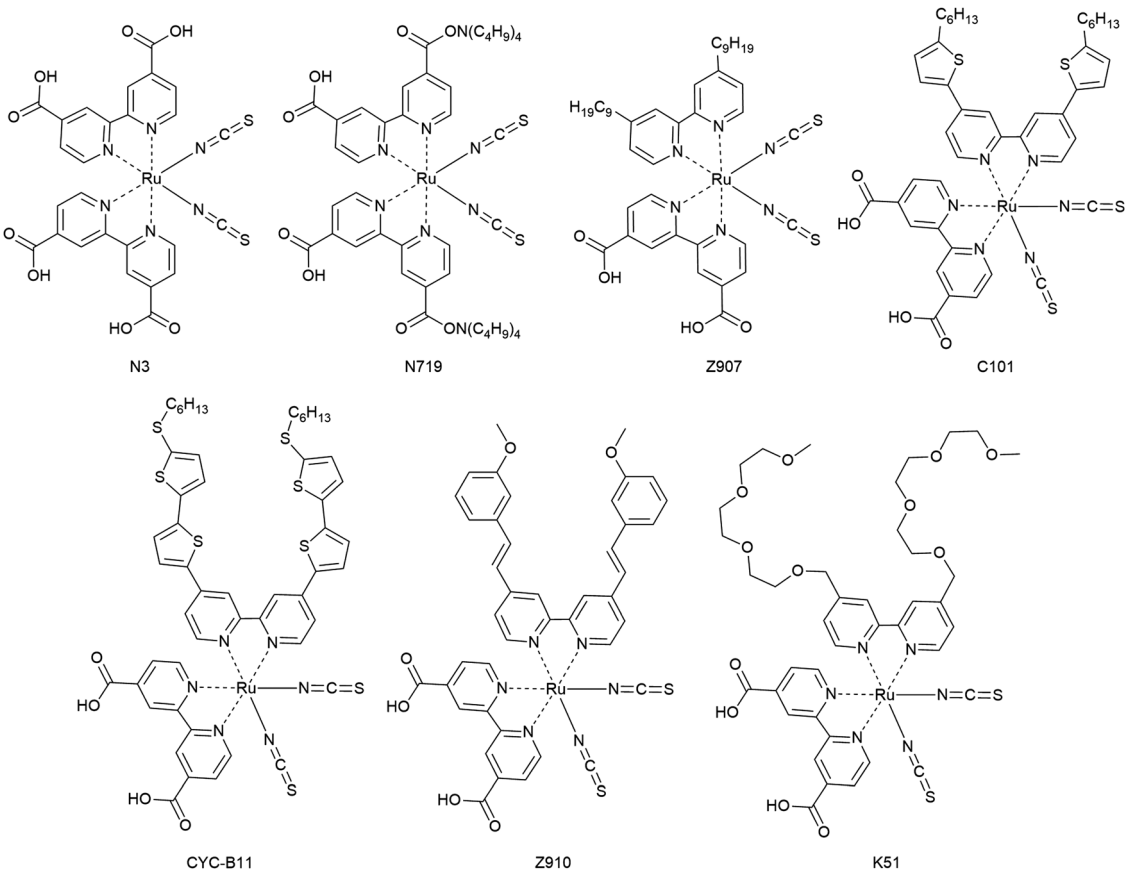

Fig. 14 Chemical structures of ruthenium-based sensitizers for ssDSCs.

Table 2 Photovoltaic performance of ssDSCs with metal-complex sensitizers

Dye	HTM[a]	Additives[b]	CE[c]	V_{OC}[d] (mV)	J_{SC}[e] (mA cm^{-2})	FF[f]	PCE[g] (%)	Ref.
N3	**Spiro-OMeTAD**	Sb, Li	Au	340	0.32	0.62	0.74	85
N719	**Spiro-OMeTAD**	Sb, Li, *t*BP	Au	910	5.1	0.57	2.6	97
N719	**Spiro-OMeTAD**	Sb, Li, *t*BP	Au	930	4.6	0.71	3.2	157
Z907	**Spiro-OMeTAD**	Sb, Li, *t*BP	Au	750	8.3	0.64	4.0	158
K51	**Spiro-OMeTAD**	Sb, Li, *t*BP	Au	880	6.8	0.65	3.8	159
CYC-B11	**Spiro-OMeTAD**	Li, *t*BP	Au	830	9.2	0.63	4.7	160
C101	**Spiro-OMeTAD**	n.r.[h]	Au	800	8.2	0.69	4.5	161
YD-o-C18	**Spiro-OMeTAD**	n.r.	Ag	n.r.	n.r.	n.r.	4.1	162
KS	**Spiro-OMeTAD**	Li, *t*BP, Co	Au	849	11.0	0.53	5.1	163
FA	**Spiro-OMeTAD**	Li, *t*BP, Co	Au	786	10.5	0.54	4.5	163

[a] Hole transporting material. [b] List of additives: Sb = $N(PhBr)_3SbCl_6$, Li = LiTFSI, *t*BP = 4-*tert*-butylpyridine, Co = **FK102**, FK209 or **FK269**. [c] Counter-electrode. [d] Open circuit voltage. [e] Short circuit current. [f] Fill factor. [g] Power conversion efficiency. [h] n.r. = not reported.

form of **N3**, namely **N719,** was used and with careful optimization of the additive *tert*-butylpyridine (*t*BP) a certified efficiency of 2.56% was obtained for a solar cell device with an active area of 1.07 cm^2.[97] To solve the issue of rather low photocurrents, studies with addition of coadsorbents, increasing ligand length by extension of the conjugated system, cosensitization, and the use of a near-IR absorbing dye, known as a black dye, were reported. In particular, the additive *t*BP plays a crucial role in the inhibition of the interfacial electron recombination.

In 2005, the amphiphilic dye **Z907** with hydrophobic tails was introduced in ssDSCs and a PCE of 4.0% was obtained. The enhanced photovoltaic performance of ssDSCs was attributed to the dense packing of dyes on the surface of TiO_2 as well as the hydrophobic isolating chains which block the direct contact between **spiro-OMeTAD** and TiO_2.[158] Inspired by this, the effect of the hydrocarbon chain lengths on the Ru-dye was systematically investigated, and it was confirmed that the hydrophobic chains act as an insulating barrier between TiO_2 and the HTM, and can efficiently suppress the interfacial electron recombination, as demonstrated by detailed studies *via* transient absorption results.

Another strategy is to improve dye packing and blocking properties towards the HTM on the mesoporous surface. This was achieved by implementation of amphiphilic, heteroleptic

ruthenium sensitizers with hydrophobic spacers. Efficiencies over 7.8% were reported with an ion-coordinating sensitizer (**K51**) containing triethylene oxide methyl ether (TEOME) at the 4,4-position of a 2,2-bipyridine ligand; this enables the dye to prevent the ions from reaching the semiconductor interface.[159]

In the **CYC-B11** dye, bithiophene groups were added, resulting in a good molar extinction coefficient (2.42×10^4 M^{-1} cm^{-1} at 554 nm) and a high PCE for ssDSCs of 4.7%.[160] Alkylthiophene-containing groups were added to the bipyridine ligand by Peng Wang and co-coworkers in order to increase the extinction coefficient of **Z907**, resulting in **C101** with an enhanced performance of 4.5% compared to 2.9% for **Z907**.[161]

Other issues in considering Ru-based dyes are their cost as Ru is a rare metal with high price and toxic nature. Thus, research into Ru free dyes, metal-complex porphyrin dyes, has intensified.[162,163]

Unlike ruthenium systems, the porphyrin exhibits strong absorption in the near-IR region due to an additional Q-band in the 500–700 nm region with good stability. The asymmetric porphyrin dye (**YD2-o-C8**, Fig. 15) was synthesized by introducing triarylamine as an electron donor and carboxylic acid as an acceptor. Porphyrins have been designed and synthesized based on the molecular structure of **YD2-o-C8** for applications in DSCs to reach a PCE of 13% using a cobalt-based liquid-type electrolyte.[19]

The **LD14** was modified for the use in ssDSC by a functional group inserted into the position between the porphyrin core and the donor group; the resulting device attained a PCE of 4.1% with **spiro-OMeTAD** as the HTM. The performance was still lower in comparison to **LD14** in liquid junction DSCs, where a PCE of 9.2% was attained.[156,164,165] Another modified push–pull porphyrin was designed having a benzothiadiazole (BTD) group between the porphyrin core and the acceptor anchoring group. The ssDSC achieved a PCE of 5.5%, when the porphyrin dye was co-sensitized with an organic dye.[162] Both time-resolved transient absorption spectroscopy and frequency-domain electrochemical impedance spectroscopy techniques were applied to understand charge transport and recombination kinetics with respect to their photovoltaic performances.

Peng Qin *et al.* recently reported molecularly engineered weakly conjugated hybrid porphyrin dyes (**KS** and **FA**) as efficient sensitizers for solid-state dye-sensitized solar cells. By incorporating a quinolizino acridine and triazatruxene based unit as the secondary light-harvester as well as an electron-donating group at the *meso*-position of the porphyrin core efficiencies of 4.5% and 5.1% were achieved in ssDSCs (Table 2).[163]

3.1.3.2. Organic dyes. Sensitizer development for ssDSCs is largely focused on metal-free dyes, since higher efficiencies were recently reached in combination with hole transport materials based on metal coordination complexes.[166] Their success, especially over the ruthenium based systems, can be attributed to the following characteristics:

(1) The organic dyes show a large variety in terms of sensitizer families (indolines (**D149**, **ID176**), triphenylamines, coumarine, arylamines (Fig. 18)).[36,98,99,153,167] The ease in their design and synthesis leads to a large variety of characteristics.

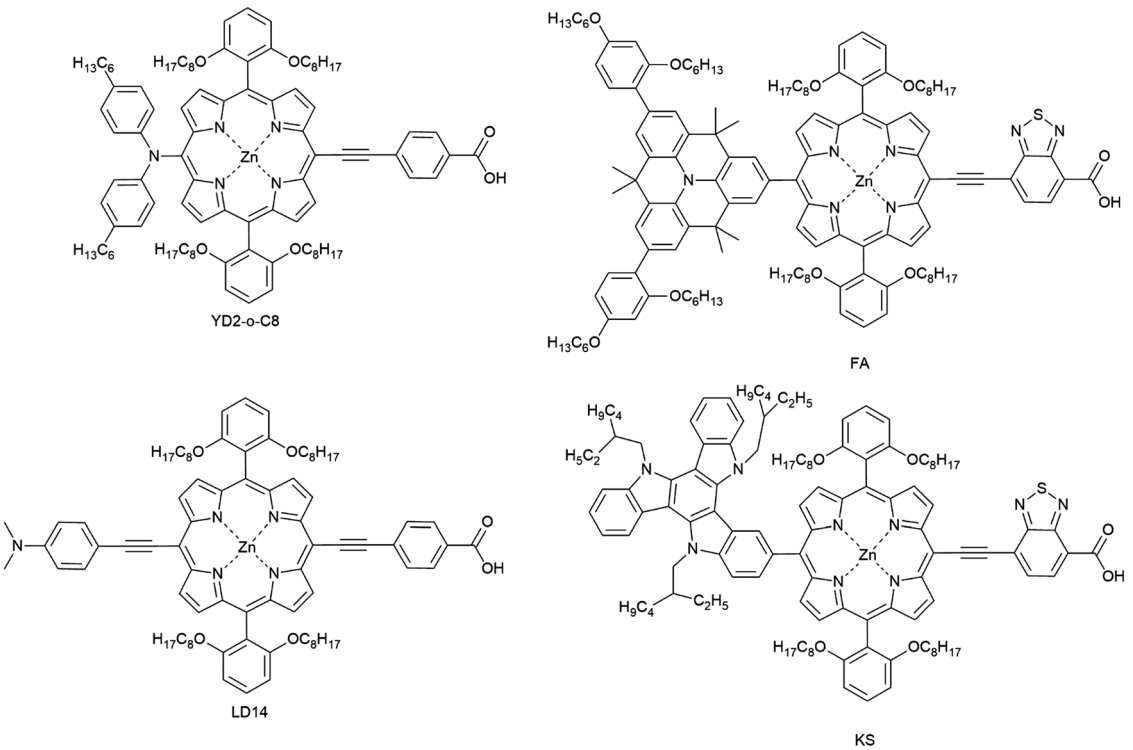

Fig. 15 Chemical structures of porphyrin-based sensitizers for ssDSCs.

(2) The organic dyes have generally higher extinction coefficients (the most efficient ssDSC incorporated 55 800 M^{-1} cm^{-1} **LEG4** and 70 100 M^{-1} cm^{-1} **XY1** as well as 68 800 M^{-1} cm^{-1} **XY1B**).[34,41,168] The high molar extinction coefficients are especially desirable for thin TiO_2 films in ssDSCs. For instance, indoline dye **D102**[169] has a very high extinction coefficient of 55 800 M^{-1} cm^{-1} at 491 nm, which yields over 90% absorption over a broad spectral range when sensitizing TiO_2 films are as thin as 2 μm. However, for the ruthenium sensitizers, the TiO_2 film of 10 μm thickness is required to get the same absorption.[38,39,158,170]

(3) Organic dyes lack the precious metal part, which also makes them more cost efficient and sustainable.[17,171]

Some general principles to design an efficient organic dye and efficient ssDSCs are as follows: a donor–π-bridge–acceptor (D–π–A, D–A–π–A) structure (Fig. 16), which can be easily modified for extending the absorption spectra, adjusting the HOMO and LUMO levels to complete the intramolecular charge separation.[78,118]

Likely donors or the electron-rich groups include: coumarin, indoline, and triarylamine moieties. In particular, triarylamine dyes have been most efficient displaying good power conversion efficiencies in DSCs due to their electron donating ability

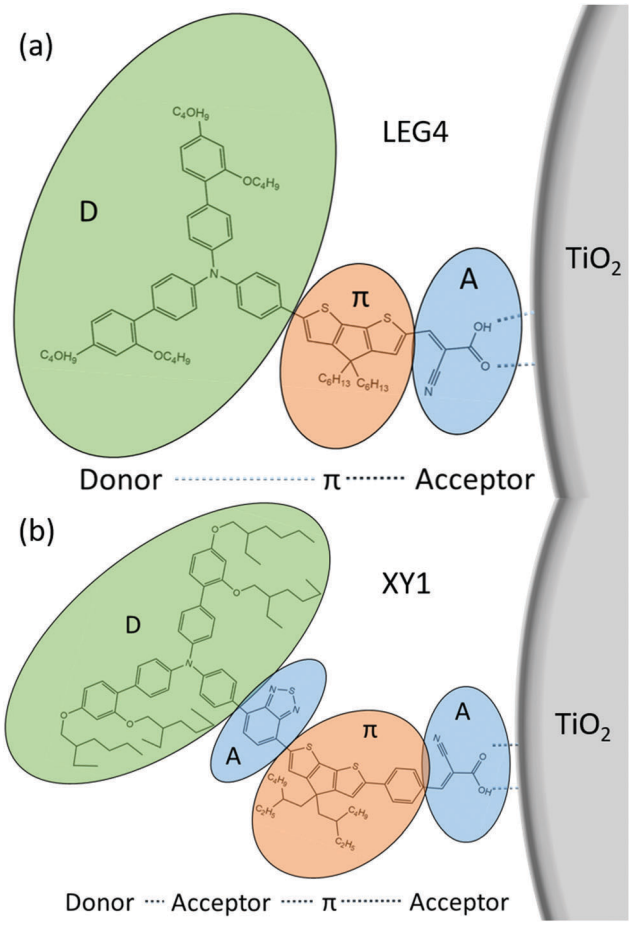

Fig. 16 D–π–A/D–A–π–A structures of the organic dyes (a) **LEG4** and (b) **XY1**.

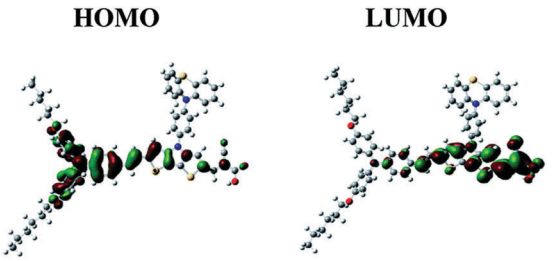

Fig. 17 Orbital distribution in donor–π–acceptor dyes. Reproduced from ref. 174 with permission from the Royal Society of Chemistry.

and hole-transport properties.[172,173] The π-bridge mostly consists of thiophene units, such as oligothiophene, thienothiophene, ethylenedioxythiophene. The favorite acceptor group is cyanoacrylic acid containing a carboxylic acid unit for binding to the metal oxide semiconductor. The electron density of the highest occupied molecular orbital (HOMO) of the dye molecule is mainly located in the donor part, whereas the density of the lowest unoccupied molecular orbital (LUMO) of the dye molecule is mostly located in the acceptor part (Fig. 17).

After the photoexcitation of the dye, the electrons subsequently transfer from the donor to the acceptor through the π-bridge. By this design, the electrons and holes are spatially separated in the dye molecule after light excitation, which could favor charge injection and dye regeneration. The properties of organic dyes can be easily tuned by suitable combination of these three parts.

Although organic dyes have many advantages as sensitizers in DSCs, the efficiency of devices prepared with them has been limited mainly by two factors: first, increasing the size of the conjugated system chain in organic dyes can cause dye aggregation or π–π stacking on the TiO_2 surface due to their planar structures. Dye aggregation results in unfavorable back electron transfer and decreasing cell performance in a DSC. Second, sensitizers reported so far to give high efficiencies mostly have absorption bands below 550 nm, indicating that photons in the longer wavelength region are not absorbed efficiently. They should, however, harvest incident light in a broad spectral range to obtain a high photocurrent. Some organic dyes show a panchromatic response, but the obtained photocurrent and efficiency are not as high as expected due to their low LUMOs, which reduces injection efficiency.

The previously mentioned indoline dye **D102** was also the first efficient organic sensitizer investigated for ssDSCs in 2005. It exhibits a high extinction coefficient of 55 800 M^{-1} cm^{-1} at 490 nm. A PCE of over 4% was obtained by Schmidt-Mende *et al.* (Table 3).[166] Another indoline dye, **D149**, was used as a sensitizer in ssDSCs with CuI as the inorganic HTM, exhibiting a PCE of 4.2%.[175]

Hagfeldt and coworkers investigated a perylene dye **ID176** for ssDSCs. This dye showed a good absorption coefficient (25 000 M^{-1} cm^{-1} at 590 nm) as well as a broad absorption spectrum. Devices with good performance, high photocurrent of 9 mA cm^{-2} and PCE of 3.2% were obtained.[98] An interesting fact of this dye is that it worked well in ssDSCs but not in

Table 3 Photovoltaic performance of ssDSCs with organic sensitizers

Dye	HTM[a]	Additives[b]	CE[c]	V_{OC}[d] (mV)	J_{SC}[e] (mA cm^{-2})	FF[f]	PCE[g] (%)	Ref.
D102	**Spiro-OMeTAD**	Sb, Li, *t*BP	Au	860	7.7	0.61	4.1	166
D149	**CuI**	$(C_2H_5)_3HSCN$	Au	550	14.1	0.54	4.2	175
ID176	**Spiro-OMeTAD**	Li, *t*BP	Ag	640	8.7	0.57	3.2	98
BODIPY-1	**Spiro-OMeTAD**	n.r.[h]	Au	800	2.2	0.37	0.6	176
D35	**Spiro-OMeTAD**	Li, *t*BP	Ag	850	7.2	0.73	4.5	153
C220	**Spiro-OMeTAD**	Li, *t*BP	Au	880	9.7	0.71	6.1	177
Y123	**Spiro-OMeTAD**	Li, *t*BP, Co	Ag	930	9.8	0.75	6.9	178
JD10	**Spiro-OMeTAD**	Li, *t*BP, Co	Ag	710	7.3	0.61	3.6	179
WN3.1	**Spiro-OMeTAD**	Li, *t*BP, Co	Ag	870	9.7	0.75	6.3	180
MK2	**Spiro-OMeTAD**	Li, *t*BP	Ag	700	6.9	0.58	2.8	181
CPDT-3	**Spiro-OMeTAD**	Li, *t*BP, Co	Au	730	10.9	0.47	3.9	154
XY2	**Spiro-OMeTAD**	Li, *t*BP, Co	Au	900	11.0	0.76	7.5	78
S5	**Spiro-OMeTAD**	Li, *t*BP, $C_2H_2Cl_4$	Ag	830	12.9	0.73	7.8	182

[a] Hole transporting material. [b] List of additives: Sb = $N(PhBr)_3SbCl_6$, Li = LiTFSI, *t*BP = 4-*tert*-butylpyridine, Co = **FK102**, FK209 or **FK269**. [c] Counter-electrode. [d] Open circuit voltage. [e] Short circuit current. [f] Fill factor. [g] Power conversion efficiency. [h] n.r. = not reported.

liquid DSCs. By detailed time-resolved absorption spectroscopy measurements it was found that (a) the dye **ID176** regeneration by solid-state **spiro-OMeTAD** was ultrafast, and (b) lithium ions are necessary for efficient electron injection in the device.

Triphenylamine (TPA) based dyes are the most successful organic dyes due to their structural versatility and high absorption coefficients.[107,182–184] The implementation of the TPA dyes started with the work by Hagfeldt and coworkers with the **D35** dye and its bulky *o*,*p*-dibutoxyphenyl groups. The **D35**-based devices showed a promising PCE of 4.5%, due to improved electron lifetime in the device.[153] Inclusion of a 4,4′-didodecyl-4*H*-cyclopenta[2,1-*b*:3,4-*b*′]dithiophene (CPDT) conjugated linker improved the absorption spectrum of the TPA dye C220. Using such a modified dye a certified PCE of 6.1% was achieved by Cai *et al.* in 2011.[177] With the **Y123** dye a PCE of 6.9% was achieved by Dualeh *et al.* in a study based on the investigation of the donor influence on the V_{OC} of the ssDSCs.[178] Sellinger and coworkers obtained a PCE of 6.3% in ssDSCs based on dye **WN3.1** with alkyl chains, which were instrumental in suppressing unwanted recombination processes.[180]

The modified, donor-free **MK2** dye was introduced by Abate *et al.* consisting of cyanoacrylic acid-functionalized oligo (3-hexylthiophene). The modification of the dye had a long-lived oxidized state and this led to increased V_{OC} and PCE in ssDSCs.[181] Yue Hu *et al.* reported another series of 'donor-free' dyes featuring moieties of extensions of oligo(4,4-dihexyl-4*H*-cyclopenta[1,2-*b*:5,4-*b*′]-dithiophene) (**CPDT-1**, **CPDT-2**, and **CPDT-3**) with molar absorption coefficients of up to 75 000 M^{-1} cm^{-1}. ssDSCs with **CPDT-3** and **spiro-OMeTAD** hole transporter resulted in devices with a PCE of 3.9%.[154]

Very recently, He Tian and coworkers developed a series of dyes featuring benzothiadiazole (BTZ), 2,3-diphenylpyrido[3,4-*b*]-pyrazine (PP) or 2,3-diphenylquinoxaline (QT) as the auxiliary acceptors and cyclopentadithiophene (CPDT) as the π-linker with the overall structure D–A–π–A. With the **XY2** dye, having a high extinction coefficient of 6.66 × 10^4 M^{-1} cm^{-1}, and **spiro-OMeTAD** as the HTM a high PCE of 7.5% was obtained.[78] The **XY1** dye from the same study was later used in combination with a copper coordination complex based HTM (see Section 3.2.2.3 on metal complex HTMs) to record efficiencies over 11%.[87]

He Tian and coworkers introduced two novel organic blue-colored dyes **S4** and **S5** with the donor indeno[1,2-*b*]thiophene functionalized triphenylamine, and the acceptors 2,3-diphenylpyrido[3,4-*b*]pyrazine or 2,3-diphenylquinoxaline and cyclopentadithiophene (CPDT) as the π-linker were designed and synthesized for ssDSCs. Both dyes exhibit a very high molar extinction coefficient of 6.3 × 10^4 M^{-1} cm^{-1} at 600 nm. The blue dye **S5** resulted in devices with PCEs of 7.8% in ssDSCs.[182]

Organic metal-free dyes with red or near-infrared (near-IR) absorption have also been employed in ssDSCs. Grätzel and coworkers reported a near-IR absorbing squaraine dye, **JD10**, with strong absorption (672 nm, 2.5 × 10^5 M^{-1} cm^{-1}). By effectively reducing the dye aggregation *via* adding the coadsorber chenodeoxycholic acid in the dye bath, an efficiency of 3.2% was obtained.[179] Kolemen *et al.* developed a series of boron-dipyrromethene (BODIPY)-based molecules as red and near-IR sensitizers for ssDSCs.[176] The devices with these dyes exhibited relatively low incident photon-to-current efficiency in spite of their broad absorption spectra. Further study on the kinetics of the charge transfer at the interfaces is needed to further improve their performance. It should be noted that the red or near-IR absorbing dyes provide more choices for the colors in the solar cell (such as visibly colorless) and are important to broaden the overall absorption spectrum in co-sensitized systems.

3.1.3.3. Quantum dots. Quantum dots (QDs) are inorganic nanoparticles with special electronic and optical properties due to quantum confinement of light capabilities given by their size. Orbitals and electronic behavior inside these nano-sized dots greatly vary compared to a bulk crystal of the same material. Light absorption properties are different and excited states are much longer lived, which leads to intense fluorescence upon illumination. These properties make QDs promising materials for photovoltaic applications. As it happened for the perovskite light absorber, QDs were first employed in photovoltaics as dyes in DSCs (Fig. 19), while nowadays the best-performing devices with this technology can have a planar structure and are considered p–n junctions rather than p-i-n junctions as is the case for DSCs.[185–187]

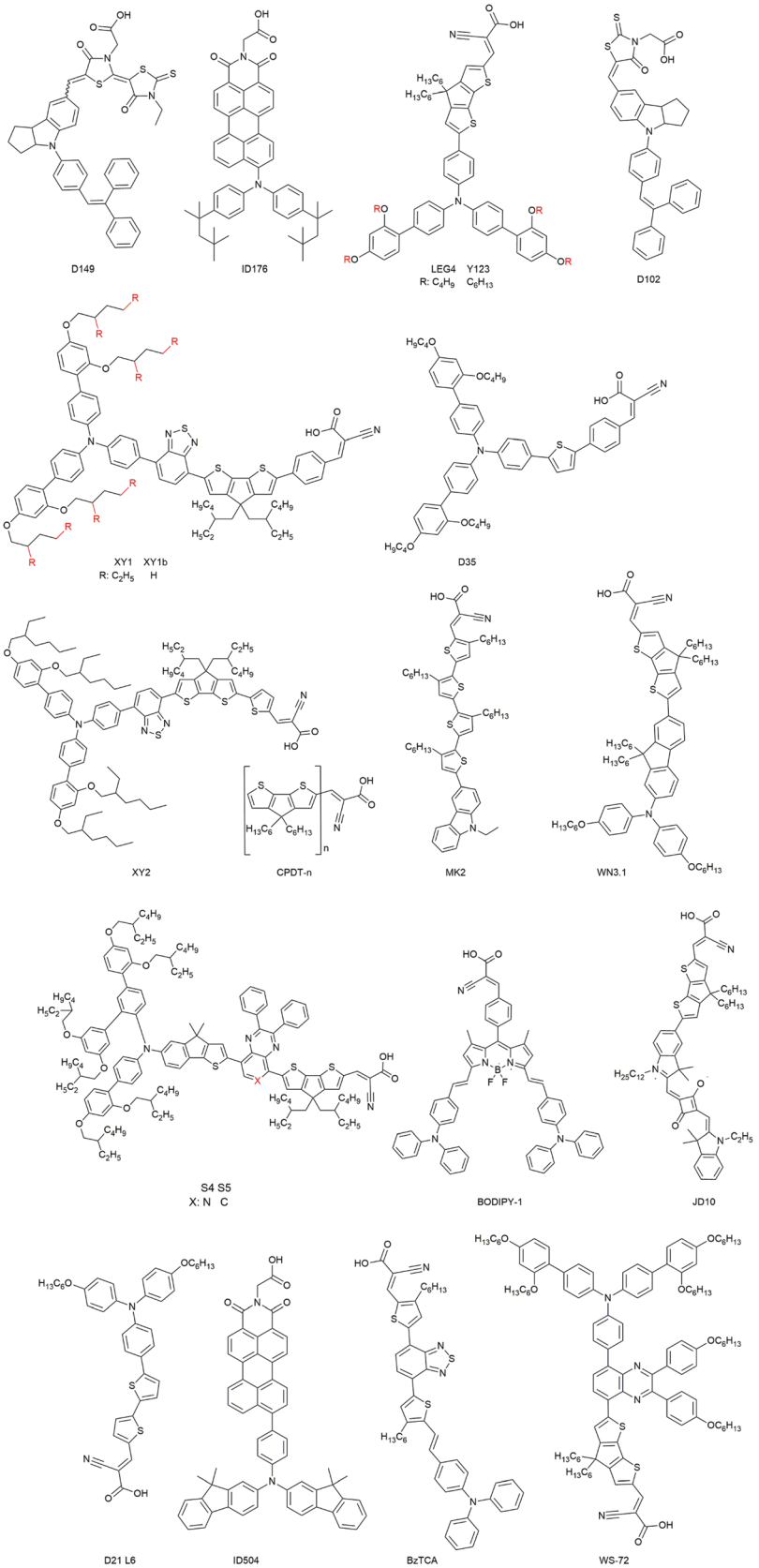

Fig. 18 Chemical structures of organic dyes used in ssDSCs.

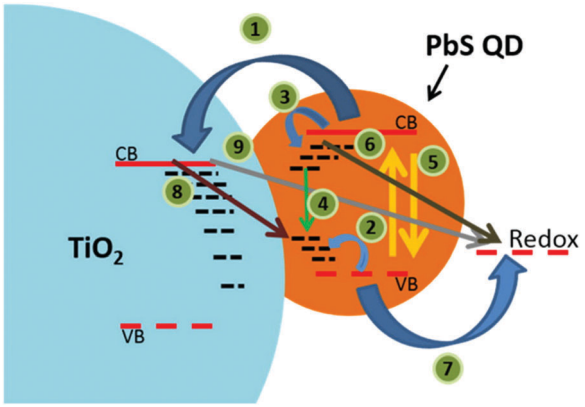

Fig. 19 Schematic illustration of photoinduced charge-transfer processes following absorption of quanta of light by PbS QDs on TiO_2. Reprinted from ref. 190 with permission from the American Chemical Society.

Nonetheless, QD-based DSCs are still actively being developed.[188,189]

In recent advances in solid-state quantum dot-sensitized solar cells (ssQDSCs), Jumabekov *et al.*[190] and Park *et al.*[191] have fabricated devices based on the PbS quantum dot. Jumabekov focused on the stability of the quantum dot by passivating its surface with L-glutathione to avoid surface oxidation. Surface passivation led to a more than doubled short circuit current, for a final device efficiency of 0.95%. Park extended absorption properties in the near-infrared of the PbS quantum dot thanks to the surface plasmon resonance effect by partly exchanging Pb^{2+} cations on the surface with Cu^{2+} cations. The inclusion of Cu produced an overall improvement of device parameters, with the PCE increasing from 2.36% to 8.07% after Cu embedding. Johansson and coworkers grew Ag_2S QDs on ZnO nanowires.[192] They show how the growth conditions for the QD on the nanowire greatly affect the final device. Under the best conditions, they obtained a solar cell efficiency of 0.36%. Finally, Duan *et al.* worked on a CdS QD in a device employing a polymer-based electrolyte.[193] The best performance obtained with this setup was 0.55%.

3.2. Charge transport materials

In DSCs, the role of the redox mediator is to transport charges between the electrodes and regeneration of the oxidized dye. It is a crucial component determining the overall performance of the solar cell. The usage of the liquid solvent and especially of organic solvents, which are usually very volatile, lead to leakage and corrosion of the solar cells and degradation of the dyes.[194] Even though considerable progress has been made in this field of research, fundamental stability considerations represent significant limitations for the commercialization of DSCs. Generally, the electrolytes used in DSCs can be categorized into: liquid, quasi-solid and solid states.[26,195,196] The electrolyte in a liquid junction solar cell consists of a solvent, which can be organic or aqueous, with a redox mediator such as I_3^-/I^-, copper or cobalt coordination complexes or small organic molecules.[17,26] A significant part of the efforts made in this field has been devoted to the development of sustainable and efficient quasi-solid-state and solid-state hole transporting materials (HTMs) based on polymers, small organic and inorganic molecules.[197] The main difference between the various charge transporting materials are the charge transport characteristics.[69,82,198] In the case of polymer electrolytes it can be both ionic and electronic, whereas in others electronic transport is the dominant process.[24,196]

3.2.1. Polymers. Polymer electrolytes (PEs) are a result of the trapping of ionic conductors in a polymer host matrix retaining the beneficial aspects of liquid electrolytes (high ionic conductivity, diffusive transport and interfacial contact properties) in combination with the mechanical benefits such as the durability and flexibility of a polymer.

The incorporation of PEs into ssDSCs made substantial steps forward in the research and development of ssDSCs. Most of the research activities are within the field of solid-state electrochemistry, in which high ion-conducting materials are developed for the energy conversion and storage applications. In this sense, PEs are a class of materials, which have been studied extensively in the last 20 years, to achieve systems with good conductivity and electrochemical stability. Polymer-based electrolytes are usually classified into solid-state polymer electrolytes, quasi-solid state gel polymer electrolytes and their composites.[23,24,26,199,200]

3.2.1.1. Solid polymer electrolytes. Peter V. Wright first showed in 1975 that poly(ethylene oxide) (PEO) can act as a host for sodium and potassium salts, thus producing a solid electrical conductor polymer/salt complex.[201] Later, Armand *et al.* proposed that these systems could be used with graphite intercalation compounds for electrodes and immediately realized that lithium/PEO complexes could be employed as solid electrolytes and applied in batteries.[202–204]

Generally, solid polymer electrolytes (SPEs) are made from inorganic salts dispersed or dissolved in a polar polymer matrix. Most inorganic conductors consist of alkali metal salts (LiI, NaI, $LiClO_4$, $LiCF_3SO_3$, LiSCN, NaSCN, $NaClO_4$, $LiPF_6$, *etc.*) in a host polymer (Fig. 20).

The choice of polymer hosts for PEs is made based on the following characteristics: presence of groups with sufficient polarity to form strong coordinations with cations, and with low hindrance of bond rotations. Poly(ethylene oxide) (PEO) is the

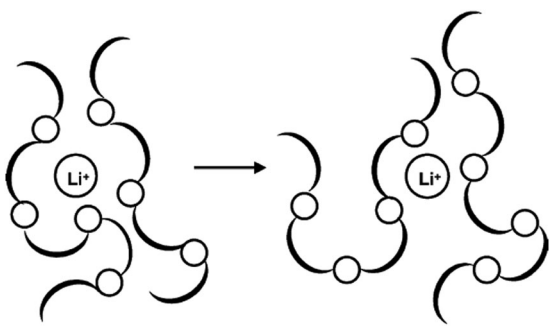

Fig. 20 Schematic drawing of lithium ions embedded in a polymer matrix. Reprinted from ref. 196 with permission from Elsevier.

Table 4 Photovoltaic performance of ssDSCs with solid polymer electrolytes

Polymer	Salt	Dye	V_{OC}[a] (mV)	J_{SC}[b] (mA cm^{-2})	FF[c]	PCE[d] (%)	Ref.
PEO-EPI	NaI/I_2	PAni	48	0.012	0.32	0.00016	209
PEO-EPI	NaI/I_2	PAni	820	4.2	0.47	1.6	210
PEO-TiO_2	Li/I_2	**N3**	664	7.2	0.58	4.2	211
PNR4VPI/NR′PI/I_2		**N719**	682	13.4	0.62	5.6	212
HEII/I_2		**MK2**	733	14.66	0.69	7.5	213
CκC	NaI/I_2	**N719**	510	7.6	0.53	2.1	214

[a] Open circuit voltage. [b] Short circuit current. [c] Fill factor. [d] Power conversion efficiency.

most commonly used host polymer, but these systems usually display low conductivity (10^{-8} S cm^{-1}),[205,206] which can be improved by using blends of different polymers or copolymers, as well as by synthetically modified monomers.[24,207,208] This is necessary, since the required ionic conductivity values for ssDSC are around 10^{-3}–10^{-4} S cm^{-1}.[196]

PE-incorporating DSCs were first reported in 1999 attaining a very low IPCE of 1.3% (410 nm). The PE consisted of poly(*o*-methoxyaniline) (PAni) as the sensitizer and a copolymer of poly(ethylene oxide-*co*-epichlorohydrin) (PEO-EPI), containing NaI/I_2, as the electrolyte (Table 4).[209] Since then, there have been substantial research activities towards the preparation of various types of polymer electrolytes having different combinations of polymers and salts.

In 2000, Nogueira *et al.* prepared an elastomeric polymer electrolyte again based on copolymer poly(ethylene oxide-*co*-epichlorohydrin) complexes with sodium or lithium iodide salts. Unsealed prototype cells showed an efficiency of 1.6% (2.6% at 10 mW cm^{-2}), thus demonstrating that a polymer electrolyte was an alternative as a solid-state electrolyte for ssDSCs.[196,210,215] Falaras and coworkers prepared a solid polymer electrolyte consisting of PEO/TiO_2, LiI, and I_2. In this case, TiO_2 nanoparticles were used as fillers to decrease the crystallinity leading to an increase in ionic conductivity (10^{-5} S cm^{-1}) and consequently an efficiency of 4.2% at 65.6 mW cm^{-2} illumination.[211,216,217]

Wu *et al.* synthesized a polyelectrolyte based on polyvinyl pyridine and used it as a solid-state ionic conductor in ssDSCs. Based on a larger backbone cation poly(*N*-alkyl-4-vinylpyridine) (PNR4VPI) and a smaller anion I^-, the polyelectrolyte showed low conductivity due to weak interactions between the cation and anion. The efficiency of the ssDSC reached 5.6% after the conductivity was immensely improved (6.41×10^{-3} S cm^{-1}) by incorporation of I_2 and *N*-alkylpyridine iodide (NR'PI).[212,218]

Li *et al.* introduced functionalized hydroxyethyl and ester co-functionalized imidazolium iodide (HEII) as a solid-state electrolyte and investigated the effect of substituents to the imidazolium ring on the ionic conductivity and the performance of ssDSCs. Compared to the methyl–ethyl-substituted imidazolium iodide, replacement of the methyl group with an ester group increased the ionic conductivity and the cell performance. Replacement of the ethyl group with a hydroxyethyl group further increased the ionic conductivity and cell performance significantly and the ssDSCs achieved a conversion efficiency of 7.45%.[213]

Bella *et al.* contributed to green chemistry by employing biodegradable polymers derived from seaweed as a SPE. The ssDSCs with carboxymethyl-κ-caraageenan (CκC) and NaI/I_2 demonstrated a high power conversion efficiency of up to 2.06% with an ionic conductivity value of 5.53×10^{-2} S cm^{-1} at room temperature. The system displayed high degree of stability and even after 250 h under thermal stress (60 °C) for stability test, the cell showed only a 6% reduction of its initial photoconversion efficiency.[214]

Limitations associated with SPEs are still related to poor pore filling and ionic conduction resulting in a low dye regeneration rate and high electron recombination kinetics occurring in the solid polymer electrolyte and interfaces with dye and the metal oxide semiconductor. High wettability of sensitized TiO_2 films is also an important factor for dye regeneration, which is attributed to a 0.2 eV decrease in the highest occupied molecular orbital energy of the dye yielding an increase in the driving force for dye regeneration. This understanding may contribute to a further increase in the energy-conversion efficiency of DSCs employing solid polymer electrolytes.

3.2.1.2. Quasi-solid-state electrolytes. Gel polymer electrolytes (GPEs) used as charge transport materials provide a viable and safe alternative to liquid electrolytes. They consist of a liquid electrolyte encapsulated in a polymer framework. These quasi-solid electrolytes combine the properties of a solid and a liquid. When combined, they suppress the leakage of volatile organic solvents, and have excellent pore filling properties. Despite the polymer being present for gelation, GPEs can hold large amounts of the electrolyte (tens to hundreds of times that of the polymer itself). Their excellent contacting and filling properties between the electrodes result in fast dye regeneration, while their high conductivity ensures fast charge transport to the counter electrode. Combined with their low vapor pressure as well as excellent thermal and long-term stability, they even provide the possibility for flexible and therefore wearable electronics.[24,26,77,219–222]

Common host materials are polyacrylonitrile (PAN), PEO derivatives and conducting polymers that include polypyrrole (PPy), PAni and other polymers. As organic plasticizers, dimethyl carbonate (DMC), propylene carbonate (PC) and ethylene carbonate (EC) can be used with a wide range of polar solvents, ionic liquids (ILs), and salts.[223,224]

Other categories of GPEs are prepared by swelling the polymeric membrane in the liquid electrolyte with a redox mediator-based electrolyte solution as illustrated. By this method, the liquid electrolyte is trapped in the polymer matrix network and a stable gel is obtained.[225–227]

Bella *et al.* conducted studies on UV-curing GPEs for quasi-solid dye-sensitized solar cells (Fig. 21).

Power conversion efficiencies of up to 4.41% (Table 5) were reported using bisphenol-A-ethoxylate dimethacrylate (BEMA) and poly(ethylene glycol)methyl ether methacrylate (PEGMA). BEMA forms a three-dimensional network and the addition of PEGMA as a copolymer influences the propagation reaction and changes the architecture of the polymeric matrix, thus affecting its properties.[228–230]

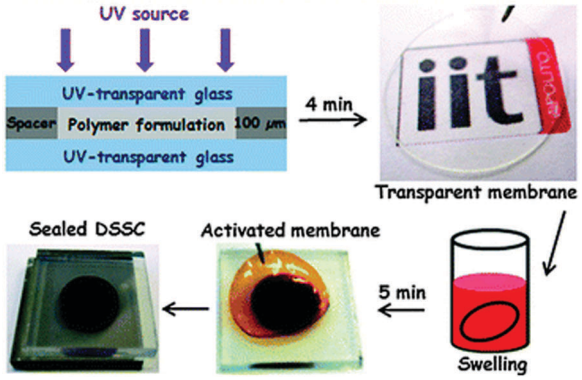

Fig. 21 Preparation of quasi-solid polymer electrolytes by swelling techniques. Reproduced from ref. 227 with permission from the Royal Society of Chemistry.

Table 5 Photovoltaic performance of quasi-solid state polymer electrolytes in ssDSCs

Matrix	Salt	Dye	V_{OC}[a] (mV)	J_{SC}[b] (mA cm^{-2})	FF[c]	PCE[d] (%)	Ref.
PEGMA:BEMA	NaI/I_2	**N719**	499	17.5	0.52	4.4	229
Mg–MOF	NaI/I_2	**N719**	690	12.6	0.55	4.8	231
BEMA:PEGMA:MFC	NaI/I_2	**N719**	760	15.2	0.61	7.0	232
PMMA	BMII/I_2	**N719**	750	15.5	0.69	8.0	233
Polyurethane	LiI/I_2	**N719**	740	15.0	0.55	6.1	234
Polystyrene beads	BMII/I_2	**N719**	770	15.3	0.64	7.5	235

[a] Open circuit voltage. [b] Short circuit current. [c] Fill factor. [d] Power conversion efficiency.

PEGMA was copolymerized with various bifunctional acrylate monomers which formed a three-dimensional polymer network under irradiation. The efficiency of quasi-solid DSCs ranged from 1.3% to 2.7% and was affected by the cross-link density of the membranes due to the amount of liquid electrolyte being trapped in the gel-polymer membranes. A high degree of cross-link density cannot store fair amounts of liquid electrolytes, while a low degree of cross-link density value cannot effectively trap the liquid electrolyte.

Later, a PCE of up to 4.80% was achieved by the introduction of metal–organic framework compounds (Mg–MOF) as fillers. A drastic improvement of PCE (up to 7.03%) was observed after incorporating bio-polymer organic fillers based on microfibrillated cellulose (MFC) into a 30 : 70 BEMA : PEGMA system.[229–232,236,237]

Another component for bioderived photoanodes and polymer electrodes in DSCs can be natural cellulose fibres. Simple papermaking processes using TiO_2-laden paper foils can be applied to (conductive glass or plastic) substrates as alternatives for low temperature applications. The nanoscale microfibrillated cellulose is used as a reinforcing filler in acrylate/methacrylate-based thermo-set polymer electrolyte membranes prepared by UV-induced free-radical photopolymerization. PCEs between 3.55% and 5.20% were achieved for laboratory-scale DSCs.[214]

A PCE of 8.03% was achieved by using GPE based on poly(methyl methacrylate) (PMMA). The ionic conductivity and diffusivity of the iodine/1-butyl-3-methylimidazolium iodide (BMII) redox system were comparable to those of liquid electrolytes, and the resulting cells showed improved stability compared to traditional liquid DSCs.[233] PCEs of 6.1% were achieved by using gel electrolytes based on polyurethane as the polymer matrix prepared through UV curing of a liquid electrolyte containing an aliphatic urethane acrylate.[234] PCEs of 7.54% were reported for devices filled with a liquid electrolyte and controlled dissolution of polystyrene nanobeads on the CE, resulting in a gel electrolyte. The PCE of these devices is comparable to that of liquid-based DSCs (7.59%).[235]

3.2.2. Hole transporting materials. All charge transport materials reviewed so far, albeit solid, work on the same principles of a liquid electrolyte: they mostly rely on ion diffusion to move charges between the dye and the counter electrode. We cannot expect ion diffusion to be as fast in the solid state as it is in a liquid medium. Therefore, we cannot expect solid electrolyte-based DSCs to be as efficient as their liquid counterparts. To achieve high efficiency in ssDSCs, a different paradigm for hole transport is required. Hole transporting materials (HTMs) are homogeneous solid-state hole transporters, *i.e.* charges move within the material itself, rather than through salts embedded in the compound's matrix. Unlike PEs and quasi-solid gels, in HTMs holes move across the layer through inter-molecular hopping processes, rather than relying on ion diffusion.[238,239] In this case, it is more correct to talk about electronic (or charge) diffusion. Since there is no molecular movement involved through a solid medium during charge transport, ssDSCs relying on an HTM layer have the potential to rival liquid DSCs in efficiency, while retaining the benefits of solid-state devices.

Solid-state hole transporting materials introduce a new issue in the fabrication of dye-sensitized solar cells, that is pore filling of the mesoporous oxide layer.[240] This issue can manifest in different forms, depending on the kind of hole transporter employed. In the case of large molecules and macromolecules, such as polymers, their size might prevent them from correctly and fully infiltrating the deepest parts of a thick mesoporous layer.[241,242] Even when a compound is small enough to easily enter into all the pores, the solvent removal problem remains. HTMs are in fact deposited from solution and – to form a solid-state film – the solvent needs to be removed. The hole conductor film will have the best charge transport properties when a compact film can be formed, but the solvent needs channels and voids to escape from the mesoporous layer, eventually creating air bubbles in the HTM film. To overcome (or at least greatly mitigate) this problem, the mesoporous layer of HTM-based ssDSCs is much thinner compared to their liquid counterparts. If a hole conductor has a low melting or glass transition temperature, an alternative procedure to correctly infiltrate the compound is to melt it directly on top of the photoanode, to completely avoid the use of solvents.[243]

Bach *et al.* pioneered work on HTM for ssDSCs in 1998, when they reported for the first time a solid-state device with the hole conductor 2,2′,7,7′-tetrakis(*N*,*N*-di-*p*-methoxyphenylamine)9,9′-spirobifluorene (**spiro-OMeTAD**).[85] That first solar cell had an efficiency of only 0.74%. However, thanks to device

optimization and especially HTM layer optimization with the inclusion of additives and p-dopants to the precursor solution, in 2011 Burschka *et al.*, also from Grätzel's research group, reported on a ssDSC featuring **spiro-OMeTAD** with a PCE of 7.2%.[244] This work renewed research efforts towards efficient hole conductors and became a sort of benchmark for all future works. Both Bach's and Burschka's results, furthermore, contributed to elect **spiro-OMeTAD** as the HTM of reference, against which almost all new compounds are compared. Indeed, **spiro-OMeTAD** has proven to be an efficient hole conductor for solar cells. However, this material presents several drawbacks and there is a consensus on the fact that a new, efficient material will need to be found before ssDSCs become commercially viable. More in detail, **spiro-OMeTAD** suffers from poor conductivity and hole mobility in its pristine form, and it is not stable in the long term.[54,245,246] Furthermore, its synthesis is complex and involves multiple steps, which require time- and energy-consuming purification procedures, making **spiro-OMeTAD** much more expensive than gold.[247]

In the following sections, we will review compounds belonging to several categories which aim to overcome spiro-OMeTAD as the material of choice for ssDSCs together with dopants and additives, which are of paramount importance to achieve high-efficiency devices.

3.2.2.1. Organic hole transporting materials. Most of the compounds investigated as hole transporting materials for ssDSCs belong to the family of organic molecules. Thanks to organic synthesis, in fact, their number, shape, features and properties are only limited by the researcher's creativity. These compounds can be divided into two categories – small molecules and polymers – each with their strengths and weaknesses.

Small molecules enable fine tuning of energy levels, electronic properties, film-forming properties, and solubility in different solvents by combining moieties with different characteristics. Their very well-defined composition and molecular weight allow for great synthetic reproducibility, ensuring consistent properties over different batches. Furthermore, their relatively small size allows them to infiltrate the mesoporous structure of DSCs' photoanode more easily compared to polymers. However, their small size partially hinders inter-molecular charge transfer and they generally suffer from poor charge conductivity, especially in their pristine form.[248,249]

Polymers allow less control over electronic properties and the polymerization steps sometimes limit the chemical composition of the monomer itself.[196] A less than perfect control over the polymerization reaction may prevent good batch-to-batch reproducibility and material properties.[250] Their big size makes it difficult for them to infiltrate the thick mesoporous dye-sensitized layer, forcing researchers to find *in situ* polymerization techniques to overcome this issue. On the other hand, however, their long chains ensure very fast intra-molecular charge movements and their entangled nature in the solid state provides many points of contact for inter-molecular charge hopping. The combination of these two characteristics often grants conductive polymers superior charge transport properties over small molecules.[196]

3.2.2.1.1. Small molecules. The category of organic small molecules is that comprising the highest number of novel HTMs for ssDSCs. Most of the designed compounds share the triphenylamine moiety inside their structure. Triphenylamine is considered a good hole acceptor (electron donor) thanks to the nitrogen's lone electron pair and the presence of three phenyl rings that contribute to the delocalization of the resulting charge, stabilizing the cation. The energy level of molecules containing such a moiety is tuned by adding substituents – most often the electron donating group methoxy – on the phenyls not connected to the rest of the molecule, to destabilize the electronic cloud in the rings.[251] Several of the reviewed hole conductors feature a carbazole as their core moiety, as this group is reported to have good structural and hole transporting properties.[252] A list of reviewed small molecule HTMs together with their associated dye, device parameters and **spiro-OMeTAD** reference cell efficiency is reported in Table 6 while their chemical structures are portrayed in Fig. 22.

Degbia *et al.* and Xu *et al.* both reported on a carbazole featuring a *p*-methoxyphenyl group attached to the nitrogen atom and a di(*p*-methoxyphenyl)amino group in *para* position to each benzene ring, **3b**[253] and **X19**,[254] respectively. Devices with the **3b** HTM were sensitized with the **D102** dye, while those with **X19** employed **LEG4**. This comparison allows understanding how important a good dye–HTM combination is in terms of charge transfer efficiency. The champion device with the **3b** HTM had a V_{OC} of 680 mV, J_{SC} of 6.32 mA cm^{-2}, FF of 0.41 and PCE of 1.75%. The best device with **X19** featured a V_{OC} of 750 mV, J_{SC} of 9.62 mA cm^{-2}, FF of 0.62 and PCE of 4.5%. While a higher current might be due to differences in light absorption profiles between the two dyes, the higher V_{OC} and FF in the latter case is the result of a reduced series resistance (R_s) in the device based on **X19**. Since conductivity and hole mobility of the two HTM layers should be similar as they are based on the same molecule, it can be concluded that a great role in the R_s difference is played by the charge transfer between the dye and the HTM. In their work, Degbia *et al.* also explored the contribution of the *p*-methoxy group to charge transport properties of hole conductors by comparing **3b** with compound **3a**, which lacked the said groups attached to the diphenylamine moieties. The HOMO level of **3a** (−4.95 eV) was slightly lower lying than that of **3b** (−4.84 eV), but still sufficiently high for good dye regeneration. Despite this, the best cell with **3a** had poor parameters, namely a V_{OC} of 860 mV, J_{SC} of 0.32 mA cm^{-2}, FF of 0.44 and PCE of 0.12%. The authors did not perform any conductivity or hole mobility measurement of the two HTMs but, while a different pore filling cannot be excluded, due to the similar molecular structure they argued that the very low current in the case of **3a** was to be attributed to poor charge transport properties caused by the lack of *p*-methoxy groups. In their aforementioned work, Xu *et al.* reported on a second carbazole-based HTM, **X51**.[254] The constituents of **X51** were similar to those of **X19** but in this case two carbazole units were linked together by the two nitrogen atoms through a biphenyl linker, creating a molecule of almost double molecular weight

Table 6 Photovoltaic performance of organic small molecule HTMs in ssDSCs

HTM[a]	Dye	V_{OC}[b] (mV)	J_{SC}[c] (mA cm^{-2})	FF[d]	PCE[e] (%)	PCE with **spiro-OMeTAD**[f] (%)	Ref.
3a	**D102**	860	0.32	0.44	0.12	n.r.[g]	253
3b[h]	**D102**	680	6.32	0.41	1.75	n.r.	253
X19[h]	**LEG4**	750	9.62	0.62	4.5	5.5	254
X51	**LEG4**	920	9.27	0.70	6.0	5.5	254
1[i]	**D102**	800	3.34	0.60	1.62	n.r.	255
2a[i]	**D102**	760	4.41	0.48	1.60	4.44	256
2b	**D102**	750	5.25	0.46	1.81	4.44	256
TCz-C3	**D102**	690	6.27	0.51	2.21	3.03	167
TCz-C6	**D102**	590	0.86	0.38	0.20	3.03	167
TCz-C12	**D102**	660	0.21	0.34	0.05	3.03	167
4b	**D102**	573	0.75	0.28	0.12	n.r.	257
4d	**D102**	630	2.63	0.32	0.54	n.r.	257
5b	**D102**	531	1.72	0.35	0.32	n.r.	257
5	**D102**	850	2.00	0.38	0.63	n.r.	258
H-DATPA	**D102**	620	0.67	0.37	0.15	2.96	259
Me-DATPA	**D102**	700	1.13	0.43	0.34	2.96	259
MeO-DATPA	**D102**	890	1.93	0.67	1.16	2.96	259
MeO-TPD[j]	**LEG4**	800	9.5	0.65	4.9	4.7	117
X1[j]	MKA253	680	5.8	0.58	2.3	6.1	183
	LEG4	720	8.8	0.67	4.3	5.2	183
	LEG4	750	9.47	0.62	4.4	5.4	41
	LEG4	880	9.44	0.69	5.8	5.9	260
X11	MKA253	580	4.7	0.62	1.7	6.1	183
	LEG4	655	8.2	0.55	3.0	5.2	183
X2	**LEG4**	810	9.79	0.63	5.0	5.4	41
X3	**LEG4**	900	9.70	0.66	5.8	5.4	168
	Z907	720	8.10	0.63	3.7	3.5	168
	LEG4	910	9.52	0.67	5.8	5.4	41
X35	**LEG4**	890	9.81	0.63	5.5	5.4	41
X14	**LEG4**	910	9.71	0.71	6.1	5.9	260
HTM	**Z907**	750	8.5	0.51	3.3	n.r.	261
TPAN	$ZnPcOC_4$	720	4	0.42	1.21	n.r.	262
HTM-1	ID504	820	9.34	0.63	4.8	4.8	246
HTM-2	ID504	800	7.08	0.38	2.2	4.8	246
HTM-3	ID504	800	7.00	0.38	2.1	4.8	246
1(Bis)	**D102**	790	3.0	0.51	1.2	n.r.	263
2	**D102**	870	1.8	0.29	0.46	n.r.	263
3	**D102**	810	1.85	0.29	0.44	n.r.	263
X60	**LEG4**	890	11.38	0.72	7.30	n.r.	264
HT2	**LEG4**	920	9.72	0.71	6.35	6.36	247

[a] Hole transporting material. [b] Open circuit voltage. [c] Short circuit current. [d] Fill factor. [e] Power conversion efficiency. [f] Power conversion efficiency of a reference cell fabricated with the spiro-OMeTAD HTM. [g] n.r. = not reported. [h] Same molecule with two different names. [i] Same molecule with two different names. [j] Same molecule with two different names.

compared to **X19**. **X51** and **X19** had similar hole mobilities of 1.51×10^{-4} and 1.19×10^{-4} cm^2 V^{-1} s^{-1}, respectively. However, once prepared with the additives employed in solar cell fabrication, solid-state films of the former displayed conductivities almost one order of magnitude higher compared to the latter. The higher conductivity of **X51** leads to a lower R_s in the final device, as it can be inferred by cell parameters resulting in a V_{OC} of 920 mV, J_{SC} of 9.27 mA cm^{-2}, FF of 0.70 and PCE of 6.0%: while current values were similar, the V_{OC} and FF of the cell based on **X51** were much higher compared to their **X19** counterparts. The higher V_{OC} was not the result of a lower-lying HOMO level of **X51** compared to **X19**, as they were placed only 30 meV apart. The device based on **X51** was also more efficient than the **spiro-OMeTAD**-based reference device, which had a PCE of only 5.5%.

A second comparison can be made between the work of Degbia *et al.* and that of Bui *et al.*, as they both reported devices fabricated with the same dye and hole conductor, named **1**[255] and **2a**,[256] respectively. This compound is similar to **3b** and **X19** but it features an ethyl group attached to the nitrogen of the carbazole instead of a *p*-methoxyphenyl one. Device parameters for HTM **1** were a V_{OC} of 800 mV, J_{SC} of 3.34 mA cm^{-2}, FF of 0.60 and PCE of 1.62% while for **2a** were a V_{OC} of 760 mV, J_{SC} of 4.41 mA cm^{-2}, FF of 0.48 and PCE of 1.60%. The various parameters were quite different for the two cells but they evened out, yielding a similar PCE value. It is interesting to notice that in the case of compound **1** high cell efficiencies were only reached when a final sublimation purification step was performed on the compound, while in the case of **2a** a more common column chromatography final purification step was sufficient. In the same work, Bui *et al.* also reported on a molecule named **2b**, which was similar to **2a** but in which the ethyl group attached to the carbazole's nitrogen was substituted with a hexyl one. This modification was not expected to greatly change electronic properties (their HOMO levels were only 50 meV apart), but rather the film-forming properties and molecular packing in the solid state of the two molecules. Device parameters for a cell based on **2b** were a V_{OC} of

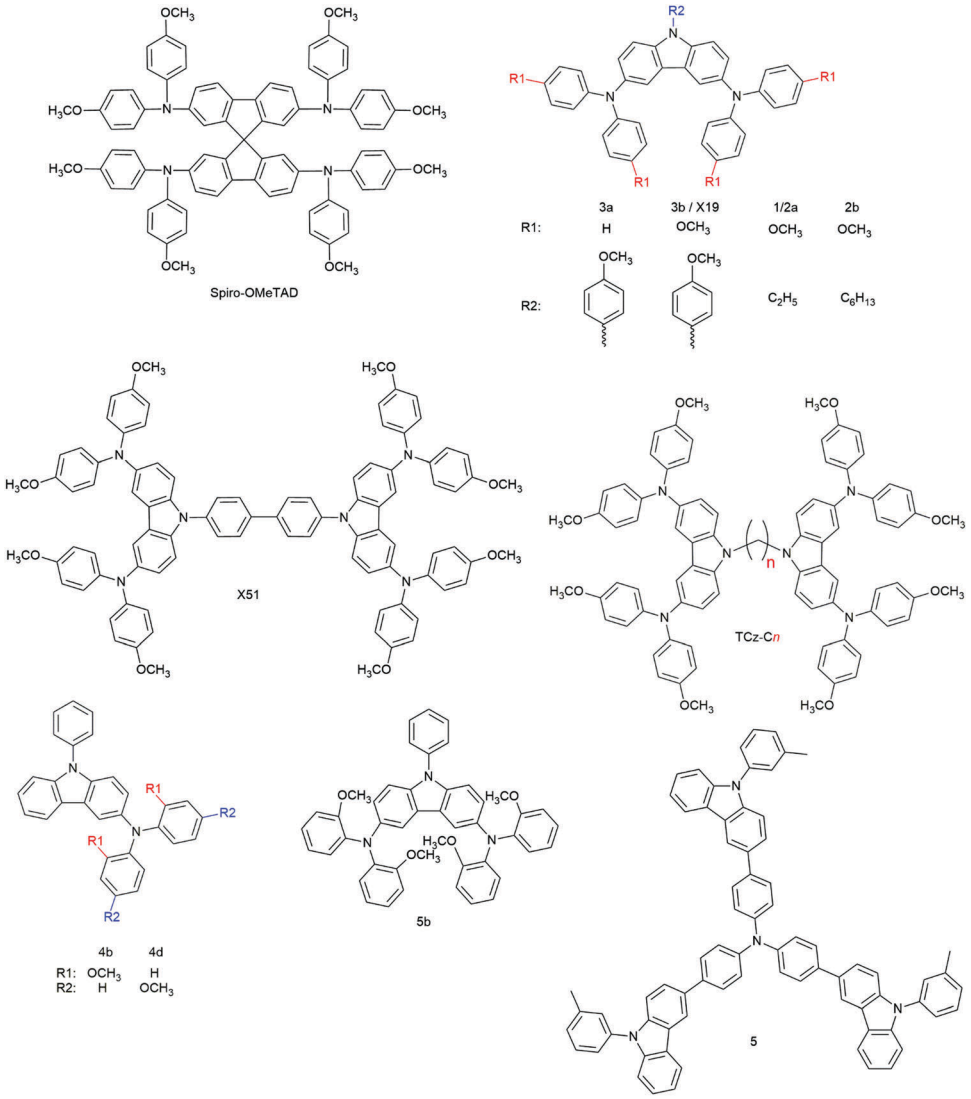

Fig. 22 Spiro-OMeTAD and novel carbazole-based hole transport materials.

750 mV, J_{SC} of 5.25 mA cm^{-2}, FF of 0.46 and PCE of 1.81%. The difference between the two devices was not large, but a higher J_{SC} was obtained with HTM **2b**, leading to a slightly improved efficiency.

Similar to the work done for **X51**, Benhattab *et al.* have connected two carbazole units with alkyl chains, namely propyl (**TCz-C3**), hexyl (**TCz-C6**), and dodecyl (TCz-T12).[167] Unlike **X51**, alkyl chains electronically separated the two carbazole units, which acted as single molecules as far as charge transfer was concerned. The presence of the alkyl linker was instead an attempt to tune the morphology of the solid-state film in the device. The champion device with **TCz-C3** had a V_{OC} of 690 mV, J_{SC} of 6.27 mA cm^{-2}, FF of 0.51 and PCE of 2.21%. The device based on **TCz-C6** had a V_{OC} of 590 mV, J_{SC} of 0.86 mA cm^{-2}, FF of 0.38 and PCE of 0.20%; while that based on **TCz-C12** had a V_{OC} of 660 mV, J_{SC} of 0.21 mA cm^{-2}, FF of 0.34 and PCE of 0.05%. It is clear that the longer the alkyl chain, the worse the performance of the final device, due especially to a plummet in current, a clear sign of charge transport issues. The reason behind this degradation in performance was not clear to the authors, as hole mobilities for the three compounds were similar. They suggested that lower glass transition temperatures for TCz-6 and TCz-12 might cause instability in the HTM layer during device operation. Another reason might be that – since hole mobilities were measured with a planar transistor device – the different environment provided by the DSC mesoporous layer might have affected molecular packing and ultimately the charge hopping capabilities of the studied compounds.

Tomkeviciene *et al.* prepared devices with three different hole transporting materials, **4b**, **4d** and **5b** (see Fig. 22 for their structures).[257] Two of them were asymmetric molecules, with substituted diphenylamino groups attached to only one of the carbazole rings (**4b** and **4d**), while one was symmetric, in which the methoxy groups on the diphenylamino moieties were attached in the *ortho* position, rather than the usual para one. **4b** also featured the two methoxy groups in the *ortho*

position, which created steric hindrance in the molecule, changing the usual geometry of the relevant side groups. All devices fabricated with these compounds achieved modest results. For **4b** the best cell featured a V_{OC} of 573 mV, J_{SC} of 0.75 mA cm^{-2}, FF of 0.28 and PCE of 0.12%. For **4d** the cell parameters were a V_{OC} of 630 mV, J_{SC} of 2.63 mA cm^{-2}, FF of 0.32 and PCE of 0.54%, making it the most efficient of the three. The device based on **5b** laid in between with a V_{OC} of 531 mV, J_{SC} of 1.72 mA cm^{-2}, FF of 0.35 and PCE of 0.32%.

The last carbazole-based HTM – **5** – developed by Lygaitis *et al.* had inverted triphenylamino and carbazole groups: the former was used as the core moiety, and the latter as the side one.[258] The best solar cell built with this compound featured a V_{OC} of 850 mV, J_{SC} of 2.00 mA cm^{-2}, FF of 0.38 and PCE of 0.63%.

Snaith, Robertson and coworkers developed a series of rod-shaped HTMs based on two triphenylamine groups linked by a highly linear diacetylene core, namely **H-DATPA**, **Me-DATPA**, **MeS-DATPA** and **MeO-DATPA** (Fig. 23).[259] The difference between them was given by the different side-groups attached in the *para* position to the two external rings of each triphenylamine moiety. **MeS-DATPA** did not form a uniform film in the device and was therefore discarded, while the other three were analyzed more in detail. As expected, the presence of side groups destabilizes the electronic cloud in the benzene rings, raising the HOMO level, whose values for H-, Me- and **MeO-DATPA** were −5.33, −5.23 and −5.02 eV, respectively. While hole mobility and conductivity values were similar for all compounds, the presence and nature of side groups greatly influenced their performance in ssDSCs, as seen previously for other compounds. All device parameters were improved when going from H to Me and to MeO side groups. The device fabricated with the first one achieved a V_{OC} of 620 mV, J_{SC} of 0.67 mA cm^{-2}, FF of 0.37 and PCE of 0.15%, while for the other two the cell parameters were a V_{OC} of 700 mV, J_{SC} of 1.13 mA cm^{-2}, FF of 0.43 and PCE of 0.34%, and a V_{OC} of 890 mV, J_{SC} of 1.93 mA cm^{-2}, FF of 0.67 and PCE of 1.16%, respectively.

With a molecule named **MeO-TPD**, Johansson and coworkers showed how a light soaking treatment of complete DSC devices can greatly influence the final performance of a solar cell, suggesting that ion migration may occur in the solid-state HTM film.[117] An as-prepared device with **MeO-TPD** attained a V_{OC} of 750 mV, J_{SC} of 2.7 mA cm^{-2}, FF of 0.55 and PCE of 1.1%. However, when performing an initial light soaking treatment of 30 min under open circuit conditions, device performance was boosted to a V_{OC} of 800 mV, J_{SC} of 9.5 mA cm^{-2}, FF of 0.65 and PCE of 4.9%, slightly higher than that of the **spiro-OMeTAD** reference device (4.7%). It is important to notice that the light soaking treatment was only required once, not each time the device was tested. Sun's and Kloo's research groups employed the same molecule – under the name of **X1** – in several other publications[41,183,260] (see Table 6 for all device parameters) with an efficiency of up to 5.8%, the closest to the related spiro-OMeTAD reference device (5.9%). However, in none of these publications the initial light soaking treatment was mentioned.

Yuan *et al.* and Liu *et al.* have worked on similar molecules, namely **HTM**[261] and **X11**,[183] composed of a fluorene core with *p*-methoxydiphenylamino side groups attached to each benzene ring. The hole conductor **HTM**, in addition, also featured long alkyl chains attached to the central fluorene ring with the aim of reducing the glass transition temperature of the compound. Unfortunately, it is not possible to make a direct comparison between the two because their devices employed different dyes and data for a **spiro-OMeTAD** reference cell was not always provided. A ssDSC with **HTM** achieved a V_{OC} of 750 mV, J_{SC} of 8.5 mA cm^{-2}, FF of 0.51 and PCE of 3.3% when both the HTM solution and the substrate were pre-heated before spin-coating. The pre-heating of both solution and substrate was very important for hole conductor deposition as devices only attained an efficiency of 2.0% when just the HTM solution was heated and of 0.44% when neither the solution nor the substrate was heated. A solar cell fabricated with **X11** and the MKA253 sensitizer featured a V_{OC} of 580 mV, J_{SC} of 4.7 mA cm^{-2}, FF of 0.62 and PCE of 1.7%, and a V_{OC} of 655 mV, J_{SC} of 8.2 mA cm^{-2}, FF of 0.55 and PCE of 3.0% when the **LEG4** sensitizer was used instead.

Building on **X1**, Sun and coworkers synthesized a series of *p*-methoxy substituted triphenylamine oligomers.[41] If **X1** was composed of two triphenylamine groups linked linearly, with X2 and X3 the number of repeating units was extended to three and four, respectively. **X35** also featured four units, but rather than being linked linearly they were connected in a star-shaped configuration, with three groups attached to a central one. Optimized devices showed that there was an increase in performance with increasing number of repeating units. Device parameters for an average of 8 cells for each compound were provided (see Table 6 for champion device details) and were as follows: for **X1**-based cells V_{OC} was 725 mV, J_{SC} was 9.26 mA cm^{-2}, FF was 0.56 and PCE was 4.0%; for X2-based cells V_{OC} was 800 mV, J_{SC} was 9.51 mA cm^{-2}, FF was 0.60 and PCE was 4.7%; for X3-based devices V_{OC} was 880 mV, J_{SC} was 9.23 mA cm^{-2}, FF was 0.62 and PCE was 5.4%; for **X35**-based devices V_{OC} was 875 mV, J_{SC} was 9.62 mA cm^{-2}, FF was 0.61 and PCE was 5.2%; lastly, **spiro-OMeTAD**-based reference cells had a V_{OC} of 905 mV, J_{SC} of 9.13 mA cm^{-2}, FF of 0.58 and PCE of 5.2%. Both X3 and **X35** had performances similar or slightly superior to **spiro-OMeTAD**, making them affordable candidates for a broader use. X3 was already reported by Sun's research group in a previous work with very similar performances, showing the good reproducibility of devices made with this compound (see Table 6).[168]

From Sun, Kloo and coworkers came another efficient hole conductor, **X14**.[260] This molecule was also designed to improve on the **X1** HTM and it featured an extended aromatic conjugation, since each of **X1**'s methoxy groups was replaced with an *o*,*p*-dimethoxy substituted phenyl group. This substitution shifted the HOMO level by about 200 meV away from vacuum and gave **X14** a hole mobility that was double that of **X1** when both compounds were doped with LiTFSI. Solar cell performances were similar for the two hole transporting materials, with a small advantage in the case of **X14**. The best device fabricated with **X1** had a V_{OC} of 880 mV, J_{SC} of 9.44 mA cm^{-2}, FF of 0.69 and PCE of 5.8%; while that fabricated with **X14** had a V_{OC} of 910 mV, J_{SC}

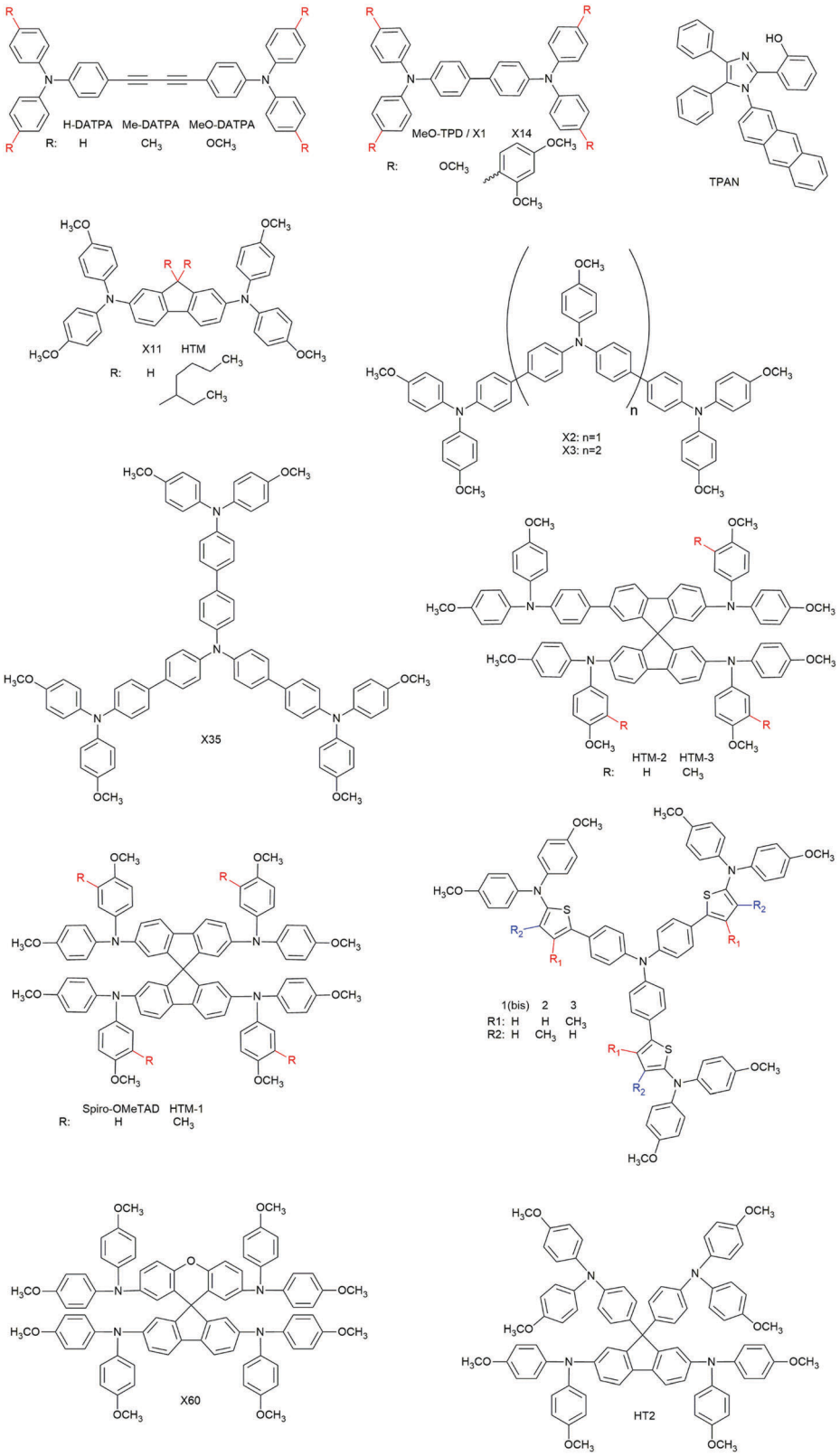

Fig. 23 Triphenylamine-based novel organic hole transport materials.

of 9.71 mA cm^{-2}, FF of 0.71 and PCE of 6.1%. For comparison, the best **spiro-OMeTAD**-based device had a PCE of 5.9%.

Aulakh *et al.* have developed a relatively flat compound based on the linkage of a benzimidazole and an anthracene group.[262]

A solar cell fabricated with a Zn porphyrin dye achieved a V_{OC} of 720 mV, J_{SC} of 4 mA cm^{-2}, FF of 0.42 and PCE of 1.21%.

Malinauskas *et al.* have focused their work on the long-term stability of ssDSCs based on **spiro-OMeTAD**. They discovered that when keeping devices at 60 °C for an extended amount of time, crystalline domains were formed in the initially amorphous **spiro-OMeTAD** film and they proved that this was a major reason for the poor performance of such devices over time (see Section 4.1 on long-term stability).[246] To overcome this issue, they modified **spiro-OMeTAD**'s molecular structure by introducing elements of asymmetry in order to prevent crystallization. In HTM-1 a methyl group was added in the meta position to only one of the two rings of each of the four diphenylamine side groups. HTM-2 and HTM-3 had more radical substitutions, as one of the diphenylamine group was exchanged with a triphenylamine one. HTM-3 also featured the same methyl groups of HTM-1. A batch of five solar cells featuring HTM-1 managed to retain the same average efficiency of the **spiro-OMeTAD** reference one, with a V_{OC} of 820 mV, J_{SC} of 9.34 mA cm^{-2}, FF of 0.63 and PCE of 4.8%. The more heavily substituted HTM-2 and HTM-3 proved less efficient with a V_{OC} of 800 mV, J_{SC} of 7.08 mA cm^{-2}, FF of 0.38 and PCE of 2.2%; and a V_{OC} of 800 mV, J_{SC} of 7.00 mA cm^{-2}, FF of 0.38 and PCE of 2.1%; respectively. More importantly, however, all three HTMs greatly outperformed **spiro-OMeTAD**-based devices in a long-term stress-test at 60 °C.

Hirsch, Goubard and coworkers synthesized three star-shaped hole transporters based on a triphenylamine core and diphenylamine side groups linked to the core *via* a thiophene bridge.[263] The difference between 1 (called 1(bis) throughout this review to avoid confusion), 2 and 3 was that 2 and 3 had a methyl substitution on each thiophene bridge, on the inner or outer available carbon, respectively. Methyl substitutions in 2 and 3 appeared to be detrimental as the device with 1(bis) achieved a V_{OC} of 790 mV, J_{SC} of 3.0 mA cm^{-2}, FF of 0.51 and PCE of 1.2%; while those based on 2 and 3 only achieved a V_{OC} of 870 mV, J_{SC} of 1.8 mA cm^{-2}, FF of 0.29 and PCE of 0.46%; and a V_{OC} of 810 mV, J_{SC} of 1.85 mA cm^{-2}, FF of 0.29 and PCE of 0.44%; respectively, indicating charge transport issues.

Xu *et al.* have synthesized the highest-performing organic hole conductor among those reviewed,[264] and the only one capable of producing a ssDSC able to rival with Burschka's benchmark device.[244] **X60** is based on a spiro[fluorene-9,9′-xanthene] core with *p*-methoxy substituted diphenylamine side groups and its core moiety was estimated to be 30 times less expensive than that of **spiro-OMeTAD**. A **spiro-OMeTAD**-based reference cell was not provided in their work but that based on **X60** featured a V_{OC} of 890 mV, J_{SC} of 11.38 mA cm^{-2}, FF of 0.72 and PCE of 7.30%.

To conclude this review on small molecule HTMs, Boschloo, Sun and coworkers prepared **HT2**, a compound based on a fluorene core featuring *p*-methoxy substituted diphenylamine side groups attached to its two aromatic rings and two *p*-methoxy substituted triphenylamine groups attached to its central ring.[247] Their best device attained a V_{OC} of 920 mV, J_{SC} of 9.72 mA cm^{-2}, FF of 0.71 and PCE of 6.35%, only slightly lower than the **spiro-OMeTAD**-based reference one (6.36%).

3.2.2.1.2. Polymers. The use of polymers in ssDSCs adds a level of complexity compared to small molecules. In fact, it is not enough to develop a highly performing compound, it is also necessary to engineer device fabrication to ensure that the polymer will penetrate the TiO_2 mesoporous structure and thus regenerate the dye throughout the whole device thickness (pore filling will be discussed in greater detail in a following section). Since infiltration of large molecules is challenging, most of the studied polymers are capable of *in situ* polymerization. Thanks to this processing, monomers can wet the device as easily as other small molecules and – after polymerization – the generally higher conductivity of macromolecules can be exploited. For this reason, in each work of this kind there is as much attention on the polymerization process as there is on the nature and properties of the monomer itself. A summary of the champion devices reviewed in this section is presented in Table 7, while Fig. 24 contains the structure of the related units.

Kim and coworkers proposed a polymer based on a propylenedioxythiophene monomer, ProDOT.[265] The corresponding polymer, **PProDOT**, is similar to the more widely known poly(ethylenedioxythiophene) (PEDOT), but its monomer features a propyl alkyl chain rather than an ethyl one. They used a solid-state polymerization technique, starting with a dibrominated ProDOT monomer, to fabricate devices. This technique is very slow but also very simple. A monomer solution was drop-cast onto the photoanode. After solvent evaporation, the solid monomer was left in an oven at 25 °C for five days to allow for polymerization to spontaneously occur with evaporation of Br_2 gas as a side-product. After covering this assembly with a Pt-coated FTO counter-electrode, a V_{OC} of 630 mV, J_{SC} of 10.0 mA cm^{-2}, FF of 0.56 and PCE of 3.5% were achieved in the complete device.

Zhang *et al.* showed the performance of **PEDOP** (poly(ethylenedioxypyrrole)) in combination with three different dyes, demonstrating that the dye plays a crucial role in the suppression of electron recombination.[200] Photoelectrochemical polymerization

Table 7 Photovoltaic performance of organic and inorganic polymeric HTMs in ssDSCs

HTM[a]	Dye	V_{OC}[b] (mV)	J_{SC}[c] (mA cm^{-2})	FF[d]	PCE[e] (%)	Ref.
PProDOT	**N719**	630	10.0	0.56	3.5	265
PEDOP	**D35**	825	7.99	0.66	4.34	200
	D21 L6	645	7.92	0.59	3.05	200
	Z907	440	1.97	0.53	0.46	200
PEDOT	**LEG4**	910	10.80	0.57	5.6	266
	D35	830	8.19	0.68	4.6	266
	Z907	510	4.49	0.66	1.5	266
	DPP07	770	11.13	0.65	5.54	267
PPP-*b*-P3HT	**CYC-B11**	810	8.81	0.65	4.65	268
$TPDSi_2$	**Z907**	683	4.97	0.60	2.05	269
P3HT	**CYC-B11**	750	7.71	0.61	3.53	268
	N3	628	6.29	0.43	1.70	270
	BzTCA	880	8.22	0.44	3.21	270
	D102	720	11.37	0.58	4.78	271
S:DIB	**LEG4**	750	4.11	0.48	1.5	84
	LEG4	700	4.34	0.36	1.09	272
SeS_2:S.DIB	**LEG4**	750	5.04	0.45	1.70	272

[a] Hole transporting material. [b] Open circuit voltage. [c] Short circuit current. [d] Fill factor. [e] Power conversion efficiency.

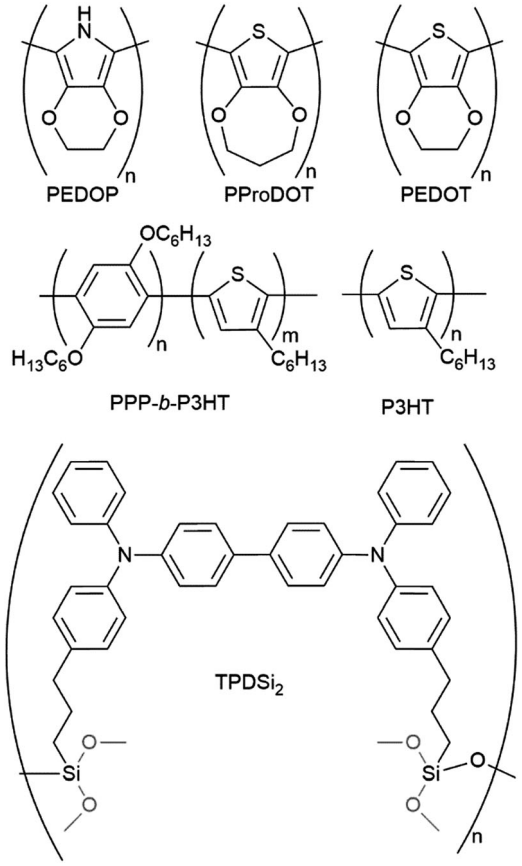

Fig. 24 Polymer hole transport materials.

(PEP) was used for the *in situ* polymerization of EDOP. In this technique, the DSC photoanode is immersed in a solution of the HTM monomer to act as the working electrode in a three-electrode setup. When a current at a suitable potential is run through the device and light is shined on the photoanode, the hole in the HOMO orbital of the excited dye triggers the polymerization of the HTM. With this technique it is possible to achieve electropolymerization of organic compounds at much lower potentials compared to the system where a dye is not present. For this technique to work efficiently, a large enough potential difference between the HOMO of the dye and that of the monomer is required. Device performances were quite different depending on the employed dye, demonstrating once more the importance of a good dye–HTM pairing. The device with the **D35** dye was the best-performing one, with a V_{OC} of 825 mV, J_{SC} of 7.99 mA cm^{-2}, FF of 0.66 and PCE of 4.34%. The other organic dye, **D21 L6**, was slightly less performing with a V_{OC} of 645 mV, J_{SC} of 7.92 mA cm^{-2}, FF of 0.59 and PCE of 3.05%; while the Ru-based dye proved to be poorly compatible with **PEDOP** yielding a device with a V_{OC} of 440 mV, J_{SC} of 1.97 mA cm^{-2}, FF of 0.53 and PCE of 0.46%.

Zhang *et al.* applied the same PEP technique used for **PEDOP** to **PEDOT** as well, again testing the studied polymer in combination with three different dyes.[266] Contrary to **PEDOP**, which was polymerized from EDOP, **PEDOT** was polymerized using a bisEDOT dimer, which had a lower redox potential compared to the EDOT monomer. PEP was performed with all three dyes both in organic and aqueous HTM solutions and in all cases the organic solvent proved to be a better medium for polymerization due to changes in redox potentials of both dyes and HTM precursor. The device based on the **D35** dye with the **PEDOT** hole transporting material was slightly more efficient than that employing **PEDOP**, with a V_{OC} of 830 mV, J_{SC} of 8.19 mA cm^{-2}, FF of 0.68 and PCE of 4.6%. **LEG4** proved to be the best-performing dye, with a V_{OC} of 910 mV, J_{SC} of 10.80 mA cm^{-2}, FF of 0.57 and PCE of 5.6%. **Z907** proved to be more compatible with **PEDOT** than with **PEDOP**, as a solar cell with the former reached a V_{OC} of 510 mV, J_{SC} of 4.49 mA cm^{-2}, FF of 0.66 and PCE of 1.5%. Two years later Zhang *et al.* also showed that the dye DPP07 is as efficient in combination with **PEDOT** as **LEG4**, when they fabricated a device with a V_{OC} of 770 mV, J_{SC} of 11.13 mA cm^{-2}, FF of 0.65 and PCE of 5.54%.[267] This device was much more efficient than a reference one based on **spiro-OMeTAD** (2.91%).

Wang and coworkers explored the properties of a pre-polymerized block copolymer of poly(2,5-dihexyloxy-*p*-phenylene), PPP and poly(3-hexylthiophene), **P3HT**.[268] The PPP block helped the **PPP-*b*-P3HT** copolymer to self-organize in crystalline domains, which increased the hole mobility of the copolymer significantly (8.5×10^{-4} cm^2 V^{-1} s^{-1}) compared to the **P3HT** homopolymer (1.9×10^{-4} cm^2 V^{-1} s^{-1}) and, as the authors claimed, provided a more intimate contact with the **CYC-B11** dye. The pore filling proved to be similar for both copolymer and **P3HT** but, thanks to the higher hole mobility and better contact with the dye, the **PPP-*b*-P3TH**-based solar cell achieved a V_{OC} of 810 mV, J_{SC} of 8.81 mA cm^{-2}, FF of 0.65 and PCE of 4.65%; while those employing **P3HT** could only display a V_{OC} of 750 mV, J_{SC} of 7.71 mA cm^{-2}, FF of 0.61 and PCE of 3.53%.

Zhou *et al.* relied on silanes for *in situ* polymerization of their hole conductor.[269] The $TPDSi_2$ monomer was composed of two triphenylamine groups linked together. In the *para* position to one of the phenyl rings of each group was attached a propyl chain terminated with a silane. The monomer, deposited on the substrate in an inert, glovebox atmosphere, easily infiltrated the titania mesoporous layer. Once exposed to air, the monomer's silane terminations readily underwent cross-linking, creating a rigid and thermally stable structure. It should be noted that, unlike the other reviewed polymers, the backbone of $TPDSi_2$ is not conductive due to the alkyl chains. ssDSCs fabricated with this new HTM featured a V_{OC} of 683 mV, J_{SC} of 4.97 mA cm^{-2}, FF of 0.60 and PCE of 2.05%.

Liu *et al.* probed the performance of **P3HT** with two different dyes.[270] Solar cells attained a V_{OC} of 628 mV, J_{SC} of 6.29 mA cm^{-2}, FF of 0.43 and PCE of 1.70% when sensitized with **N3** and a V_{OC} of 880 mV, J_{SC} of 8.22 mA cm^{-2}, FF of 0.44 and PCE of 3.21% when sensitized with **BzTCA**, once more proving that organic dyes are better-suited to work with polymeric HTMs. The best **P3HT**-based ssDSCs were fabricated by Clément and coworkers.[271] They overcame the typical pore filling issues of **P3HT** by synthetizing a highly regioregular polymer with medium-range molecular weight and narrow dispersity. **P3HT** with such characteristics achieved high efficiency in a device with a 2 μm thick titania layer. After HTM deposition and an

annealing step at 150 °C to improve film morphology, devices displayed a V_{OC} of 720 mV, J_{SC} of 11.37 mA cm^{-2}, FF of 0.58 and PCE of 4.78%. For comparison, a device fabricated with **spiro-OMeTAD** displayed a PCE of only 3.99%.

The last two reviewed polymeric HTMs, developed by Liu, Gardner and Kloo, sit at the border between organic polymer and inorganic hole transporting materials. These two compounds are, in fact, composed of inorganic polymers (either sulfur in the case of S:DIB[84] or a mix of sulfur and selenium sulfide in the case of SeS_2:S:DIB[272]) cross-linked with the organic molecule 1,3-diisopropenylbenzene in a process called inverse vulcanization. Both polymers were soluble in organic solvents and, hence, solution-processable. The best solar cell fabricated with S:DIB displayed a V_{OC} of 750 mV, J_{SC} of 4.11 mA cm^{-2}, FF of 0.48 and PCE of 1.5%. The addition of selenium sulfide increased the performance to a V_{OC} of 750 mV, J_{SC} of 5.04 mA cm^{-2}, FF of 0.45 and PCE of 1.70% (compared to an efficiency of 1.09% of a device with S:DIB fabricated at the same time).

3.2.2.2. Inorganic hole transporting materials. Inorganic semiconducting materials are a class of compounds with great potential for energy conversion and transport. To date, many electronic, solar, and energy storage devices have relied on them for efficient operation.[9] They possess good electronic properties, good conductivity and high temperature stability.[63,80,124] In the field of dye-sensitized solar cells their use is limited, as only a few of them are soluble in solvents and at temperatures compatible with DSC fabrication. Even fewer have good energy alignment with dyes and n-type semiconductors used in this class of solar cells and it is not as easy to tune their energetics as in the case of organic compounds. The few materials that can be used in ssDSCs have better performances than most organic HTMs, although charge recombination at grain boundaries can prove to be an issue. In Table 8 all the inorganic materials that have been recently studied as hole conductors in ssDSCs can be found.

Chung *et al.* employed the tin-based perovskite $CsSnI_3$ as a hole transporting material in an **N719**-sensitized ssDSC.[33] After doping with tin fluoride and engineering the device with ZnO photonic crystals their best solar cell exhibited a V_{OC} of 732 mV, J_{SC} of 19.2 mA cm^{-2}, FF of 0.72 and PCE of 10.2%. From the IPCE the authors showed that the hole conductor contributed to the cell's photocurrent in the region between 550 and 700 nm. Despite the very high efficiency achieved with this material (the highest among the reviewed inorganic HTMs), $CsSnI_3$ suffers from high instability as Sn(II) is not the most stable oxidation state of tin at room temperature in air. Peedikakkandy and Bhargava worked on the same material and their best cell attained 3% efficiency. Furthermore, they reported on the degradation mechanisms of $CsSnI_3$.[273] Their results showed that the material was stable in an inert atmosphere, but when exposed to air and moisture it first underwent a phase transition to a non-conductive, one-dimensional phase and then oxidation to Cs_2SnI_6.

Due to the instability of the Sn(II)-based perovskite, Chang and coworkers decided to use the air stable Cs_2SnI_6 compound as a hole conductor for their cells.[149] This material was used to harvest holes from three differently sensitized photoanodes. The ssDSC sensitized with **Z907** yielded a V_{OC} of 571 mV, J_{SC} of 13.2 mA cm^{-2}, FF of 0.61 and PCE of 4.63%; while that with **N719** a V_{OC} of 631 mV, J_{SC} of 14.7 mA cm^{-2}, FF of 0.68 and PCE of 6.32%. The best performance was achieved with a mix of dyes, namely **N719**, **YD2-o-C8** and RLC5. Such a device had a V_{OC} of 623 mV, J_{SC} of 16.9 mA cm^{-2}, FF of 0.66 and PCE of 6.94%. The performance with the dye mix was further increased after engineering the solar cell with ZnO photonic crystals, reaching a V_{OC} of 618 mV, J_{SC} of 18.6 mA cm^{-2}, FF of 0.68 and PCE of 7.80%. A sample cell with the **Z907** dye proved to be quite stable for 800 h.

Sakamoto *et al.* worked on copper iodide, which is a well-known HTM for solar applications.[274] In their study they focused on the influence that the contact materials have on the performance of the drop-cast CuI layer. Results showed that the presence of thiocyanate groups in both the dye and counter electrode was of paramount importance to achieve high efficiency. The variation of the density of SCN groups in the **PEDOT:PSS** based counter electrode in particular led to devices with an efficiency that was more than double that of the devices without SCN groups. The best ssDSC displayed a V_{OC} of 739 mV, J_{SC} of 14.5 mA cm^{-2}, FF of 0.69 and PCE of 7.4%. Muhamad and Mahmood also fabricated devices with CuI using a mist-atomization technique, with more modest results.[275] Their best device achieved a V_{OC} of 650 mV, J_{SC} of 3.51 mA cm^{-2}, FF of 0.46 and PCE of 1.05%.

The last reviewed inorganic hole conductor is CuSCN, based on the work of Premalal *et al.*[276] They doped CuSCN with triethylamine hydrothiocyanate to improve the p-type conductivity of the inorganic material. The precursor solution required an equilibration time of 20 days before deposition in a ssDSC, after which the device achieved a V_{OC} of 578 mV, J_{SC} of 10.52 mA cm^{-2}, FF of 0.55 and PCE of 3.39%.

Table 8 Photovoltaic performance of inorganic HTMs in ssDSCs

HTM[a]	Dye	V_{OC}[b] (mV)	J_{SC}[c] (mA cm^{-2})	FF[d]	PCE[e] (%)	Ref.
$CsSnI_3$	**N719**	732	19.2	0.72	10.2	33
	N3	620	9	n.r.[f]	3	273
Cs_2SnI_6	**Z907**	571	13.2	0.61	4.63	149
	N719	631	14.7	0.68	6.32	149
	Mix[g]	623	16.9	0.66	6.94	149
	Mix + PC[g]	618	18.6	0.68	7.80	149
CuI	**N3**	739	14.5	0.69	7.4	274
	N3	650	3.51	0.46	1.05	275
CuSCN	**N719**	578	10.52	0.55	3.39	276

[a] Hole transporting material. [b] Open circuit voltage. [c] Short circuit current. [d] Fill factor. [e] Power conversion efficiency. [f] n.r. = not reported. [g] Mix = **N719** + **YD2-o-C8** + RLC5, PC = photonic crystal.

3.2.2.3. Coordination metal complex hole transporting materials. Coordination transition metal complexes are a class of materials that inherits benefits and drawbacks from both organic small molecules and inorganic compounds. They retain the ease of processing of organic compounds but with charge conductivity

closer to the inorganic ones, which eliminates the need for p-dopants. More exactly, the p-dopant is embedded in the compound itself and it consists of the same complex with a higher oxidation state of its metal center. Their energy levels are easily fine-tuned by applying changes to the organic ligand or greatly varied by changing the metal center.[277,278] However, they have the tendency to form crystalline domains in the solid state, either immediately upon deposition or over time.[107,279] This crystallization may modify film morphology, worsening the contact between the dye or counter electrode and HTM, thus hindering charge transport; or it may create charge recombination sites at grain boundaries. Metal complexes have already contributed greatly to the advancement of liquid DSCs by replacing iodine/iodide as the electrolyte as they have simple, one-step oxidation and reduction processes (thus reducing the driving force needed for regeneration) and are much less corrosive than the latter. To date, all most-efficient liquid DSCs are based on transition metal complex electrolytes.[19,104,280] In the field of solid-state dye-sensitized solar cells, however, they have only recently started to be investigated and only a few examples of their application exist. It should be noted, however, that the two best performing ssDSCs employ a metal complex as the hole conductor. Device details of metal complex-based ssDSCs are found in Table 9, while in Fig. 25 there is a graphical representation of the compounds' molecular structures.

Freitag *et al.* were the first researchers to publish a work on solid-state dye-sensitized solar cells based on a metal complex hole conductor. They used a mix of Cu(I) and Cu(II) coordinated with a phenanthroline-based ligand (**Cu(dmp)$_2$**).[107] The device fabrication method was similar to that of liquid devices, but instead of sealing the cell after electrolyte injection the solvent was allowed to evaporate in air and then a new injection was performed until the space between the photoanode and the counter electrode was filled with solid HTM. Their best solar cell achieved a V_{OC} of 1010 mV, J_{SC} of 13.8 mA cm^{-2}, FF of 0.59 and PCE of 8.2%, making it more efficient than the **spiro-OMeTAD**-based reference device (5.6%) and even more efficient than a liquid DSC based on the same electrolyte (6.0%).

Kashif *et al.* published a similar device based on a Co(II/III) metal center and a polypyridyl hexadentate ligand ([**Co(bpyPY4)**](OTf)$_{2.33}$).[281] As inferred by the counter-ion stoichiometry, the Co(II) to Co(III) ratio was 2 : 1. The device fabrication method was similar to that of Freitag *et al.* but in this case the HTM solvent was removed under vacuum rather than by natural evaporation in air. Kashif's best device exhibited a V_{OC} of 768 mV, J_{SC} of 12.12 mA cm^{-2}, FF of 0.62 and PCE of 5.68%. In the same work, Kashif tried to fabricate ssDSCs with the **Co(bpy)$_3$** metal complex, which is known to yield high efficiency in liquid DSCs.[282] However, in the solid state charge transport issues due to poor conductivity severely limited the output current, yielding a device with a V_{OC} of 877 mV, J_{SC} of 0.66 mA cm^{-2}, FF of 0.73 and PCE of 0.21%. This demonstrated that not all metal complexes, not even those with a common metal center, can be employed as hole conductors in ssDSCs.

Table 9 Photovoltaic performance of metal complex HTMs in ssDSCs

HTM[a]	Dye	V_{OC}[b] (mV)	J_{SC}[c] (mA cm^{-2})	FF[d]	PCE[e] (%)	Ref.
Cu(dmp)$_2$	**LEG4**	1010	13.8	0.59	8.2	107
[**Co(bpyPY4)**](OTf)$_{2.33}$	**Y123**	768	12.12	0.62	5.68	281
[**Co(bpy)$_3$**](OTf)$_{2.33}$	**Y123**	877	0.66	0.73	0.21	281
Cu(tmby)$_2$	**Y123**	1080	13.87	0.73	11.0	87
	WS-72	1070	13.8	0.79	11.7	103

[a] Hole transporting material. [b] Open circuit voltage. [c] Short circuit current. [d] Fill factor. [e] Power conversion efficiency.

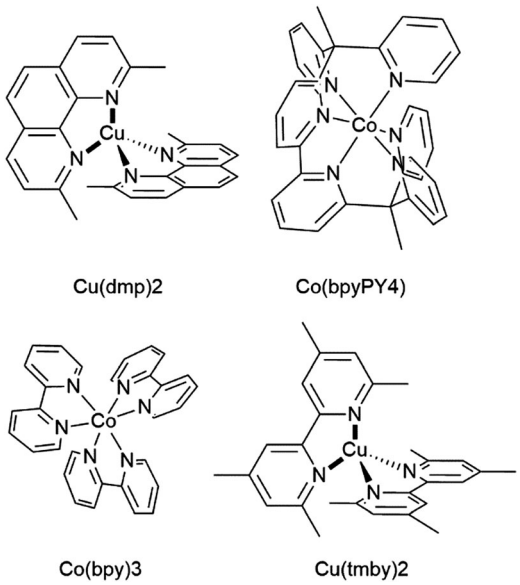

Fig. 25 Transition metal complexes as hole transport materials in ssDSCs.

Building on the work on Cu complexes by Freitag, Grätzel and coworkers have fabricated the highest-performing ssDSCs reported so far, both based on a Cu(I/II) complex with the bipyridine-derived ligand tmby.[87,103] In their first work the authors coupled **Cu(tmby)$_2$** with the **Y123** dye to achieve a best-performing V_{OC} of 1080 mV, J_{SC} of 13.87 mA cm^{-2}, FF of 0.73 and PCE of 11.0%. In their latest work they developed a new dye, **WS-72**, designed to reduce potential loss in the solar cell through better energy alignment of the various device components and reduced electron recombination. Indeed, in liquid DSCs a V_{OC} improvement of 70 mV and a FF improvement of 0.04 were observed when moving from **Y123** to the **WS-72** dye. A solid-state device with **Cu(tmby)$_2$** and **WS-72** was fabricated with a V_{OC} of 1070 mV, J_{SC} of 13.8 mA cm^{-2}, FF of 0.79 and PCE of 11.7%. Although the V_{OC} of this device was slightly lower compared to that of the previous work despite the better dye energy alignment, the improved FF led to a significant increase in efficiency.

3.2.2.4. Dopants for hole transporting materials. When it comes to HTM dopants, some confusion exist in the literature regarding their nomenclature, and it is important to make a distinction between additives and proper dopants (p-dopants). On the one hand, additives are compounds dissolved in the HTM precursor solution because they must be applied to the device after dye sensitization, but they do not directly affect the

Table 10 Electrochemical properties of HTM dopants, conductivity of pristine and doped **spiro-OMeTAD** solid-state films, and efficiency of ssDSCs fabricated with pristine and doped **spiro-OMeTAD** HTM layers

Dopant	Redox potential (V *vs.* NHE)	Pristine conductivity (S cm^{-1})	Doped conductivity (S cm^{-1})	Pristine efficiency (%)	Doped efficiency (%)	Ref.
FK102	1.06	4.4×10^{-5}	5.3×10^{-4}	2.3	5.6	244
				2.6[a]	6.1[a]	244
FK209	1.02[b]	n.r.[c]	n.r.	2.3[d]	6.2	293
FK269	1.28[b]	n.r.	n.r.	2.3[d]	6.0	293
LiTFSI + O_2	n.a.[e]	3×10^{-8}[f]	3×10^{-5}	~0[f]	3	54 and 96
F4TCNQ	4.0[b]	n.r.	n.r.	0.01[f]	0.33[f]	294
				4.55	5.44	294
$SnCl_4$	1.10	~4-Fold increase		2.52	3.40	295
Spiro$(TFSI)_2$	n.a.	2.0×10^{-8}[f]	1.4×10^{-3}[f]	5.71×10^{-4}[f]	4.67[f]	245
				2.34	4.89	245
TeCA	n.r.	1.2×10^{-6}	7.5×10^{-5}	5.8	7.7	296
TEMPO-Br	0.97	7.42×10^{-5}	3.67×10^{-4}	3.99	6.83	297
DDQ	n.r.	5.31×10^{-5}	2.22×10^{-4}	3.50	6.37	298

[a] After 5 days. [b] Assuming a redox potential of $Fc^{0/+}$ *vs.* NHE of 0.7 V or of NHE *vs.* vacuum of 4.4 V.[299] [c] n.r. = not reported. [d] From ref. 244. [e] n.a. = not applicable. [f] Without LiTFSI.

HTM itself. For example, additives like LiTFSI and 4-*tert*-butylpyridine (or other similar substituted pyridines) are known to migrate to the TiO_2 surface to shift energy levels and passivate the exposed surface, in order to enable better charge injection and to reduce charge recombination at the TiO_2–HTM interface.[97,283–288] They are not only used in solid-state devices, but also in liquid DSCs. In the solid state, they may have the additional effect of modifying the HTM film morphology.[289] On the other hand, proper dopants are characteristic of solid-state hole conductors and affect them directly by oxidizing a fraction of the material. The partial oxidation of the hole conducting material leads to the presence of vacancies in the solid-state film, which greatly increase hole mobility across the layer and, ultimately, conductivity.[290] For organic compounds and small molecules in particular, which display very low hole mobility in their pristine state, the use of dopants is of paramount importance for the fabrication of efficient devices (*vide infra*). Compounds with a more positive redox potential with respect to that of the HTM (or strong Lewis acids) act as p-type dopants in HTM layers. Sufficient enough driving force promotes removal of electrons from the hole conductor. All the reviewed dopants have been applied to the **spiro-OMeTAD** molecule due to its role of reference material in ssDSCs but they can also be applied to other hole conductors to increase their conductivity.[264,291,292] A summary of reviewed dopants and their effect on **spiro-OMeTAD**'s hole mobility, and device efficiency is given in Table 10. In Fig. 26 the chemical structures of these compounds are depicted.

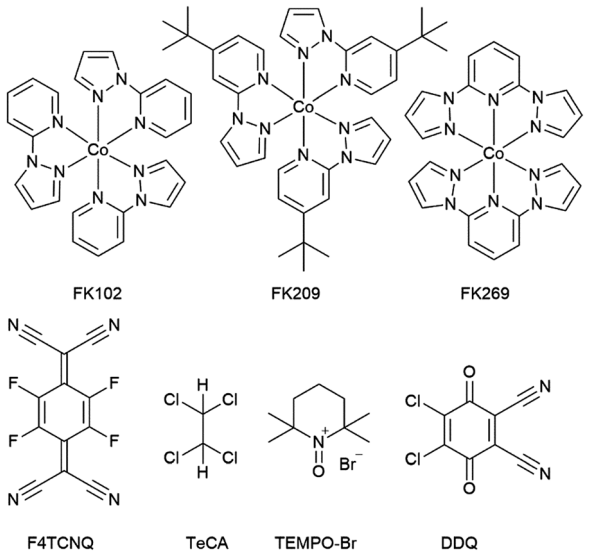

Fig. 26 Dopants tested to enhance the performance of **spiro-OMeTAD** in ssDSCs.

Burschka *et al.* prepared for the first time a p-dopant – **FK102** – which allowed solid-state dye sensitized solar cells to achieve relatively high efficiencies.[244] Furthermore the compound – which was a Co(III)-based metal complex with three pyrazole-pyridine ligands – was soluble in the HTM precursor solution, simplifying the deposition process. The complex was able to oxidize **spiro-OMeTAD** and the resulting Co(II) species had a low molar extinction coefficient, which did not interfere with the effective light absorption of the dye. After doping the HTM film conductivity increased from 4.4×10^{-5} to 5.3×10^{-4} S cm^{-1}, which in turn improved the average device efficiency from 2.3 to 5.6%. A second measurement after five days resulted in an even greater improvement as the reference cells increased their efficiency to 2.6% and those with the doped **spiro-OMeTAD** to 6.1%. Two years later Burschka *et al.* presented two more Co complex p-dopants – FK209 and **FK269** – which were synthesized to improve the poor solubility of **FK102** in relatively nonpolar solvents like chlorobenzene.[293] In both of them PF_6^- counter-ions were replaced with much more soluble $TFSI^-$ ones. Furthermore, FK209 featured a ligand similar to that of **FK102** but in which the pyridine was replaced with 4-*tert*-butylpyridine to increase solubility. **FK269** was designed with a tridentate ligand instead, in which a second pyrazole moiety was added to **FK102**'s ligand. This ligand significantly increased the redox potential of the compound (see Table 10), making it suitable to oxidize HTMs with a lower lying HOMO level than **spiro-OMeTAD**. The increased solubility

allowed the authors to study greater concentrations – up to 5 times higher – of the dopant in the hole conductor solution. Keeping the 2.3% efficient devices of the previous study as a reference, average efficiencies of solar cells with FK209 reached 6.2% with 10% dopant concentration (6.0% with 2% concentration), while devices with 2% concentration of **FK269** also attained efficiencies of 6.0%.

Cappel *et al.* began the study of LiTFSI's p-doping properties when devices were exposed to an air or to a N_2 atmosphere in the presence of light[96] and Snaith and coworkers continued their work giving a full explanation of LiTFSI's doping properties.[54] The combined results of these studies showed that LiTFSI enabled molecular oxygen to oxidize **spiro-OMeTAD** regardless of light exposure, while LiTFSI alone was not able to oxidize the hole conductor. Conductivities after Li-catalyzed doping were increased by three orders of magnitude and the device efficiency increased from nearly 0% to 3%. Unfortunately, this redox reaction in air consumed Li^+ ions due to the formation of lithium oxides, and Li^+ also plays an important role as an additive on the titania surface in DSCs. For this reason, the authors recommended the use of a proper p-dopant for the oxidation of the hole transporter.

Chen *et al.* combined **spiro-OMeTAD** with the Lewis acid 2,3,5,6-tetrafluoro-7,7,8,8-tetracyanoquinodimethane (**F4TCNQ**), a strong electron acceptor.[294] When they added 1.1 wt% dopant to the HTM solution a UV-Vis measurement confirmed the formation of the **spiro-OMeTAD**$^+$ species. They applied pristine and doped hole transporter solutions (without LiTFSI) to ssDSCs obtaining a 3300% increase in efficiency from 0.01 to 0.33%. However, the presence of LiTFSI was required to achieve high efficiency and the two solutions with the added Li salt led to device efficiencies of 4.55 and 5.44%, respectively, confirming the beneficial effect of **F4TCNQ** doping.

Han and coworkers also worked on a Lewis acid, $SnCl_4$.[295] In their report they showed a figure with the *I–V* curves of the conductivity measurements without providing any actual number. From the picture itself, however, a ~4-fold increase in conductivity can be inferred upon $SnCl_4$ doping. When a 0.8% doped solution of **spiro-OMeTAD** was applied to solar cells, an efficiency of 3.40% was obtained as opposed to an efficiency of 2.52% for non-doped devices.

McGehee and coworkers decided to get rid of any p-dopant – which may alter film-formation or charge transfer properties of **spiro-OMeTAD** – from the HTM solution by pre-oxidizing the hole conductor itself.[245] They reacted **spiro-OMeTAD** with two equivalents of AgTFSI to obtain spiro$(TFSI)_2$ and metallic silver. After purifying the compound, they mixed it with the non-oxidized species in a ratio of 12 mol% to obtain an efficient HTM precursor solution. A solid-state film of this mixture displayed five orders of magnitude increase in conductivity, from 2.00×10^{-8} to 1.43×10^{-3} S cm^{-1} – two orders of magnitude higher than what was achieved with Li-induced oxygen doping by Snaith and coworkers. Devices fabricated without LiTFSI (but with *t*BP) showed an enormous increase in efficiency from nearly 0 to 4.67%, a much greater increase compared to the case of **F4TCNQ** or $SnCl_4$ (0.35% efficiency for a $SnCl_4$-doped device without LiTFSI). The doping beneficial effect was pronounced also in the presence of the Li salt, when solar cell efficiencies increased from 2.34 to 4.89% upon doping.

Xu *et al.* reported on 1,1,2,2-tetrachloroethane (**TeCA**), which they defined as a co-solvent, rather than a proper p-dopant.[296] The reason for this is that UV light needed to be shined on the **TeCA**-containing HTM solution for one minute to allow **spiro-OMeTAD** oxidation to take place. Precipitation of AgCl upon addition of $AgNO_3$ to the oxidized **spiro-OMeTAD/TeCA** solution proved that TeCA oxidized the hole conductor by forming a **spiro-OMeTAD**$^+Cl^-$ salt. 4% **TeCA**-doped HTM film conductivity increased from 1.2×10^{-6} to 7.5×10^{-5} S cm^{-1}. Similarly, device efficiencies improved from 5.8 to 7.7%. As a comparison, devices fabricated with FK209 instead of **TeCA** exhibited an efficiency of 6.8%.

Yang *et al.* oxidized **spiro-OMeTAD** with a compound widely used in organic synthesis – TEMPO (or, rather, its bromide salt **TEMPO-Br**).[297] HTM films doped with 2.5% **TEMPO-Br** showed a smaller increase in conductivity compared to other dopants, with values increasing from 7.42×10^{-5} to 3.67×10^{-4} S cm^{-1}. However, the dopant's effect on device efficiency was remarkable with PCEs increased from 3.99 to 6.83%.

The most recent work on p-dopants in ssDSCs was published by Sun and coworkers, who studied the effects on **spiro-OMeTAD** of 2,3-dichloro-5,6-dicyano-1,4-benzoquinone (**DDQ**), another oxidant widely used in organic synthesis.[298] The most notable result of their work is that only a very tiny 0.04% **DDQ** addition to **spiro-OMeTAD** was required to maximize solar cell efficiency. Conductivity of the oxidized HTM film increased from 5.31×10^{-5} to 2.22×10^{-4} S cm^{-1} and the device efficiency was boosted from 3.50 to 6.37%.

3.3. Counter electrode

The choice of counter electrode materials in recent ssDSC literature strongly correlates with the chosen device architecture. Liquid electrolyte-based DSCs were traditionally assembled in a sandwich structure between two glass electrodes. The counter electrode was often platinized to provide good catalytic interfaces for the reduction of the redox electrolyte species.[300] Given that this sandwich design protects the HTM and other active components of the solar cell well, it is still often chosen as a layout for ssDSCs.[301,302] In 2013, electropolymerized poly(3,4-ehtylenedioxythiophene) counter electrodes (Fig. 27) as a low-cost alternative to the scarce platinum were first presented by Ellis *et al.* with lower sheet resistance compared to platinized electrodes.[74] Such organic counter electrodes have since been employed in most, especially Cu-based, ssDSCs.[87,107]

By contrast, in a ssDSC layout where the HTM is spin-coated onto the sensitized TiO_2, metal contacts are commonly evaporated on top of the HTM layer. Such thin layers of noble metals such as Au/Ag not only collect charges from the HTM but reflect unabsorbed photons back into the active part of the cell.[267,303] Silver contacts generally exhibit stronger light reflection at a lower material cost. Gold contacts, however, excel with chemical stability and higher tolerance of minor defects in the HTM layer, while shunt resistances rapidly arise upon Ag penetration into the HTM layer.[304] A picture as well as a cross-sectional electron microscopy

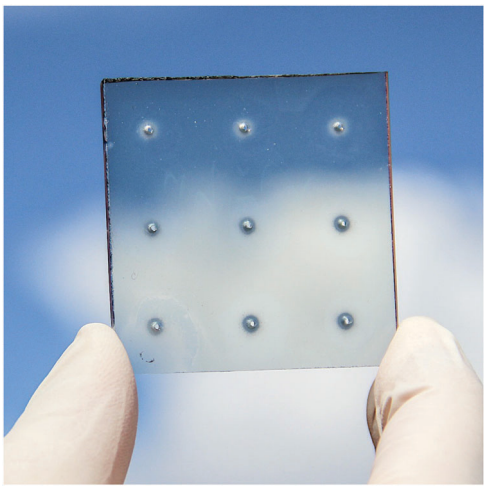

Fig. 27 Electropolymerized poly(3,4-ehtylenedioxythiophene) on an FTO substrate.

image of a ssDSC employing a vacuum-evaporated gold counter contact was shown above in Fig. 1.

Occasionally, alternative approaches for counter electrode deposition are described in the literature. Chiang *et al.* demonstrated in 2012 that a transparent layer of ITO can be sputtered on top of **spiro-OMeTAD** to serve as a counter contact.[305] Such bifacial transparent ssDSCs furthermore open up possible tandem designs (see Section 4.2.2) as later demonstrated by the same group.[306] Aitola *et al.* described the deposition of carbon nanotubes as counter electrode materials in solid-state DSCs. They combined *in situ* photoelectropolymerized poly(3,4-ethylenedioxythiophene) onto mesoporous TiO_2 sensitized with the organic **LEG4** dye and achieved 4.8% power conversion efficiency with subsequently transferred single-walled carbon nanotubes doped with lithium bis(trifluoromethylsulfonyl)imide and 4-*tert*-butylpyridine whilst 5.2% power conversion with an evaporated Ag contact.[307] Zhang *et al.* deposited carbon nanotubes onto a flexible conductive ITO-coated poly(ethylenetherephtalate) substrate and fabricated quasi-solid-state DSCs with 4.24% power conversion efficiency at 0.95 sun illumination, while recording 4.87% efficiency with Pt-based reference devices.[308] Margulis *et al.* sprayed Ag nanowires on top of a poly(3,4-ethylenedioxythiophene): polystyrenesulfonate layer to obtain 3.6% power conversion efficiency and 3.7% for the reference device with evaporated silver contacts.[309]

Early reports indicated that power conversion efficiencies achieved with evaporated gold contacts were matched with pressed graphite.[143] Even gold-coated glass substrates were tested as counter electrodes initially, but no longer pursued due to interfacial issues.[310]

4. Device characteristics

4.1. Stability

Ultimately, any solar cell technology is required to perform over years or even decades of operation to become a feasible investment for customers. To yield any non-negligible return-on-investment (ROI) interest for the investor, the lifetime of any solar cell needs to exceed the payback time for the production cost of the solar cell.[311] However, despite the comparably low production cost of dye-sensitized solar cells, the cells need to, depending on the intended application, sustain a significant period of time to gain market appeal. Therefore, stability testing has become a crucial concern in the development of all emerging photovoltaic technologies.[312,313]

Contrarily to silicon solar cells, no standardized stability testing protocol has been established for DSCs as well as for ssDSCs. Reports can be found in the literature from stability under dark storage conditions to operational stability under full sun illumination, strongly impeding any effective comparison of reported stabilities. Since 2008, the IEC-61646 norm has set the standard testing conditions for common solar cells with temperature cycling between −40 °C and +85 °C combined with performance tracking for 1000 hours.[314] In 2016, new testing protocols were released specifically for testing of, *e.g.*, Si, GaAs, CdTe and other thin film technology solar cells including damp-heat-tests and UV irradiation (IEC-61215-2, IEC-61215-1-2, IEC-61215-1-4).[315] The most common procedure to trace the photovoltaic performance is the so-called maximum power point tracking (MPP).[316]

Although some studies comply with one of the aforementioned standards, milder testing conditions are commonly chosen for stability testing on a laboratory scale. Specifically, the increasing interest in employing DSCs and ssDSCs to power internet of things (IoT) devices under ambient light conditions does not call for equally robust testing procedures.[102]

Solid-state alternatives to liquid electrolyte-based DSCs were developed to circumvent the inherent thermal instability of volatile electrolyte solvents.[317] Electrolytes based on less-volatile solvents such as 3-methoxypropionitrile were demonstrated; however, they suffered from mass transport deficiencies of the redox species in the more viscous electrolyte or aggregation effects at the TiO_2/dye/electrolyte interface.[318,319] Solid-state DSCs are not subjected to such degradation mechanisms in the electrolyte and do thus possess a much higher intrinsic stability compared to their liquid counterparts.

Just as in many biological ensembles, failure of a single component in ssDSCs can lead to malfunction. Generally, with the semiconductor metal oxides exhibiting excellent photo- and thermal stability, degradation pathways largely involve the dye molecules and the hole transporting material (HTM). With the bandgap of 3.2 eV in the widely used antase-TiO_2 comes the absorption of UV-photons in the mesoporous layer of the cell. Consequently, high-energy carriers can lead to destructive, irreversible reactions with both absorbed sensitizers and electrolyte/HTM components.[320] The degradation pathway at the TiO_2/dye/HTM interface, however, has yet to be entirely revealed. While early reports by Kroon *et al.* pointed towards hydrophobic (co-)sensitizers to keep possible water/oxygen away from the TiO_2,[321] later studies indicated that molecules such as 4-*tert*-butylpyridine (or even acetonitrile in the case of liquid-electrolyte DSCs) can passivate reactive states at the TiO_2

surface.[322,323] The variety of ionic dopants (such as Li^+) employed in the most-frequently used **spiro-OMeTAD** has been shown to draw additional humidity into the molecular ensemble.[324]

Different approaches for the geometrical architecture of ssDSCs have been proposed (see Section 2.1). In ssDSCs inspired by the traditional liquid electrolyte 'sandwich' architecture,[107] the active components can be sealed, and will thus not be subjected to (*e.g.* humidity-induced) degradation as easily as ssDSCs with an evaporated counter contact.[200] As already emphasized in the review by Docampo *et al.* in 2014,[325] the reader of any stability report should carefully pay attention to the exclusion of UV-light from the testing protocol as well as the device architecture and sealing.

Several approaches have been reported to address the stability of ssDSCs. Already in 2003, Wang *et al.* observed that gelation of I^-/I_3^- redox electrolytes with poly(vinylideneflouride-*co*-hexaflouropropylene) led to preservation of 94% of the initial performance after 1000 hours of storage at 80 °C, compared to only 88% for the liquid counterpart based on 3-methoxypropionitrile (MPN).[221] In 2007, Zhang *et al.* employed a ruthenium sensitizer and CuI as the HTM to demonstrate that, upon exposure to UV-light, complete device malfunction was observed after 60 hours, while the device produced 90% of its initial power output after 500 hours when employing a 435 nm cutoff UV filter. They furthermore demonstrated that, upon passivation of the TiO_2 surface with a thin layer of MgO, even under UV irradiation 70% of the initial performance was maintained after 72 hours.[326] A first full long-term operational stability study on ssDSCs was carried out by the group of Grätzel and coworkers in 2010. Their devices based on ruthenium sensitizers and **spiro-OMeTAD** as the HTM retained 70% of the initial power output after 1000 hours of continuous full-sun illumination in an inert argon atmosphere employing a thin polyester film to cut off UV-photons below 460 nm.[303] Several approaches ensued to enhance the long-term stability of quasi-solid-state DSCs by gelation of a solvent-based electrolyte and/or ionic liquid with pyrazolium derivates,[327] polyvinylpyrrolidone,[220] poly(1,6-hexanedioldiacrylate),[302] poly(methylmethacrylate) matrices,[328] polyaniline-loaded carbon black,[329] *N*,*N*′-1,5-pentadiylbis-dodecanamide,[330] carboxymethyl-κ-caraageenan[214] and poly(methylmethacrylate)-polyaniline nanotubes.[301]

In 2011, Grätzel and coworkers reported ssDSCs with a new cobalt-based dopant for **spiro-OMeTAD** in C220-sensitized ssDSCs that, employing a 420 nm UV cutoff filter, retained 80% of their initial performance after 40 days under full continuous one-sun illumination at 60 °C.[244] Compelling studies by Malinauskas *et al.* showed that impurities in the **spiro-OMeTAD** layer led to the formation of large crystals, which caused complete device failure after 4 hours at 100 °C. The group instead proposed spiro-derivatives with asymmetric methylation or insertion of phenyl units that impede the crystallization (see Section 3.2.2.1 on organic hole transport materials). Devices based on their methylated **spiro-OMeTAD** analogue matched the photovoltaic performance of pristine spiro-OMeTAD; however, they kept over 90% of the initial power conversion after 1000 hours at 60 °C, while reference devices based on pristine **spiro-OMeTAD** degraded to 10% of their performance. Insertion of phenyl units into **spiro-OMeTAD** also led to an increased long-term stability of at least 50% performance after the same thermal stress treatment.[246] Most recently, the group of Kloo and coworkers designed novel D–A–π–A dyes that allowed for preservation of 86% of the initial performance of devices with doped spiro-OMeTAD as the HTM after 170 hours in a dark ambient atmosphere.[118] In 2017, Cao *et al.* for the first time carried out a long-term stability study on ssDSCs with the performance-leading copper complex hole transport materials. Their devices based on the **Y123** dye and $\mathbf{Cu^{II/I}(tmby)_2}$ showed preservation of 85% power output after 200 hours of continuous illumination with a 50 mW cm^{-2} white LED array.[87]

4.2. Types of ssDSC

The power conversion efficiency of any photovoltaic device is ultimately limited by the intrinsic Shockley–Queisser limit, which was estimated to be around 33.7% in 1961.[114] Briefly, in a single-junction power conversion device, only photons above the bandgap energy of the light absorber can be absorbed. However, for photons of even higher energy, the excess energy with respect to the bandgap of the photoabsorber (sometimes called overpotential) cannot be utilized and is dissipated. In order to obtain a high photovoltage, a large-bandgap material should be chosen. However, high-bandgap solar cells suffer from transmittance losses as many photons below the bandgap energy cannot be converted to photocurrent. Detailed derivations and calculations on the conversion limits of photovoltaic cells were reported by Jacobsson *et al.* as well as Alharbi *et al.* in 2015.[331,332] In order to ultimately overcome the Shockley–Queisser limit, multijunction devices (or their subparts) have recently been investigated for ssDSCs and will be reviewed in the ensuing sections. Additionally, photon-upconversion materials are drawing increasing interest of the scientific community and, while implementation in all-solid-state devices is still awaited, first results on liquid-electrolyte DSCs are reported.[333–336]

4.2.1. p-Type solid-state DSCs. The vast majority of research contributions in ssDSCs (as well as their liquid counterparts) employs the n-type semiconductor titanium dioxide as the photoanode material due to its low material cost, high carrier mobility and moderately good impurity tolerance.[337,338] Occasionally, even sensitized zinc and tin oxides have been reported as photoanodes.[141,339,340] In the development towards heterojunction tandem ssDSCs (see ensuing Section 4.2.2), the sensitization of p-type semiconductors as porous photocathode materials has been investigated. The power conversion mechanism in p-type cells is essentially different from that in n-type ssDSCs and is shown in Fig. 28. A p-type semiconductor (such as NiO) is sensitized with dye molecules that upon photoexcitation inject holes into the semiconductor. An electron-selective material instead of a HTM then completes the dye regeneration.

Sensitized NiO was first studied in I^-/I_3^--electrolyte p-type DSCs by He *et al.* in 1999[341] and more recently by Hammarström and coworkers.[342,343] The group of Tian presented the first all-solid-state p-type cell in 2016. They sensitized mesoporous NiO with the organic P1 dye and used phenyl-C61-butyric acid

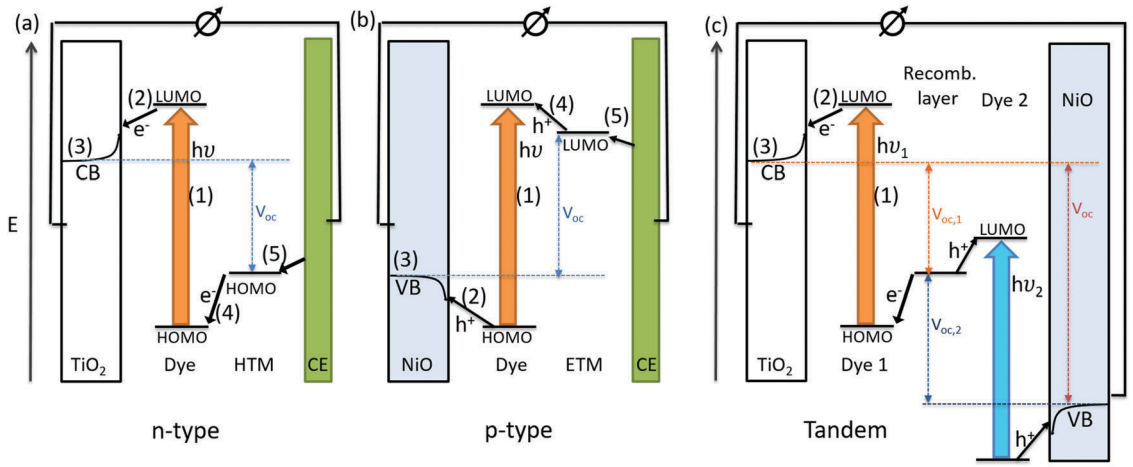

Fig. 28 Charge transfer processes in (a) n-type, (b) p-type and (c) tandem ssDSCs.

methylester (PCBM) as the electron transport material to obtain 620 mV photovoltage, but with only 50 μA cm^{-2} photocurrent density.[344] In 2017, Pham *et al.* sensitized NiO with a diketopyrrolopyrrole dye and measured 0.45 mA cm^{-2} photocurrent density.[152] Tian's group recently demonstrated that the charge separation kinetics can be enhanced by deposition of a shell of titanium dioxide on top of the PB6-sensitized NiO.[345] They furthermore reported that a shielding layer of Al_2O_3 between NiO and TiO_2 suppresses carrier recombination.[346]

4.2.2. Tandem solid-state DSCs. In multi-junction solar cells, several light absorbing sites contribute to the power output of the cell. Through a combination of two variant bandgap materials, the photoresponse of the device can be extended to a broader spectral range and transmittance losses thus minimized. The reader is referred to the works of Jacobsson *et al.* for more general derivations.[331,347] The photoresponse of DSCs can be easily tuned by choice of sensitizers and therefore adjusted for tandem devices. One exemplary cell layout is schematically drawn in Fig. 28. Photoanodes and photocathodes with n-type (such as TiO_2) and p-type semiconductors (such as NiO), respectively, can be sensitized with dyes of different spectral absorption to maximize the light harvesting in the solar cell. The V_{OC} of the cell is then the energetic offset between the Fermi level of electrons in the conduction band of TiO_2 and the Fermi level of holes in the valence band of NiO. Therefore, the theoretical Shockley–Queisser limit can be raised to 42% power conversion efficiency.

In 2000, He *et al.* presented the first tandem-dye-sensitized solar cell.[348] Four years later, both Dürr *et al.* and Kubo *et al.* reported solar cells consisting of two serially positioned, parallel-connected DSCs based on sensitized TiO_2 and I^-/I_3^- electrolyte.[349,350] In 2009, Gibson *et al.* presented heterojunction devices based on a **N719**-sensitized TiO_2 photoanode and a perylene-sensitized NiO photocathode mediated by a single cobalt redox mediator.[351]

Bruder *et al.* reported the first all-solid-state tandem DSC in 2009. A charge recombination layer of Ag was placed between a top cell with indoline-sensitized TiO_2/**spiro-OMeTAD** and a bottom junction of zinc phtalocyanine/C_{60}. With each individual cell component converting sunlight at about 4.0% efficiency, they obtained (serial) tandem cells with 1.36 V open-circuit potential and 6.0% power conversion efficiency.[169] In 2013, Chiang *et al.* used semi-transparent indium-doped tin oxide contacts to stack two n-type ssDSCs. They sensitized the bottom cell with squarine-B1, the top cell with **Z907** and deposited **spiro-OMeTAD** as the HTM on both cells. Upon parallel connection of the cells, they recorded a 3.1% power conversion efficiency, which matched combined conversion of the two subcells.[306]

4.2.3. Light absorption enhancement. Light absorption by components in the redox mediator has shown to impede the photovoltaic performance of liquid-electrolyte DSCs.[352] In particular the photocurrent density suffers from competitive light absorption since the number of photons available for power generation at the dye/TiO_2 junction is reduced. Additionally, reverse transfer of excited charge carriers can inhibit efficient power generation.[352,353] Besides the moderate redox potential, strong competitive light absorption was one of the reasons that led to the development of redox mediator alternatives to iodide/triiodide.[86,354,355]

For solid-state DSCs, however, studies indicate that the addition of photoactive compounds can lead to an increase in, specially, photocurrent density. Electrons excited in the HTM matrix can be transferred to the TiO_2-adsorbed dyes through Förster resonance energy transfer.[356] In 2010, Mor *et al.* demonstrated a light harvesting enhancement for a squaraine-sensitized TiO_2 device upon addition of a pyran dye component to the **spiro-OMeTAD** hole transport material.[357] Unger *et al.* resolved the Förster resonance energy transfer contributions to the incident-photon-to-current conversion efficiency of the photoactive hole transport material tris(thienylvinyl-thienyl)triphenylamine in squaraine-sensitized ssDSCs.[358] Grätzel and coworkers employed the absorbing poly(3-hexylthiophen-2,5-diyl) hole transport material to increase the photocurrent density of a YD2-porphyrine-sensitized ssDSC to 12.1 mA cm^{-2}, however, with potential losses with respect to the **spiro-OMeTAD** device.[359]

5. Outlook

The ignored challenge with all emerging solar cell technologies is that they lack the stability that established technologies have; this is the largest hindrance towards their entrance into society at large. Further, in most of these systems, the development and knowledge curve of the photo-absorbing material has reached a mature state where only incremental improvements are expected for the future. The development of new charge transfer (redox mediators, HTMs, electron transport materials) systems are still far behind the efforts and understanding, which were made to develop new sensitizers or any other component of the DSCs. Large knowledge gaps still exist in the adjacent charge selective and transporting materials. Hence, it is important to address several challenges, including fundamental understanding of how various charge transport materials in solid state facilitate charge transfer and how they can be tuned to obtain ideal energy alignments in the photo-electrochemical device. Simultaneously, the new materials must be stable, easily processable, and prepared from sustainable sources of materials. Careful matching in energy alignments of panchromatic sensitizers, in combination with the new charge transporting materials with higher conductivity and charge mobility, will lead to increased charge collection efficiency and more stable hybrid solar cells.

Conflicts of interest

There are no conflicts to declare.

Acknowledgements

This work was supported by the Swedish Energy Agency (42037-1 and 43294-1), the STandUP for Energy program and the Carl Trygger Stiftelse 17:158.

References

1 A. A. Bartlett, *Am. J. Phys.*, 1978, **46**, 876–888.
2 K. Butti and J. Perlin, *A Golden Thread: 2500 Years of Solar Architecture and Technology*, M. Boyars, 1981.
3 A. Goetzberger, J. Luther and G. Willeke, *Sol. Energy Mater. Sol. Cells*, 2002, **74**, 1–11.
4 A. Cristobal, A. M. Vega and A. L. López, *Next Generation of Photovoltaics: New Concepts*, Springer Berlin Heidelberg, 2012.
5 G. F. Brown and J. Wu, *Laser Photonics Rev.*, 2009, **3**, 394–405.
6 M. A. Green, *Phys. E*, 2002, **14**, 65–70.
7 M. A. Green, Y. Hishikawa, W. Warta, E. D. Dunlop, D. H. Levi, J. Hohl-Ebinger and A. W. H. Ho-Baillie, *Prog. Photovoltaics Res. Appl.*, 2017, **25**, 668–676.
8 A. Becquerel, *C. R. Acad. Sci.*, 1839.
9 S. R. Wenham and M. A. Green, *Prog. Photovoltaics Res. Appl.*, 1996, **4**, 3–33.
10 J. Perlin, *Silicon Solar Cell Turns 50*, USA, 2004.
11 H. Gerischer, *J. Electrochem. Soc.*, 1966, **113**, 1174–1182.
12 H. Gerischer, *Electrochim. Acta*, 1990, **35**, 1677–1699.
13 B. O'Regan and M. Grätzel, *Nature*, 1991, **353**, 737–740.
14 M. Grätzel, *J. Photochem. Photobiol., C*, 2003, **4**, 145–153.
15 A. Hagfeldt, G. Boschloo, L. Sun, L. Kloo and H. Pettersson, *Chem. Rev.*, 2010, **110**, 6595–6663.
16 M. Grätzel, *Chem. Lett.*, 2005, **34**, 8–13.
17 M. Freitag and G. Boschloo, *Curr. Opin. Electrochem.*, 2017, **2**, 111–119.
18 K. Kakiage, Y. Aoyama, T. Yano, K. Oya, J. Fujisawa and M. Hanaya, *Chem. Commun.*, 2015, **51**, 15894–15897.
19 S. Mathew, A. Yella, P. Gao, R. Humphry-Baker, B. F. E. Curchod, N. Ashari-Astani, I. Tavernelli, U. Rothlisberger, Md. K. Nazeeruddin and M. Grätzel, *Nat. Chem.*, 2014, **6**, 242–247.
20 J. Gong, J. Liang and K. Sumathy, *Renewable Sustainable Energy Rev.*, 2012, **16**, 5848–5860.
21 H. Pettersson and T. Gruszecki, *Sol. Energy Mater. Sol. Cells*, 2001, **70**, 203–212.
22 J. Goldstein, I. Yakupov and B. Breen, *Sol. Energy Mater. Sol. Cells*, 2010, **94**, 638–641.
23 A. Hagfeldt and N. Vlachopoulos, in *The Future of Semiconductor Oxides in Next-Generation Solar Cells*, ed. M. B. T.-T. F. of S. O. in N.-G. S. C. Lira-Cantu, Elsevier, 2018, pp. 183–239.
24 M. S. Su'ait, M. Y. A. A. Rahman, A. Ahmad, M. S. Su'ait, M. Y. A. A. Rahman, A. Ahmad, M. S. Su'ait, M. Y. A. A. Rahman and A. Ahmad, *Sol. Energy*, 2015, **115**, 452–470.
25 J.-L. Lan, T.-C. Wei, S.-P. Feng, C.-C. Wan and G. Cao, *J. Phys. Chem. C*, 2012, **116**, 25727–25733.
26 J. Wu, Z. Lan, J. Lin, M. Huang, Y. Huang, L. Fan and G. Luo, *Chem. Rev.*, 2015, **115**, 2136–2173.
27 A. Hauch and A. Georg, *Electrochim. Acta*, 2001, **46**, 3457–3466.
28 M. Freitag, B. Łosiewicz, T. Goryczka and J. Lelątko, *Application of EIS to study the corrosion resistance of passivated NiTi shape memory alloy in simulated body fluid*, 2012, vol. 183.
29 C. Law, O. Moudam, S. Villarroya-Lidon and B. O'Regan, *J. Mater. Chem.*, 2012, **22**, 23387–23394.
30 S. K. Yadav, S. Ravishankar, S. Pescetelli, A. Agresti, F. Fabregat-Santiago and A. Di Carlo, *Phys. Chem. Chem. Phys.*, 2017, **19**, 22546–22554.
31 L. Kavan, P. Liska, S. M. Zakeeruddin and M. Grätzel, *Electrochim. Acta*, 2016, **195**, 34–42.
32 M. Grätzel, *MRS Bull.*, 2005, **30**, 23–27.
33 I. Chung, B. Lee, J. He, R. P. H. Chang and M. G. Kanatzidis, *Nature*, 2012, **485**, 486–489.
34 J.-H. Yum, P. Chen, M. Grätzel and M. K. Nazeeruddin, *ChemSusChem*, 2008, **1**, 699–707.
35 U. Bach, PhD thesis, ÉCOLE POLYTECHNIQUE FÉDÉRALE DE LAUSANNE, 2000.
36 K. Tennakone, G. R. R. A. Kumara, A. R. Kumarasinghe, K. G. U. Wijayantha and P. M. Sirimanne, *Semicond. Sci. Technol.*, 1995, **10**, 1689.
37 K. Tennakone, A. H. Jayatissa, C. A. N. Fernando, S. Wickramanayake, S. Punchihewa, L. K. Weerasena and W. D. R. Premasiri, *Phys. Status Solidi*, 1987, **103**, 491–497.

38 K. Tennakone, G. R. R. A. Kumara, I. R. M. Kottegoda, K. G. U. Wijayantha and V. P. S. Perera, *J. Phys. D: Appl. Phys.*, 1999, **31**, 1492–1496.
39 G. R. R. Kumara, A. Konno, G. K. R. Senadeera, P. V. V. Jayaweera, D. B. R. De Silva and K. Tennakone, *Sol. Energy Mater. Sol. Cells*, 2001, **69**, 195–199.
40 J. Zhang, N. Vlachopoulos, M. Jouini, M. B. Johansson, X. Zhang, M. K. Nazeeruddin, G. Boschloo, E. M. J. Johansson and A. Hagfeldt, *Nano Energy*, 2016, **19**, 455–470.
41 X. Bo, T. Haining, L. Lili, Q. Deping, C. Hong, Z. Jinbao, V. Nick, B. Gerrit, L. Yi, Z. Fengling, H. Anders, S. Licheng, B. Xu, H. Tian, L. Lin, D. Qian, H. Chen, J. Zhang, N. Vlachopoulos, G. Boschloo, Y. Luo, F. Zhang, A. Hagfeldt, L. Sun, X. Bo, T. Haining, L. Lili, Q. Deping, C. Hong, Z. Jinbao, V. Nick, B. Gerrit, L. Yi, Z. Fengling, H. Anders and S. Licheng, *Adv. Energy Mater.*, 2014, **5**, 1401185.
42 D. Moia, U. B. Cappel, T. Leijtens, X. Li, A. M. Telford, H. J. Snaith, B. C. O'Regan, J. Nelson and P. R. F. Barnes, *J. Phys. Chem. C*, 2015, **119**, 18975–18985.
43 I.-K. K. Ding, N. Tétreault, J. Brillet, B. E. Hardin, E. H. Smith, S. J. Rosenthal, F. Sauvage, M. Grätzel and M. D. McGehee, *Adv. Funct. Mater.*, 2009, **19**, 2431–2436.
44 P. Docampo, A. Hey, S. Guldin, R. Gunning, U. Steiner and H. J. Snaith, *Adv. Funct. Mater.*, 2012, **22**, 5010–5019.
45 C. T. Weisspfennig, D. J. Hollman, C. Menelaou, S. D. Stranks, H. J. Joyce, M. B. Johnston, H. J. Snaith and L. M. Herz, *Adv. Funct. Mater.*, 2014, **24**, 668–677.
46 H. J. Snaith, R. Humphry-Baker, P. Chen, I. Cesar, S. M. Zakeeruddin and M. Grätzel, *Nanotechnology*, 2008, **19**, 424003.
47 I. K. Ding, J. Melas-Kyriazi, N. Le Cevey-Ha, K. G. Chittibabu, S. M. Zakeeruddin, M. Grätzel and M. D. McGehee, *Org. Electron.*, 2010, **11**, 1217–1222.
48 C. D. Bailie, E. L. Unger, S. M. Zakeeruddin, M. Grätzel and M. D. McGehee, *Phys. Chem. Chem. Phys.*, 2014, **16**, 4864.
49 A. S. Hoon, K. D. Jun, C. W. Seok and K. J. Hak, *Adv. Funct. Mater.*, 2014, **24**, 5037–5044.
50 W. Cho, J. Lim, T.-Y. Kim, Y. R. Kim, D. Song, T. Park, F. Fabregat-Santiago, J. Bisquert and Y. S. Kang, *J. Phys. Chem. C*, 2016, **120**, 2494–2500.
51 B. E. Hardin, H. J. Snaith and M. D. McGehee, *Nat. Photonics*, 2012, **6**, 162.
52 C. T. Weisspfennig, M. M. Lee, J. Teuscher, P. Docampo, S. D. Stranks, H. J. Joyce, H. Bergmann, I. Bruder, D. V. Kondratuk, M. B. Johnston, H. J. Snaith and L. M. Herz, *J. Phys. Chem. C*, 2013, **117**, 19850–19858.
53 J. Lu, Y. C. Chang, H. Y. Cheng, H. P. Wu, Y. Cheng, M. Wang and E. W. G. Diau, *ChemSusChem*, 2015, **8**, 2529–2536.
54 A. Abate, T. Leijtens, S. Pathak, J. Teuscher, R. Avolio, M. E. Errico, J. Kirkpatrik, J. M. Ball, P. Docampo, I. McPherson and H. J. Snaith, *Phys. Chem. Chem. Phys.*, 2013, **15**, 2572–2579.
55 T. Leijtens, I.-K. Ding, T. Giovenzana, J. T. Bloking, M. D. McGehee and A. Sellinger, *ACS Nano*, 2012, **6**, 1455–1462.
56 M. K. Nazeeruddin, E. Baranoff and M. Grätzel, *Sol. Energy*, 2011, **85**, 1172–1178.
57 T. Higashino and H. Imahori, *Dalton Trans.*, 2015, **44**, 448–463.
58 S. Ito, H. Miura, S. Uchida, M. Takata, K. Sumioka, P. Liska, P. Comte, P. Péchy and M. Grätzel, *Chem. Commun.*, 2008, 5194.
59 S. Gauthier, B. Caro, F. Robin-Le Guen, N. Bhuvanesh, J. A. Gladysz, L. Wojcik, N. Le Poul, A. Planchat, Y. Pellegrin, E. Blart, D. Jacquemin and F. Odobel, *Dalton Trans.*, 2014, **43**, 11233–11242.
60 S. Altobello, R. Argazzi, S. Caramori, C. Contado, S. Da Fré, P. Rubino, C. Choné, G. Larramona and C. A. Bignozzi, *J. Am. Chem. Soc.*, 2005, **127**, 15342–15343.
61 H. L. Wong, C. S. K. Mak, W. K. Chan and A. B. Djurišić, *Appl. Phys. Lett.*, 2007, **90**, 20–22.
62 T. C. B. Harlang, Y. Liu, O. Gordivska, L. A. Fredin, C. S. Ponseca, P. Huang, P. Chábera, K. S. Kjaer, H. Mateos, J. Uhlig, R. Lomoth, R. Wallenberg, S. Styring, P. Persson, V. Sundström and K. Wärnmark, *Nat. Chem.*, 2015, **7**, 883–889.
63 N. Alonso-Vante, J.-F. Nierengarten and J.-P. Sauvage, *J. Chem. Soc., Dalton Trans.*, 1994, **11**, 1649.
64 Z.-S. Wang, Y. Cui, Y. Dan-oh, C. Kasada, A. Shinpo and K. Hara, *J. Phys. Chem. C*, 2008, **112**, 17011–17017.
65 C. Qin, Y. Numata, S. Zhang, X. Yang, A. Islam, K. Zhang, H. Chen and L. Han, *Adv. Funct. Mater.*, 2014, **24**, 3059–3066.
66 E. Stathatos, P. Lianos, A. Laschewsky, O. Ouari and P. Van Cleuvenbergen, *Chem. Mater.*, 2001, **13**, 3888–3892.
67 M. Kraus, S. Richler, A. Opitz, W. Brütting, S. Haas, T. Hasegawa, A. Hinderhofer and F. Schreiber, *J. Appl. Phys.*, 2010, **107**, 3–8.
68 H. J. Snaith and M. Grätzel, *Appl. Phys. Lett.*, 2006, **89**, 262114.
69 J. U. Wallace, *Carrier mobility in organic charge transport materials: methods of measurement, analysis, and modulation*, University of Rochester, 2009.
70 H. J. Snaith and M. Grätzel, *Adv. Mater.*, 2007, **19**, 3643–3647.
71 J. E. Kroeze, N. Hirata, L. Schmidt-Mende, C. Orizu, S. D. Ogier, K. Carr, M. Grätzel and J. R. Darrant, *Adv. Funct. Mater.*, 2006, **16**, 1832–1838.
72 K. Aitola, K. Sveinbjornsson, J.-P. Correa-Baena, A. Kaskela, A. Abate, Y. Tian, E. M. J. Johansson, M. Gratzel, E. I. Kauppinen, A. Hagfeldt and G. Boschloo, *Energy Environ. Sci.*, 2016, **9**, 461–466.
73 C.-E. Cheng, C.-Y. Lin, C.-H. Shan, S.-Y. Tsai, K.-W. Lin, C.-S. Chang and F. Shih-Sen Chien, *J. Appl. Phys.*, 2013, **114**, 14503.
74 H. Ellis, N. Vlachopoulos, L. Häggman, C. Perruchot, M. Jouini, G. Boschloo and A. Hagfeldt, *Electrochim. Acta*, 2013, **107**, 45–51.
75 A. A. Arbab, M. H. Peerzada, I. A. Sahito and S. H. Jeong, *J. Power Sources*, 2017, **343**, 412–423.
76 Y. Hou, D. Wang, X. H. Yang, W. Q. Fang, B. Zhang, H. F. Wang, G. Z. Lu, P. Hu, H. J. Zhao and H. G. Yang, *Nat. Commun.*, 2013, **4**, 1583.
77 Y. Rong, Z. Ku, M. Xu, L. Liu, M. Hu, Y. Yang, J. Chen, A. Mei, T. Liu and H. Han, *RSC Adv.*, 2014, **4**, 9271.
78 X. Zhang, Y. Xu, F. Giordano, M. Schreier, N. Pellet, Y. Hu, C. Yi, N. Robertson, J. Hua, S. M. Zakeeruddin, H. Tian and M. Grätzel, *J. Am. Chem. Soc.*, 2016, **138**, 10742–10745.

79 M. Grätzel, *Nature*, 2001, **414**, 338.
80 K. Rajeshwar, Fundamentals of semiconductor electrochemistry and photoelectrochemistry, in *Encyclopedia of Electrochemistry*, ed. A. J. Bard, M. Stratmann and S. Licht, Wiley-VCH Verlag GmbH & Co. KGaA, Weinheim, Germany, 2007, vol. 6, pp. 1–53.
81 R. Jose, V. Thavasi and S. Ramakrishna, *J. Am. Ceram. Soc.*, 2009, **92**, 289–301.
82 M. Wang, C. Grätzel, S. M. Zakeeruddin and M. Grätzel, *Energy Environ. Sci.*, 2012, **5**, 9394–9405.
83 J. Cong, X. Yang, L. Kloo and L. Sun, *Energy Environ. Sci.*, 2012, **5**, 9180–9194.
84 P. Liu, J. M. Gardner and L. Kloo, *Chem. Commun.*, 2015, **51**, 14660–14662.
85 U. Bach, D. Lupo, P. Comte, J. E. Moser, F. Weissörtel, J. Salbeck, H. Spreitzer, M. Grätzel, F. Weissortel, J. Salbeck, H. Spreitzer, M. Gratzel, F. Weissörtel, J. Salbeck, H. Spreitzer, M. Grätzel, F. Weissortel, J. Salbeck, H. Spreitzer, M. Gratzel, F. Weissörtel, J. Salbeck, H. Spreitzer and M. Grätzel, *Nature*, 1998, **395**, 583–585.
86 M. Freitag, F. Giordano, W. Yang, M. Pazoki, Y. Hao, B. Zietz, M. Grätzel, A. Hagfeldt and G. Boschloo, *J. Phys. Chem. C*, 2016, **120**, 9595–9603.
87 Y. Cao, Y. Saygili, A. Ummadisingu, J. J. Teuscher, J. Luo, N. Pellet, F. Giordano, S. M. Zakeeruddin, J.-E.-E. E. J.-E. Moser, M. Freitag, A. Hagfeldt and M. Grätzel, *Nat. Commun.*, 2017, **8**, 15390.
88 F. Fabregat-Santiago, J. Bisquert, L. Cevey, P. Chen, M. Wang, S. M. Zakeeruddin and M. Grätzel, *J. Am. Chem. Soc.*, 2008, **131**, 558–562.
89 J. Bisquert and F. Fabregat-Santiago, *Dye Sol. Cells*, 2010, 604.
90 E. Palomares, J. N. Clifford, S. A. Haque, T. Lutz and J. R. Durrant, *J. Am. Chem. Soc.*, 2003, **125**, 475–482.
91 B. C. O'Regan and J. R. Durrant, *Acc. Chem. Res.*, 2009, **42**, 1799–1808.
92 S. A. Haque, E. Palomares, B. M. Cho, A. N. M. Green, N. Hirata, D. R. Klug and J. R. Durrant, *J. Am. Chem. Soc.*, 2005, **127**, 3456–3462.
93 S. Tatay, S. A. Haque, B. O'Regan, J. R. Durrant, W. J. H. Verhees, J. M. Kroon, A. Vidal-Ferran, P. Gaviña and E. Palomares, *J. Mater. Chem.*, 2007, **17**, 3037–3044.
94 J. E. Kroeze, N. Hirata, S. Koops, M. K. Nazeeruddin, L. Schmidt-Mende, M. Grätzel and J. R. Durrant, *J. Am. Chem. Soc.*, 2006, **128**, 16376–16383.
95 U. Bach and T. Daeneke, *Angew. Chem., Int. Ed.*, 2012, **51**, 10451–10452.
96 U. B. Cappel, T. Daeneke and U. Bach, *Nano Lett.*, 2012, **12**, 4925–4931.
97 J. Krüger, R. Plass, L. Cevey, M. Piccirelli, M. Grätzel and U. Bach, *Appl. Phys. Lett.*, 2001, **79**, 2085–2087.
98 U. B. Cappel, M. H. Karlsson, N. G. Pschirer, F. Eickemeyer, J. Schöneboom, P. Erk, G. Boschloo and A. Hagfeldt, *J. Phys. Chem. C*, 2009, **113**, 14595–14597.
99 U. B. Cappel, A. L. Smeigh, S. Plogmaker, E. M. J. Johansson, H. Rensmo, L. Hammarström, A. Hagfeldt and G. Boschloo, *J. Phys. Chem. C*, 2011, **115**, 4345–4358.
100 A. J. Mozer, D. K. Panda, S. Gambhir, B. Winther-Jensen and G. G. Wallace, *J. Am. Chem. Soc.*, 2010, **132**, 9543–9545.
101 U. Bach, Y. Tachibana, J.-E. Moser, S. A. Haque, J. R. Durrant, M. Grätzel and D. R. Klug, *J. Am. Chem. Soc.*, 1999, **121**, 7445–7446.
102 M. Freitag, J. Teuscher, Y. Saygili, X. Zhang, F. Giordano, P. Liska, J. Hua, S. M. S. M. S. M. S. M. S. M. S. M. Zakeeruddin, J.-E. J.-E. M. J.-E. J.-E. E. Moser, M. Grätzel and A. Hagfeldt, *Nat. Photonics*, 2017, **11**, 372–378.
103 W. Zhang, Y. Wu, H. W. Bahng, Y. Cao, C. Yi, Y. Saygili, J. Luo, Y. Liu, L. Kavan, J. E. Moser, A. Hagfeldt, H. Tian, S. M. Zakeeruddin, W. Zhu and M. Grätzel, *Energy Environ. Sci.*, 2018, **11**, 1779–1787.
104 Y. Cao, Y. Liu, S. M. Zakeeruddin, A. Hagfeldt and M. Grätzel, *Joule*, 2018, **2**, 1108–1117.
105 M. Wolf and H. Rauschenbach, *Adv. Energy Convers.*, 1963, **3**, 455–479.
106 D. Gentilini, D. D'Ercole, A. Gagliardi, A. Brunetti, A. Reale, T. Brown and A. Di Carlo, *Superlattices Microstruct.*, 2010, **47**, 192–196.
107 M. Freitag, Q. Daniel, M. Pazoki, K. Sveinbjörnsson, J. Zhang, L. Sun, A. Hagfeldt and G. Boschloo, *Energy Environ. Sci.*, 2015, **8**, 2634–2637.
108 J. J. Nelson, T. J. Amick and C. M. Elliott, *J. Phys. Chem. C*, 2008, **112**, 18255–18263.
109 T. M. W. J. Bandara, W. J. M. J. S. R. Jayasundara, H. D. N. S. Fernado, M. A. K. L. Dissanayake, L. A. A. De Silva, I. Albinsson, M. Furlani and B. E. Mellander, *J. Appl. Electrochem.*, 2015, **45**, 289–298.
110 J. Bisquert, F. Fabregat-santiago, I. Mora-Seró, G. Garcia-Belmonte and S. Gimenez, *J. Phys. Chem. C*, 2009, **113**, 17278–17290.
111 G. Boschloo and A. Hagfeldt, *Inorg. Chim. Acta*, 2008, **361**, 729–734.
112 T. Daeneke, A. J. Mozer, Y. Uemura, S. Makuta, M. Fekete, Y. Tachibana, N. Koumura, U. Bach and L. Spiccia, *J. Am. Chem. Soc.*, 2012, **134**, 16925–16928.
113 W. Yang, N. Vlachopoulos, Y. Hao, A. Hagfeldt and G. Boschloo, *Phys. Chem. Chem. Phys.*, 2015, **17**, 15868–15875.
114 W. Shockley and H. J. Queisser, *J. Appl. Phys.*, 1961, **32**, 510–519.
115 H. J. Queisser, *Mater. Sci. Eng., B*, 2009, **159–160**, 322–328.
116 P. K. Nayak and D. Cahen, *Adv. Mater.*, 2014, **26**, 1622–1628.
117 L. Yang, B. Xu, D. Bi, H. Tian, G. Boschloo, L. Sun, A. Hagfeldt and E. M. J. Johansson, *J. Am. Chem. Soc.*, 2013, **135**, 7378–7385.
118 P. Liu, W. Sharmoukh, B. Xu, Y. Y. Li, G. Boschloo, L. Sun and L. Kloo, *ACS Omega*, 2017, **2**, 1812–1819.
119 L. Yang, U. B. Cappel, E. L. Unger, M. Karlsson, K. M. Karlsson, E. Gabrielsson, L. Sun, G. Boschloo, A. Hagfeldt and E. M. J. Johansson, *Phys. Chem. Chem. Phys.*, 2012, **14**, 779–789.
120 B. Peng, G. Jungmann, C. Jäger, D. Haarer, H.-W. Schmidt and M. Thelakkat, *Coord. Chem. Rev.*, 2004, **248**, 1479–1489.
121 J. Park and M. Lee, *Electron. Mater. Lett.*, 2015, **11**, 271–275.
122 H. Choi, C. Nahm, J. Kim, J. Moon, S. Nam, D.-R. Jung and B. Park, *Curr. Appl. Phys.*, 2012, **12**, 737–741.

123 U. Diebold, *Surf. Sci. Rep.*, 2003, **48**, 53–229.
124 H. Yan, X. Wang, M. Yao and X. Yao, *Prog. Nat. Sci.: Mater. Int.*, 2013, **23**, 402–407.
125 A. Wypych, I. Bobowska, M. Tracz, A. Opasinska, S. Kadlubowski, A. Krzywania-Kaliszewska, J. Grobelny and P. Wojciechowski, *J. Nanomater.*, 2014, **2014**, 124814.
126 S. Hore, C. Vetter, R. Kern, H. Smit and A. Hinsch, *Sol. Energy Mater. Sol. Cells*, 2006, **90**, 1176–1188.
127 J. Wang and Y. Shang, *Appl. Phys. Lett.*, 2013, **102**, 143113.
128 W. Maiaugree, S. Pimanpang, W. Jarernboon and V. Amornkitbamrung, *Int. J. Photoenergy*, 2016, **2016**, 1–10.
129 E. J. W. Crossland, M. Kamperman, M. Nedelcu, C. Ducati, U. Wiesner, D.-M. Smilgies, G. E. S. Toombes, M. A. Hillmyer, S. Ludwigs, U. Steiner and H. J. Snaith, *Nano Lett.*, 2009, **9**, 2807–2812.
130 P. Docampo, S. Guldin, M. Stefik, P. Tiwana, M. C. Orilall, S. Hüttner, H. Sai, U. Wiesner, U. Steiner and H. J. Snaith, *Adv. Funct. Mater.*, 2010, **20**, 1787–1796.
131 E. J. W. Crossland, N. Noel, V. Sivaram, T. Leijtens, J. A. Alexander-Webber and H. J. Snaith, *Nature*, 2013, **495**, 215–219.
132 B. O'Regan, D. T. Schwartz, S. M. Zakeeruddin and M. Grätzel, *Adv. Mater.*, 2000, **12**, 1263–1267.
133 N. O. V. Plank, H. J. Snaith, C. Ducati, J. S. Bendall, L. Schmidt-Mende and M. E. Welland, *Nanotechnology*, 2008, **19**, 465603.
134 C. Xu, J. Wu, U. V. Desai and D. Gao, *Nano Lett.*, 2012, **12**, 2420–2424.
135 K. Tennakone, V. P. S. Perera, I. R. M. Kottegoda, L. A. A. De Silva, G. R. R. A. Kumara and A. Konno, *J. Electron. Mater.*, 2001, **30**, 992–996.
136 P. Docampo and H. J. Snaith, *Nanotechnology*, 2011, **22**, 225403.
137 B. C. O'Regan, S. Scully, A. C. Mayer, E. Palomares and J. Durrant, *J. Phys. Chem. B*, 2005, **109**, 4616–4623.
138 S. Suresh, G. E. Unni, M. Satyanarayana, A. Sreekumaran Nair and V. P. Mahadevan Pillai, *J. Colloid Interface Sci.*, 2018, **524**, 236–244.
139 L. Li, Q. Lu, W. Li, X. Li, A. Hagfeldt, W. Zhang and M. Wu, *J. Power Sources*, 2016, **308**, 37–43.
140 P. Jayabal, V. Sasirekha, J. Mayandi, K. Jeganathan and V. Ramakrishnan, *J. Alloys Compd.*, 2014, **586**, 456–461.
141 M. Saito and S. Fujihara, *Energy Environ. Sci.*, 2008, **1**, 280–283.
142 J. Bouclé and J. Ackermann, *Polym. Int.*, 2012, **61**, 355–373.
143 B. O'Regan, F. Lenzmann, R. Muis and J. Wienke, *Chem. Mater.*, 2002, **14**, 5023–5029.
144 W.-Y. Rho, D. H. Song, H.-Y. Yang, H.-S. Kim, B. S. Son, J. S. Suh and B.-H. Jun, *J. Solid State Chem.*, 2018, **258**, 271–282.
145 M. D. Brown, T. Suteewong, R. S. S. Kumar, V. D'Innocenzo, A. Petrozza, M. M. Lee, U. Wiesner and H. J. Snaith, *Nano Lett.*, 2011, **11**, 438–445.
146 M. H. Buraidah, L. P. Teo, C. M. Au Yong, S. Shah and A. K. Arof, *Opt. Mater.*, 2016, **57**, 202–211.
147 C. T. Yip, H. Huang, L. Zhou, K. Xie, Y. Wang, T. Feng, J. Li and W. Y. Tam, *Adv. Mater.*, 2011, **23**, 5624–5628.
148 S. Guldin, S. Hüttner, M. Kolle, M. E. Welland, P. Müller-Buschbaum, R. H. Friend, U. Steiner and N. Tétreault, *Nano Lett.*, 2010, **10**, 2303–2309.
149 B. Lee, C. C. Stoumpos, N. Zhou, F. Hao, C. Malliakas, C.-Y. Yeh, T. J. Marks, M. G. Kanatzidis and R. P. H. Chang, *J. Am. Chem. Soc.*, 2014, **136**, 15379–15385.
150 K. Kakiage, Y. Aoyama, T. Yano, T. Otsuka, T. Kyomen, M. Unno and M. Hanaya, *Chem. Commun.*, 2014, **50**, 6379–6381.
151 K. Kakiage, T. Tokutome, S. Iwamoto, T. Kyomen and M. Hanaya, *Chem. Commun.*, 2013, **49**, 179–180.
152 T. T. T. Pham, S. K. Saha, D. Provost, Y. Farré, M. Raissi, Y. Pellegrin, E. Blart, S. Vedraine, B. Ratier, D. Aldakov, F. Odobel and J. Bouclé, *J. Phys. Chem. C*, 2017, **121**, 129–139.
153 X. Jiang, K. M. Karlsson, E. Gabrielsson, E. M. J. Johansson, M. Quintana, M. Karlsson, L. Sun, G. Boschloo and A. Hagfeldt, *Adv. Funct. Mater.*, 2011, **21**, 2944–2952.
154 Y. Hu, A. Abate, Y. Cao, A. Ivaturi, S. M. Zakeeruddin, M. Grätzel and N. Robertson, *J. Phys. Chem. C*, 2016, **120**, 15027–15034.
155 H. Ellis, S. K. Eriksson, S. M. Feldt, E. Gabrielsson, P. W. Lohse, R. Lindblad, L. Sun, H. Rensmo, G. Boschloo and A. Hagfeldt, *J. Phys. Chem. C*, 2013, **117**, 21029–21036.
156 L.-L. Li and E. W.-G. Diau, *Chem. Soc. Rev.*, 2013, **42**, 291–304.
157 J. Krüger, R. Plass, M. Grätzel and H.-J. Matthieu, *Appl. Phys. Lett.*, 2002, **81**, 367.
158 L. Schmidt-Mende, S. M. Zakeeruddin and M. Grätzel, *Appl. Phys. Lett.*, 2005, **86**, 2001–2004.
159 H. J. Snaith, S. M. Zakeeruddin, L. Schmidt-Mende, C. C. Klein, M. Grätzel, M. Grätzel and M. Grätzel, *Angew. Chem., Int. Ed.*, 2005, **44**, 6413–6417.
160 C.-Y. Chen, M. Wang, J.-Y. Li, N. Pootrakulchote, L. Alibabaei, C. Ngoc-le, J.-D. Decoppet, J.-H. Tsai, C. Grätzel, C.-G. Wu, S. M. Zakeeruddin and M. Grätzel, *ACS Nano*, 2009, **3**, 3103–3109.
161 M. Wang, S.-J. J. Moon, D. Zhou, F. Le Formal, N.-L. L. Cevey-Ha, R. Humphry-Baker, C. Grätzel, P. Wang, S. M. Zakeeruddin and M. Grätzel, *Adv. Funct. Mater.*, 2010, **20**, 1821–1826.
162 E. W.-G. Diau, *Meet. Abstr.*, 2015, **MA2015-01**, 1012.
163 P. Qin, P. Sanghyun, M. I. Dar, K. Rakstys, H. ElBatal, S. A. Al-Muhtaseb, C. Ludwig and M. K. Nazeeruddin, *Adv. Funct. Mater.*, 2016, **26**, 5550–5559.
164 J.-W. Shiu, Y.-C. Chang, C.-Y. Chan, H.-P. Wu, H.-Y. Hsu, C.-L. Wang, C.-Y. Lin and E. W.-G. Diau, *J. Mater. Chem. A*, 2015, **3**, 1417–1420.
165 J. Liu, W. Zhou, J. Liu, Y. Fujimori, T. Higashino, H. Imahori, X. Jiang, J. Zhao, T. Sakurai, Y. Hattori, W. Matsuda, S. Seki, S. K. Garlapati, S. Dasgupta, E. Redel, L. Sun and C. Wöll, *J. Mater. Chem. A*, 2016, **4**, 12739–12747.
166 L. Schmidt-Mende, U. Bach, R. Humphry-Baker, T. Horiuchi, H. Miura, S. Ito, S. Uchida and M. Grätzel, *Adv. Mater.*, 2005, **17**, 813–815.
167 S. Benhattab, R. Nakar, J. W. Rodriguez Acosta, N. Berton, J. Faure-Vincent, J. Bouclé, F. Tran Van and B. Schmaltz, *Dyes Pigm.*, 2018, **151**, 238–244.

168 B. Xu, H. Tian, D. Bi, E. Gabrielsson, E. M. J. Johansson, G. Boschloo, A. Hagfeldt and L. Sun, *J. Mater. Chem. A*, 2013, **1**, 14467–14470.
169 I. Bruder, M. Karlsson, F. Eickemeyer, J. Hwang, P. Erk, A. Hagfeldt, J. Weis and N. Pschirer, *Sol. Energy Mater. Sol. Cells*, 2009, **93**, 1896–1899.
170 Z. Yao, M. Zhang, H. Wu, L. Yang, R. Li and P. Wang, *J. Am. Chem. Soc.*, 2015, **137**, 3799–3802.
171 R. Grisorio, L. De Marco, C. Baldisserri, F. Martina, M. Serantoni, G. Gigli and G. P. Suranna, *ACS Sustainable Chem. Eng.*, 2015, **3**, 770–777.
172 H. Ellis, I. Schmidt, A. Hagfeldt, G. Wittstock and G. Boschloo, *J. Phys. Chem. C*, 2015, **119**, 21775–21783.
173 A. Mahmood, *Sol. Energy*, 2016, **123**, 127–144.
174 J. Jia, Y. Chen, L. Duan, Z. Sun, M. Liang and S. Xue, *RSC Adv.*, 2017, **7**, 45807–45817.
175 A. Konno, G. R. A. Kumara, S. Kaneko, B. Onwona-Agyeman and K. Tennakone, *Chem. Lett.*, 2007, **36**, 716–717.
176 S. Kolemen, Y. Cakmak, S. Erten-Ela, Y. Altay, J. Brendel, M. Thelakkat and E. U. Akkaya, *Org. Lett.*, 2010, **12**, 3812–3815.
177 N. Cai, S.-J. Moon, L. L. Cevey-Ha, T. Moehl, R. Humphry-Baker, P. Wang, S. M. Zakeeruddin, M. Grätzel and M. Grätzel, *Nano Lett.*, 2011, **11**, 1452–1456.
178 A. Dualeh, F. De Angelis, S. Fantacci, T. Moehl, C. Yi, F. Kessler, E. Baranoff, M. K. Nazeeruddin and M. Grätzel, *J. Phys. Chem. C*, 2012, **116**, 1572–1578.
179 A. Dualeh, J. H. Delcamp, M. K. Nazeeruddin and M. Grätzel, *Appl. Phys. Lett.*, 2012, **100**, 173512.
180 W. H. Nguyen, C. D. Bailie, J. Burschka, T. Moehl, M. Grätzel, M. D. McGehee and A. Sellinger, *Chem. Mater.*, 2013, **25**, 1519–1525.
181 A. Abate, M. Planells, D. J. Hollman, S. D. Stranks, A. Petrozza, A. R. S. Kandada, Y. Vaynzof, S. K. Pathak, N. Robertson and H. J. Snaith, *Adv. Energy Mater.*, 2014, **4**, 1400166.
182 Z. Shen, B. Xu, P. Liu, Y. Hu, Y. Yu, H. Ding, L. Kloo, J. Hua, L. Sun and H. Tian, *J. Mater. Chem. A*, 2017, **5**, 1242–1247.
183 P. Liu, B. Xu, K. M. Karlsson, J. B. Zhang, N. Vlachopoulos, G. Boschloo, L. C. Sun and L. Kloo, *J. Mater. Chem. A*, 2015, **3**, 4420–4427.
184 M. Suzuka, N. Hayashi, T. Sekiguchi, K. Sumioka, M. Takata, N. Hayo, H. Ikeda, K. Oyaizu and H. Nishide, *Sci. Rep.*, 2016, **6**, 28022.
185 X. Lan, O. Voznyy, F. P. García de Arquer, M. Liu, J. Xu, A. H. Proppe, G. Walters, F. Fan, H. Tan, M. Liu, Z. Yang, S. Hoogland and E. H. Sargent, *Nano Lett.*, 2016, **16**, 4630–4634.
186 M. Liu, O. Voznyy, R. Sabatini, F. P. García de Arquer, R. Munir, A. H. Balawi, X. Lan, F. Fan, G. Walters, A. R. Kirmani, S. Hoogland, F. Laquai, A. Amassian and E. H. Sargent, *Nat. Mater.*, 2017, **16**, 258–263.
187 E. M. Sanehira, A. R. Marshall, J. A. Christians, S. P. Harvey, P. N. Ciesielski, L. M. Wheeler, P. Schulz, L. Y. Lin, M. C. Beard and J. M. Luther, *Sci. Adv.*, 2017, **3**, eaao4204.
188 M. Ye, X. Gao, X. Hong, Q. Liu, C. He, X. Liu and C. Lin, Sustain, *Energy Fuels*, 2017, **1**, 1217–1231.
189 W. Wang, W. Feng, J. Du, W. Xue, L. Zhang, L. Zhao, Y. Li and X. Zhong, *Adv. Mater.*, 2018, **30**, 1705746.
190 A. N. Jumabekov, N. Cordes, T. D. Siegler, P. Docampo, A. Ivanova, K. Fominykh, D. D. Medina, L. M. Peter and T. Bein, *ACS Appl. Mater. Interfaces*, 2016, **8**, 4600–4607.
191 J. P. Park, J. H. Heo, S. H. Im and S.-W. Kim, *J. Mater. Chem. A*, 2016, **4**, 785–790.
192 X. Zhang, J. Liu, J. Zhang, N. Vlachopoulos and E. M. J. Johansson, *Phys. Chem. Chem. Phys.*, 2015, **17**, 12786–12795.
193 J. Duan, Q. Tang, Y. Sun, B. He and H. Chen, *RSC Adv.*, 2014, **4**, 60478–60483.
194 A. G. Kontos, T. Stergiopoulos, V. Likodimos, D. Milliken, H. Desilvesto, G. Tulloch and P. Falaras, *J. Phys. Chem. C*, 2013, **117**, 8636–8646.
195 C. Law, S. C. Pathirana, X. Li, A. Y. Anderson, P. R. F. Barnes, A. Listorti, T. H. Ghaddar and B. C. O′Regan, *Adv. Mater.*, 2010, **22**, 4505–4509.
196 A. F. Nogueira, C. Longo and M.-A. A. De Paoli, *Coord. Chem. Rev.*, 2004, **248**, 1455–1468.
197 H. Klauk, *Organic Electronics II: More Materials and Applications*, Wiley, 2012.
198 J. D. Roy-Mayhew and I. A. Aksay, *Chem. Rev.*, 2014, **114**, 6323–6348.
199 S. Kitagawa, R. Kitaura and S. Noro, *Angew. Chem., Int. Ed.*, 2004, **43**, 2334–2375.
200 J. Zhang, L. Häggman, M. Jouini, A. Jarboui, G. Boschloo, N. Vlachopoulos and A. Hagfeldt, *ChemPhysChem*, 2014, **15**, 1043–1047.
201 P. V. Wright, *Br. Polym. J.*, 1975, **7**, 319–327.
202 C. Berthier, W. Gorecki, M. Minier, M. B. Armand, J. M. Chabagno and P. Rigaud, *Solid State Ionics*, 1983, **11**, 91–95.
203 M. Armand, *Solid State Ionics*, 1983, **9–10**, 745–754.
204 G. C. Farrington and J. L. Briant, *Science*, 1979, **204**, 1371–1379.
205 M. Armand, *Solid State Ionics*, 1994, **69**, 309–319.
206 M. B. Armand, M. J. Duclot and P. Rigaud, *Solid State Ionics*, 1981, **3–4**, 429–430.
207 M. S. Michael, M. M. E. Jacob, S. R. S. Prabaharan and S. Radhakrishna, *Solid State Ionics*, 1997, **98**, 167–174.
208 K. M. Abraham, Z. Jiang and B. Carroll, *Chem. Mater.*, 1997, **9**, 1978–1988.
209 A. F. Nogueira, N. Alonso-Vante and M.-A. De Paoli, *Synth. Met.*, 1999, **105**, 23–27.
210 J. Nei de Freitas, A. F. Nogueira and M.-A. De Paoli, *J. Mater. Chem.*, 2009, **19**, 5279–5294.
211 T. Stergiopoulos, I. M. Arabatzis, G. Katsaros and P. Falaras, *Nano Lett.*, 2002, **2**, 1259–1261.
212 J. Wu, S. Hao, Z. Lan, J. Lin, M. Huang, Y. Huang, P. Li, S. Yin and T. Sato, *J. Am. Chem. Soc.*, 2008, **130**, 11568–11569.
213 J. Li, H. Wang, G. Zhou and Z.-S. Wang, *Chem. Commun.*, 2013, **49**, 9446–9448.
214 F. Bella, N. N. Mobarak, F. N. Jumaah and A. Ahmad, *Electrochim. Acta*, 2015, **151**, 306–311.

215 A. F. Nogueira, M. A. S. Spinacé, W. A. Gazotti, E. M. Girotto and M.-A. de Paoli, *Solid State Ionics*, 2001, **140**, 327–335.
216 G. Katsaros, T. Stergiopoulos, I. M. Arabatzis, K. G. Papadokostaki and P. Falaras, *J. Photochem. Photobiol., A*, 2002, **149**, 191–198.
217 E. Chatzivasiloglou, T. Stergiopoulos, N. Spyrellis and P. Falaras, *J. Mater. Process. Technol.*, 2005, **161**, 234–240.
218 J. H. Seo, A. Gutacker, Y. Sun, H. Wu, F. Huang, Y. Cao, U. Scherf, A. J. Heeger and G. C. Bazan, *J. Am. Chem. Soc.*, 2011, **133**, 8416–8419.
219 P. Wang, S. M. Zakeeruddin, P. Comte, I. Exnar and M. Grätzel, *J. Am. Chem. Soc.*, 2003, **125**, 1166–1167.
220 L. Fan, S. Kang, J. Wu, S. Hao, Z. Lan and J. Lin, *Energy Sources, Part A*, 2010, **32**, 1559–1568.
221 P. Wang, S. M. Zakeeruddin, J. E. Moser, M. K. Nazeeruddin, T. Sekiguchi and M. Grätzel, *Nat. Mater.*, 2003, **2**, 402–407.
222 F. Bella, N. Vlachopoulos, K. Nonomura, S. M. Zakeeruddin, M. Gratzel, C. Gerbaldi, A. Hagfeldt, M. Grätzel, C. Gerbaldi, A. Hagfeldt, M. Gratzel, C. Gerbaldi, A. Hagfeldt, M. Grätzel, C. Gerbaldi, A. Hagfeldt, M. Gratzel, C. Gerbaldi and A. Hagfeldt, *Chem. Commun.*, 2015, **51**, 16308–16311.
223 J. N. de Freitas, A. de, S. Gonçalves, M.-A. De Paoli, J. R. Durrant and A. F. Nogueira, *Electrochim. Acta*, 2008, **53**, 7166–7172.
224 W. Kubo, K. Murakoshi, T. Kitamura, S. Yoshida, M. Haruki, K. Hanabusa, H. Shirai, Y. Wada and S. Yanagida, *J. Phys. Chem. B*, 2001, **105**, 12809–12815.
225 F. Bella, J. R. Nair and C. Gerbaldi, *RSC Adv.*, 2013, **3**, 15993–16001.
226 F. Bella and R. Bongiovanni, *J. Photochem. Photobiol., C*, 2013, **16**, 1–21.
227 F. Bella, D. Pugliese, J. R. Nair, A. Sacco, S. Bianco, C. Gerbaldi, C. Barolo and R. Bongiovanni, *Phys. Chem. Chem. Phys.*, 2013, **15**, 3706–3711.
228 J. R. Nair, C. Gerbaldi, G. Meligrana, R. Bongiovanni, S. Bodoardo, N. Penazzi, P. Reale and V. Gentili, *J. Power Sources*, 2008, **178**, 751–757.
229 F. Bella, E. D. Ozzello, A. Sacco, S. Bianco and R. Bongiovanni, *Int. J. Hydrogen Energy*, 2014, **39**, 3036–3045.
230 F. Bella, A. Sacco, D. Pugliese, M. Laurenti and S. Bianco, *J. Power Sources*, 2014, **264**, 333–343.
231 F. Bella, R. Bongiovanni, R. S. Kumar, M. A. Kulandainathan and A. M. Stephan, *J. Mater. Chem. A*, 2013, **1**, 9033–9036.
232 A. Chiappone, F. Bella, J. R. Nair, G. Meligrana, R. Bongiovanni and C. Gerbaldi, *ChemElectroChem*, 2014, **1**, 1350–1358.
233 C.-H. Tsai, C.-Y. Lu, M.-C. Chen, T.-W. Huang, C.-C. Wu and Y.-W. Chung, *Org. Electron.*, 2013, **14**, 3131–3137.
234 H.-S. Lee, C.-H. Han, Y.-M. Sung, S. S. Sekhon and K.-J. Kim, *Curr. Appl. Phys.*, 2011, **11**, S158–S162.
235 K. S. Lee, Y. Jun and J. H. Park, *Nano Lett.*, 2012, **12**, 2233–2237.
236 F. Bella, A. Lamberti, A. Sacco, S. Bianco, A. Chiodoni and R. Bongiovanni, *J. Membr. Sci.*, 2014, **470**, 125–131.
237 G. P. Salvador, D. Pugliese, F. Bella, A. Chiappone, A. Sacco, S. Bianco and M. Quaglio, *Electrochim. Acta*, 2014, **146**, 44–51.
238 Y. Li, H. Li, C. Zhong, G. Sini and J.-L. Brédas, *npj Flex. Electron.*, 2017, **1**, 2.
239 I. Yavuz and K. N. Houk, *J. Phys. Chem. C*, 2017, **121**, 993–999.
240 J. Melas-Kyriazi, I.-K. Ding, A. Marchioro, A. Punzi, B. E. Hardin, G. F. Burkhard, N. Tétreault, M. Grätzel, J.-E. Moser and M. D. McGehee, *Adv. Energy Mater.*, 2011, **1**, 407–414.
241 Y. Zhang, K. Cao, X. Zhu, X. Li, X. Qiao, G. Tu, B. Zhang, D. Huang, Y. Shen and M. Wang, *RSC Adv.*, 2013, **3**, 14037–14043.
242 M. Rawolle, K. Sarkar, M. A. Niedermeier, M. Schindler, P. Lellig, J. S. Gutmann, J.-F. Moulin, M. Haese-Seiller, A. S. Wochnik, C. Scheu and P. Müller-Buschbaum, *ACS Appl. Mater. Interfaces*, 2013, **5**, 719–729.
243 M. Juozapavicius, B. C. O'Regan, A. Y. Anderson, J. V. Grazulevicius and V. Mimaite, *Org. Electron.*, 2012, **13**, 23–30.
244 J. Burschka, A. Dualeh, F. Kessler, E. Baranoff, N.-L. L. Cevey-Ha, C. Yi, M. K. Nazeeruddin and M. Grätzel, *J. Am. Chem. Soc.*, 2011, **133**, 18042–18045.
245 W. H. Nguyen, C. D. Bailie, E. L. Unger and M. D. Mcgehee, *J. Am. Chem. Soc.*, 2014, **136**, 10996–11001.
246 T. Malinauskas, D. Tomkute-Luksiene, R. Sens, M. Daskeviciene, R. Send, H. Wonneberger, V. Jankauskas, I. Bruder and V. Getautis, *ACS Appl. Mater. Interfaces*, 2015, **7**, 11107–11116.
247 Y. Hua, J. Zhang, B. Xu, P. Liu, M. Cheng, L. Kloo, E. M. J. Johansson, K. Sveinbjörnsson, K. Aitola, G. Boschloo and L. Sun, *Nano Energy*, 2016, **26**, 108–113.
248 D.-G. Ha, J.-J. Kim and M. A. Baldo, *AIP Adv.*, 2016, **6**, 045221.
249 H. Uratani, S. Kubo, K. Shizu, F. Suzuki, T. Fukushima and H. Kaji, *Sci. Rep.*, 2016, **6**, 39128.
250 B. C. Thompson and J. M. J. Fréchet, *Angew. Chem., Int. Ed.*, 2008, **47**, 58–77.
251 P. Agarwala and D. Kabra, *J. Mater. Chem. A*, 2017, **5**, 1348–1373.
252 G. Sathiyan, E. K. T. Sivakumar, R. Ganesamoorthy, R. Thangamuthu and P. Sakthivel, *Tetrahedron Lett.*, 2016, **57**, 243–252.
253 M. Degbia, B. Schmaltz, J. Bouclé, J. V. Grazulevicius, F. Tran-Van and F. Tran-Van, *Polym. Int.*, 2014, **63**, 1387–1393.
254 B. Xu, E. Sheibani, P. Liu, J. Zhang, H. Tian, N. Vlachopoulos, G. Boschloo, L. Kloo, A. Hagfeldt and L. Sun, *Adv. Mater.*, 2014, **26**, 6629–6634.
255 M. Degbia, M. Ben Manaa, B. Schmaltz, N. Berton, J. Bouclé, R. Antony and F. Tran Van, *Mater. Sci. Semicond. Process.*, 2016, **43**, 90–95.
256 T.-T. Bui, S. K. Shah, M. Abbas, X. Sallenave, G. Sini, L. Hirsch and F. Goubard, *ChemNanoMat*, 2015, **1**, 203–210.
257 A. Tomkeviciene, G. Puckyte, J. V. Grazulevicius, M. Degbia, F. Tran-Van, B. Schmaltz, V. Jankauskas and J. Bouclé, *Synth. Met.*, 2012, **162**, 1997–2004.
258 R. Lygaitis, B. Schmaltz, R. Degutyte, J. V. Gražulevičius, M. Degbia, F. T. Van, P. Strohriegl, V. Jankauskas and J. Bouclé, *Synth. Met.*, 2014, **195**, 328–334.
259 M. Planells, A. Abate, D. J. Hollman, S. D. Stranks, V. Bharti, J. Gaur, D. Mohanty, S. Chand, H. J. Snaith and N. Robertson, *J. Mater. Chem. A*, 2013, **1**, 6949–6960.

260 P. Liu, B. Xu, Y. Hua, M. Cheng, K. Aitola, K. Sveinbjörnsson, J. Zhang, G. Boschloo, L. Sun and L. Kloo, *J. Power Sources*, 2017, **344**, 11–14.
261 W. Yuan, H. Zhao and G. L. Baker, *Org. Electron.*, 2014, **15**, 3362–3369.
262 R. K. Aulakh, S. Sandhu, Tanvi, S. S. Kumar, A. Mahajan, R. K. Bedi and S. S. Kumar, *Synth. Met.*, 2015, **205**, 92–97.
263 T.-T. Bui, S. K. Shah, X. Sallenave, M. Abbas, G. Sini, L. Hirsch and F. Goubard, *RSC Adv.*, 2015, **5**, 49590–49597.
264 B. Xu, D. Bi, Y. Hua, P. Liu, M. Cheng, M. Grätzel, L. Kloo, A. Hagfeldt, L. Sun, M. Gratzel, L. Kloo, A. Hagfeldt, L. Sun, M. Grätzel, L. Kloo, A. Hagfeldt, L. Sun, M. Gratzel, L. Kloo, A. Hagfeldt, L. Sun, M. Grätzel, L. Kloo, A. Hagfeldt and L. Sun, *Energy Environ. Sci.*, 2016, **9**, 873–877.
265 B. Kim, J. K. Koh, J. H. J. J. H. J. Kim, W. S. Chi, J. H. J. J. H. J. Kim and E. Kim, *ChemSusChem*, 2012, **5**, 2173–2180.
266 J. Zhang, L. Yang, Y. Shen, B.-W. W. Park, Y. Hao, E. M. J. Johansson, G. Boschloo, L. Kloo, E. Gabrielsson, L. Sun, A. Jarboui, C. Perruchot, M. Jouini, N. Vlachopoulos and A. Hagfeldt, *J. Phys. Chem. C*, 2014, **118**, 16591–16601.
267 J. Zhang, N. Vlachopoulos, Y. Hao, T. W. Holcombe, G. Boschloo, E. M. J. J. Johansson, M. Grätzel and A. Hagfeldt, *ChemPhysChem*, 2016, **17**, 1441–1445.
268 W.-C. Chen, Y.-H. Lee, C.-Y. Chen, K.-C. Kau, L.-Y. Lin, C.-A. Dai, C.-G. Wu, K.-C. Ho, J.-K. Wang and L. Wang, *ACS Nano*, 2014, **8**, 1254–1262.
269 N. Zhou, B. Lee, A. Timalsina, P. Guo, X. Yu, T. J. Marks, A. Facchetti and R. P. H. Chang, *J. Phys. Chem. C*, 2014, **118**, 16967–16975.
270 Q. Liu, C. Li, K. Jiang, Y. Song and J. Pei, *Particuology*, 2014, **15**, 71–76.
271 M. Chevrier, H. Hawashin, S. Richeter, A. Mehdi, M. Surin, R. Lazzaroni, P. Dubois, B. Ratier, J. Bouclé and S. Clément, *Synth. Met.*, 2017, **226**, 157–163.
272 P. Liu, L. Kloo and J. M. Gardner, *ChemPhotoChem*, 2017, **1**, 363–368.
273 L. Peedikakkandy and P. Bhargava, *Mater. Sci. Semicond. Process.*, 2015, **33**, 103–109.
274 H. Sakamoto, S. Igarashi, M. Uchida, K. Niume and M. Nagai, *Org. Electron.*, 2012, **13**, 514–518.
275 M. Nur Amalina and M. Mohammad Rusop, *Adv. Mater. Res.*, 2013, **667**, 317–323.
276 E. V. A. Premalal, N. Dematage, G. R. R. A. Kumara, R. M. G. Rajapakse, M. Shimomura, K. Murakami and A. Konno, *J. Power Sources*, 2012, **203**, 288–296.
277 K. Hasan, A. K. Bansal, I. D. W. Samuel, C. Roldán-Carmona, H. J. Bolink and E. Zysman-Colman, *Sci. Rep.*, 2015, **5**, 12325.
278 M. Wałęsa-Chorab, R. Banasz, D. Marcinkowski, M. Kubicki and V. Patroniak, *RSC Adv.*, 2017, **7**, 50858–50867.
279 Z. Wei, J. Fan, C. Dai, Z. Pang and S. Han, *ACS Omega*, 2018, **3**, 6874–6879.
280 A. Yella, H.-W. H.-W. H.-W. Lee, H. N. Tsao, C. Yi, A. K. Chandiran, M. K. K. Nazeeruddin, E. W.-G. W.-G. W.-G. Diau, C.-Y. C.-Y. C.-Y. C.-Y. Yeh, S. M. Zakeeruddin, M. Grätzel, M. Gratzel and M. Grätzel, *Science*, 2011, **334**, 629–634.
281 M. K. Kashif, R. A. Milhuisen, M. Nippe, J. Hellerstedt, D. Z. Zee, N. W. Duffy, B. Halstead, F. De Angelis, S. Fantacci, M. S. Fuhrer, C. J. Chang, Y.-B. Cheng, J. R. Long, L. Spiccia and U. Bach, *Adv. Energy Mater.*, 2016, **6**, 1600874.
282 M. K. Kashif, M. Nippe, N. W. Duffy, C. M. Forsyth, C. J. Chang, J. R. Long, L. Spiccia and U. Bach, *Angew. Chem., Int. Ed.*, 2013, **52**, 5527–5531.
283 J.-Y. Kim, J. Y. Kim, D.-K. Lee, B. Kim, H. Kim and M. J. Ko, *J. Phys. Chem. C*, 2012, **116**, 22759–22766.
284 L. Yang, R. Lindblad, E. Gabrielsson, G. Boschloo, H. Rensmo, L. Sun, A. Hagfeldt, T. Edvinsson and E. M. J. Johansson, *ACS Appl. Mater. Interfaces*, 2018, **10**, 11572–11579.
285 M. K. Nazeeruddin, A. Kay, I. Rodicio, R. Humphry-Baker, E. Mueller, P. Liska, N. Vlachopoulos and M. Graetzel, *J. Am. Chem. Soc.*, 1993, **115**, 6382–6390.
286 S. A. Haque, Y. Tachibana, R. L. Willis, J. E. Moser, M. Grätzel, D. R. Klug and J. R. Durrant, *J. Phys. Chem. B*, 2000, **104**, 538–547.
287 J. Krüger, R. Plass, M. Grätzel, P. J. Cameron and L. M. Peter, *J. Phys. Chem. B*, 2003, **107**, 7536–7539.
288 Q. Yu, Y. Wang, Z. Yi, N. Zu, J. Zhang, M. Zhang and P. Wang, *ACS Nano*, 2010, **4**, 6032–6038.
289 E. J. Juarez-Perez, M. R. Leyden, S. Wang, L. K. Ono, Z. Hawash and Y. Qi, *Chem. Mater.*, 2016, **28**, 5702–5709.
290 I. Salzmann, G. Heimel, M. Oehzelt, S. Winkler and N. Koch, *Acc. Chem. Res.*, 2016, **49**, 370–378.
291 J. Luo, J. Xia, H. Yang, L. Chen, Z. Wan, F. Han, H. A. Malik, X. Zhu and C. Jia, *Energy Environ. Sci.*, 2018, **11**, 2035–2045.
292 Y. Hou, X. Du, S. Scheiner, D. P. McMeekin, Z. Wang, N. Li, M. S. Killian, H. Chen, M. Richter, I. Levchuk, N. Schrenker, E. Spiecker, T. Stubhan, N. A. Luechinger, A. Hirsch, P. Schmuki, H.-P. Steinrück, R. H. Fink, M. Halik, H. J. Snaith and C. J. Brabec, *Science*, 2017, **358**, 1192–1197.
293 J. Burschka, F. Kessler, M. K. Nazeeruddin and M. Grätzel, *Chem. Mater.*, 2013, **25**, 2986–2990.
294 D.-Y. Chen, W.-H. Tseng, S.-P. Liang, C.-I. Wu, C.-W. Hsu, Y. Chi, W.-Y. Hung and P.-T. Chou, *Phys. Chem. Chem. Phys.*, 2012, **14**, 11689–11694.
295 M. Xu, Y. Rong, Z. Ku, A. Mei, X. Li and H. Han, *J. Phys. Chem. C*, 2013, **117**, 22492–22496.
296 B. Xu, E. Gabrielsson, M. Safdari, M. Cheng, Y. Hua, H. Tian, J. M. Gardner, L. Kloo and L. Sun, *Adv. Energy Mater.*, 2015, **5**, 1402340.
297 X. Yang, W. Wang, Y. Zhang and L. Sun, *Sol. Energy*, 2018, **170**, 1001–1008.
298 W. Wang, X. Yang, J. Li, H. Wang, J. An, L. Zhang, X. Jiang, Z. Yu and L. Sun, *Energy Technol.*, 2018, **6**, 752–758.
299 C. M. Cardona, W. Li, A. E. Kaifer, D. Stockdale and G. C. Bazan, *Adv. Mater.*, 2011, **23**, 2367–2371.
300 Z. Tang, J. Wu, M. Zheng, J. Huo and Z. Lan, *Nano Energy*, 2013, **2**, 622–627.

301 K. Mohan, A. Bora, B. C. Nath, P. Gogoi, B. J. Saikia and S. K. Dolui, *Electrochim. Acta*, 2016, **222**, 1072–1078.
302 D. Qin, Y. Zhang, S. Huang, Y. Luo, D. Li and Q. Meng, *Electrochim. Acta*, 2011, **56**, 8680–8687.
303 M. Wang, S.-J. Moon, M. Xu, K. Chittibabu, P. Wang, N.-L. Cevey-Ha, R. Humphry-Baker, S. M. Zakeeruddin and M. Grätzel, *Small*, 2010, **6**, 319–324.
304 J. Zhang, M. Freitag, A. Hagfeldt and G. Boschloo, *Molecular Devices for Solar Energy Conversion and Storage*, 2018, pp. 151–185.
305 Y. F. Chiang, C. H. Tsai, P. Chen and T. F. Guo, *Sol. Energy*, 2012, **86**, 1967–1972.
306 Y.-F. F. Chiang, R.-T. T. Chen, A. Burke, U. Bach, P. Chen and T.-F. F. Guo, *Renewable Energy*, 2013, **59**, 136–140.
307 K. Aitola, J. Zhang, N. Vlachopoulos, J. Halme, A. Kaskela, A. G. Nasibulin, E. I. Kauppinen, G. Boschloo and A. Hagfeldt, *J. Solid State Electrochem.*, 2015, **19**, 3139–3144.
308 J. Zhang, J. Feng, Y. Hong, Z. Hu, K. Xia, P. Wang and Y. Zhu, *J. Renewable Sustainable Energy*, 2014, **6**, 043116.
309 G. Y. Margulis, M. G. Christoforo, D. Lam, Z. M. Beiley, A. R. Bowring, C. D. Bailie, A. Salleo and M. D. McGehee, *Adv. Energy Mater.*, 2013, **3**, 1657–1663.
310 G. R. A. Kumara, A. Konno, K. Shiratsuchi, J. Tsukahara and K. Tennakone, *Chem. Mater.*, 2002, **14**, 954–955.
311 I. Celik, A. B. Philips, Z. Song, Y. Yan, R. J. Ellingson, M. J. Heben and D. Apul, *IEEE J. Photovoltaics*, 2018, **8**, 305–309.
312 M. Jørgensen, K. Norrman, S. A. Gevorgyan, T. Tromholt, B. Andreasen and F. C. Krebs, *Adv. Mater.*, 2012, **24**, 580–612.
313 G. Niu, X. Guo and L. Wang, *J. Mater. Chem. A*, 2015, **3**, 8970–8980.
314 Cincinnati Sub-Zero Industrial, *Photovoltaic Module Solar Panel Environmental Testing Guide*, 2016.
315 Fraunhofer Institute for Solar Energy Systems, *PV Module certification for new standards and new technologies*, 2016.
316 S. Jain and V. Agarwal, *IEEE Power Electron. Lett.*, 2004, **2**, 16–19.
317 W. Yang, Y. Hao, P. Ghamgosar and G. Boschloo, *Electrochim. Acta*, 2016, **213**, 879–886.
318 R. Jiang and G. Boschloo, *Inorganics*, 2018, **6**, 60.
319 M. Flasque, A. N. Van Nhien, J. Swiatowska, A. Seyeux, C. Davoisne and F. Sauvage, *ChemPhysChem*, 2014, **15**, 1126–1137.
320 D. Bari, N. Wrachien, G. Meneghesso and C. Andrea, *Reliab. Phys. Symp. (IRPS), 2013 IEEE Int.*, 2013, pp. 4B.3.1–4B.3.7.
321 J. M. Kroon, N. J. Bakker, H. J. P. Smit, P. Liska, K. R. Thampi, P. Wang, S. M. Zakeeruddin, M. Grätzel, A. Hinsch, S. Hore, U. Würfel, R. Sastrawan, J. R. Durrant, E. Palomares, H. Pettersson, T. Gruszecki, J. Walter, K. Skupien and G. E. Tulloch, *Prog. Photovoltaics Res. Appl.*, 2007, **15**, 1–18.
322 S. Yu, S. Ahmadi, C. Sun, P. T. Z. Adibi, W. Chow, A. Pietzsch and M. Göthelid, *J. Chem. Phys.*, 2012, **136**, 154703.
323 K. Schwanitz, U. Weiler, R. Hunger, T. Mayer and W. Jaegermann, *J. Phys. Chem. C*, 2007, **111**, 849–854.
324 A. K. Jena, Y. Numata, M. Ikegami and T. Miyasaka, *J. Mater. Chem. A*, 2018, **6**, 2219–2230.
325 P. Docampo, S. Guldin, T. Leijtens, N. K. Noel, U. Steiner and H. J. Snaith, *Adv. Mater.*, 2014, **26**, 4013–4030.
326 X.-T. Zhang, T. Taguchi, H.-B. Wang, Q.-B. Meng, O. Sato and A. Fujishima, *Res. Chem. Intermed.*, 2007, **33**, 5–11.
327 T. He, Y. F. Wang and J. H. Zeng, *J. Mater. Chem. C*, 2016, **4**, 8235–8244.
328 S.-H. Park, J. Lim, I. Y. Song, J.-R. Lee and T. Park, *Adv. Energy Mater.*, 2014, **4**, 1300489.
329 C. P. Lee, P. Y. Chen, R. Vittal and K. C. Ho, *J. Mater. Chem.*, 2010, **20**, 2356–2361.
330 L. Tao, Z. Huo, Y. Ding, Y. Li, S. Dai, L. Wang, J. Zhu, X. Pan, B. Zhang, J. Yao, M. K. Nazeeruddin and M. Grätzel, *J. Mater. Chem. A*, 2015, **3**, 2344–2352.
331 T. J. Jacobsson, V. Fjällström, M. Edoff and T. Edvinsson, *Sol. Energy Mater. Sol. Cells*, 2015, **138**, 86–95.
332 F. H. Alharbi and S. Kais, *Renewable Sustainable Energy Rev.*, 2015, **43**, 1073–1089.
333 G. Xie, J. Lin, J. Wu, Z. Lan, Q. Li, Y. Xiao, G. Yue, H. Yue and M. Huang, *Chin. Sci. Bull.*, 2011, **56**, 96–101.
334 L. Liang, Y. Yulin, Z. Mi, F. Ruiqing, Q. LeLe, W. Xin, Z. Lingyun, Z. Xuesong and H. Jianglong, *J. Solid State Chem.*, 2013, **198**, 459–465.
335 J. S. Lissau, J. M. Gardner and A. Morandeira, *J. Phys. Chem. C*, 2011, **115**, 23226–23232.
336 C. P. Ponce, R. P. Steer and M. F. Paige, *Photochem. Photobiol. Sci.*, 2013, **12**, 1079–1085.
337 P. Tiwana, P. Docampo, M. B. Johnston, H. J. Snaith and L. M. Herz, *ACS Nano*, 2011, **5**, 5158–5166.
338 A. K. Chandiran, M. Abdi-Jalebi, M. K. Nazeeruddin and M. Grätzel, *ACS Nano*, 2014, **8**, 2261–2268.
339 A. Kay and M. Grätzel, *Chem. Mater.*, 2002, **14**, 2930–2935.
340 B. Onwona-Agyeman, S. Kaneko, A. Kumara, M. Okuya, K. Murakami, A. Konno and K. Tennakone, *Jpn. J. Appl. Phys., Part 2*, 2005, **44**, L731–L733.
341 J. He, H. Lindström, A. Hagfeldt and S.-E. Lindquist, *J. Phys. Chem. B*, 1999, **103**, 8940–8943.
342 L. D'Amario, G. Boschloo, A. Hagfeldt and L. Hammarström, *J. Phys. Chem. C*, 2014, **118**, 19556–19564.
343 L. D'Amario, L. J. Antila, B. Pettersson Rimgard, G. Boschloo and L. Hammarström, *J. Phys. Chem. Lett.*, 2015, **6**, 779–783.
344 L. Zhang, G. Boschloo, L. Hammarström and H. Tian, *Phys. Chem. Chem. Phys.*, 2016, **18**, 5080–5085.
345 L. Tian, J. Föhlinger, P. B. Pati, Z. Zhang, J. Lin, W. Yang, M. Johansson, T. Kubart, J. Sun, G. Boschloo, L. Hammarström and H. Tian, *Phys. Chem. Chem. Phys.*, 2018, **20**, 36–40.
346 L. Tian, J. Föhlinger, Z. Zhang, P. B. Pati, J. Lin, T. Kubart, Y. Hua, J. Sun, L. Kloo, G. Boschloo, L. Hammarström and H. Tian, *Chem. Commun.*, 2018, **54**, 3739–3742.
347 T. J. Jacobsson, J. P. Correa-Baena, M. Pazoki, M. Saliba, K. Schenk, M. Grätzel and A. Hagfeldt, *Energy Environ. Sci.*, 2016, **9**, 1706–1724.
348 J. He, H. Lindström, A. Hagfeldt and S.-E. Lindquist, *Sol. Energy Mater. Sol. Cells*, 2000, **62**, 265–273.

349 M. Dürr, A. Bamedi, A. Yasuda and G. Nelles, *Appl. Phys. Lett.*, 2004, **84**, 3397–3399.
350 W. Kubo, A. Sakamoto, T. Kitamura, Y. Wada and S. Yanagida, *J. Photochem. Photobiol., A*, 2004, **164**, 33–39.
351 E. A. Gibson, A. L. Smeigh, L. Le Pleux, J. Fortage, G. Boschloo, E. Blart, Y. Pellegrin, F. Odobel, A. Hagfeldt and L. Hammarström, *Angew. Chem., Int. Ed.*, 2009, **48**, 4402–4405.
352 G. Boschloo and A. Hagfeldt, *Acc. Chem. Res.*, 2009, **42**, 1819–1826.
353 N. Papageorgiou, M. Grätzel and P. P. Infelta, *Sol. Energy Mater. Sol. Cells*, 1996, **44**, 405–438.
354 S. M. Feldt, E. A. Gibson, E. Gabrielsson, L. Sun, G. Boschloo and A. Hagfeldt, *J. Am. Chem. Soc.*, 2010, **132**, 16714–16724.
355 Y. Saygili, M. Söderberg, N. Pellet, F. Giordano, Y. Cao, A. B. A. B. A. B. A. B. Munoz-García, S. M. S. M. S. M. S. M. S. M. Zakeeruddin, N. Vlachopoulos, M. Pavone, G. Boschloo, L. Kavan, J.-E. J.-E. E. Moser, M. Grätzel, A. Hagfeldt, M. Freitag, A. B. Munoz-Garcia, S. M. S. M. S. M. S. M. S. M. Zakeeruddin, N. Vlachopoulos, M. Pavone, G. Boschloo, L. Kavan, J.-E. J.-E. E. Moser, M. Grätzel, A. Hagfeldt and M. Freitag, *J. Am. Chem. Soc.*, 2016, **138**, 15087–15096.
356 T. Förster, *Naturwissenschaften*, 1946, **33**, 166–175.
357 G. K. Mor, J. Basham, M. Paulose, S. Kim, O. K. Varghese, A. Vaish, S. Yoriya and C. A. Grimes, *Nano Lett.*, 2010, **10**, 2387–2394.
358 E. L. Unger, A. Morandeira, M. Persson, B. Zietz, E. Ripaud, P. Leriche, J. Roncali, A. Hagfeldt and G. Boschloo, *Phys. Chem. Chem. Phys.*, 2011, **13**, 20172.
359 S. J. Moon, E. Baranoff, S. M. Zakeeruddin, C. Y. Yeh, E. W. G. Diau, M. Grätzel and K. Sivula, *Chem. Commun.*, 2011, **47**, 8244–8246.